Three-Dimensional Thermal Structure of Subduction Zones

by

Juan Carlos Rosas Bonilla

A thesis submitted in partial fulfillment of the
requirements for the degree of

Doctor of Philosophy

in

Geophysics

Department of Physics
University of Alberta

© Juan Carlos Rosas Bonilla, 2016

Abstract

The temperature distribution controls many processes occurring at subduction zones, such as slab dehydration and metamorphism, mantle wedge melting and the formation of arc volcanoes, and the rupture width of megathrust earthquakes. The thermal structure of the subducting oceanic plate (slab) is primarily controlled by conduction and advection of heat due to its downward motion. In the mantle wedge, heat is transported by the solid-state flow of the mantle driven by the coupling with the slab. The resulting flow pattern depends on the geometry of the subduction zone and in the rheology employed for the mantle.

A common approach for the study of the thermal structure of subduction zones consists in creating two-dimensional (2D) models in which a specific geometry and velocity is assigned to the slab and upper plate. The mantle wedge flows dynamically in a 2D corner flow driven by viscous coupling with the slab. Whereas this approach has been very successful and applied to a wide range of real subduction zones, the last decade has seen a surge of three-dimensional (3D) subduction models. 3D effects are important in subduction zones in which the along-strike geometry exhibits significant changes (i.e changes in the dip, trench curvature, or proximity to slab edges). As the driving force for mantle wedge flow is the pressure gradient induced by the viscous drag of the slab, the presence of along-strike changes in the structure of a subduction zone adds a trench-parallel component that can induce along-strike mantle wedge flow. This 3D flow geometry results in a thermal structure that differs from that obtained by traditional 2D models.

In this thesis, I present 3D thermal models of several sections of the subduction zone along the Middle America Trench (MAT). The models employ a kinematic slab and a dynamic mantle wedge that flows in response to the drag imposed by the down-

going plate. Along-strike changes in the age of the plate are incorporated through a 2D oceanic boundary condition. As the thermal state of the slab is also affected by hydrothermal circulation in the uppermost oceanic crust, the effects of along-strike changes in the efficiency of hydrothermal circulation are studied through 2D and 3D models. For the mantle wedge flow, model results show that the mantle flows along-strike from steep-dip regions to shallow-dip regions in the presence of changes in the angle of subduction. The magnitude and geometry of the flow depends on the rheology employed, with non-Newtonian, dislocation creep viscosities giving faster flow velocities and higher temperatures for the wedge with respect to an isoviscous rheology. For the MAT, the thermal change in the wedge due to along-strike flow is larger than 70°, which may be important for magma-generation depending on the amount of water the mantle holds. The direction and orientation of the flow can also be compared to seismic anisotropy studies. Theoretical studies show that the flow direction and the a-axis of olivine minerals are aligned. Along the MAT, several studies have shown an anisotropy pattern in which the a-axis have a trench-parallel component. In central Mexico, this orientation has been proposed to be due to a slab tear that cuts the Cocos plate into two sections, which allows asthenospheric mantle to flow into the mantle wedge and disrupt the corner flow. For this thesis, instead of incorporating this tear, a continuous slab geometry is employed in the models of Mexico. The mantle wedge flow obtained form these models is shown to be mostly aligned with the anisotropy pattern, which suggests the Cocos plate is probably not fragmented in central Mexico. This result is also in agreement with geochemical studies of the volcanic arc of Mexico, in which no particular signal that would suggest a broken slab is found. For the case of Central America, seismic anisotropy observations also reveal an along-strike flow component. Modeling results for this area shows that the along-strike flow caused by slab dip variations has a southeastward direction, which

is opposite to the northwestward direction inferred by arc geochemical studies. This suggests the along-strike flow in this region is induced by a different mechanism, most likely a combination of slab rollback and proximity to a slab edge near Panama.

Preface

The work presented in this thesis is an original work developed by myself, Juan Carlos Rosas Bonilla. Chapter 4 has been submitted to *Physics of the Earth and Planetary Interiors* (PEPI), peer-reviewed, and the revised version is included in this thesis. Chaper 5 has already been published in *Pure and Applied Geophysics*, and Chapter 6 will be submitted to *Earth and Planetary Science Letters* (EPSL). The design, implementation and interpretation of all the models presented in this thesis was my responsibility, as well as of most of the manuscript writing. The original concept of this Ph.D project was suggested by my supervisor, Dr. Claire Currie. Claire also provided constructive suggestions and interpretation of the modeling results, as well as manuscript writing and editing. The modeling code was developed by Jiangheng He, from the Pacific Geoscience Centre, Geological Survey of Canada. Robert N. Harris provided the heat flow data along the Middle America trench and assisted in the implementation of hydrothermal circulation.

Acknowledgments

This thesis is the result of several years of hard work, and it would not have been possible without the help and support of many people. First and most importantly, I would like to thank my advisor, Dr. Claire Currie, for her guidance, endless patience and encouragement throughout the many years of my Ph.D. Working with her was truly a priviledge. I always felt inspired by her example, dedication and hard work.

All my gratitude to Dr. Jiangheng He, first for creating the code PGCtherm3D, and then for helping me everytime I had questions about it. He was always very supportive, and I could not have done any of this without his help.

To the National Council for Science and Technology of Mexico (CONACYT), for providing the funding necessary to complete this Ph.D.

Many thanks to Dr. Robert Harris for his guidence in implementing hydrothermal circulation in the numerical models and for providing heat flow data. He was always there when I needed help, and for that I am truly grateful.

To my committee, Drs. Moritz Heimpel, Jeff Gu, Long Li, and Glenn Spinelli for their help, support and constructive comments. Their suggestions and insight helped to improve this thesis.

To all the friends I made during my Ph.D. The memories we created during the last few years will never be forgotten.

To my girlfriend Maria, for the cheering, love, and support that kept me motivated to continue working.

To my family. My parents, Carlos and Maria Elena, who have always supported me and believed in me. Through their example, they taught me the importance of dedication and hard work. Their love and encouragement gave me the confidence to pursue my goals. I was truly blessed to have had such amazing parents! To my

brother Luis. His support, love and sense of humor helped me to get through the stressful moments of my Ph.D. To my beautiful grandmother, who always believed in me and always had the right word of encouragement when needed the most. Her infinite prayers were sure listened!

Finally, to my loving God. First, for giving me the strength and confidence to achive this. And second, for giving me the opportunity to be in the right place with the right people to learn from them. Everything I have and everything I achieved, is thanks to Him.

Contents

1 Introduction **1**

1.1 General Structure and Processes Ocurring at the Subduction Factory 2

1.2 Overview of the Thermal Structure of Subduction Zones 5

1.3 Thesis Motivation and Objectives: from 2D to 3D modeling 7

1.4 Outline of Thesis 11

2 Modeling the Thermal Structure of Subduction Zones **13**

2.1 Introduction 13

2.2 Mantle Wedge Dynamics 14

2.2.1 Surface Heat Flow 14

2.2.2 Corner Flow vs Thermal Convection 16

2.3 Numerical Methodology 19

2.3.1 Governing Equations 21

2.3.2 Rheology of the Mantle Wedge 23

2.3.3 Model Geometry and Boundary Conditions 26

3 Benchmarking the Numerical Code **32**

3.1 Introduction 32

3.2 Benchmark Model Setup 34

3.3 Results 36
3.4 Generic Models 38

4 Effect of Hydrothermal Circulation on Slab Dehydration for the Subduction Zone of Costa Rica and Nicaragua 42

4.1 Introduction 43
4.2 Hydrothermal Circulation and Geotectonic Setting 50
4.3 Description of Models 53
4.4 Results 58
4.4.1 Surface Heat flow 61
4.4.2 Dehydration and Metamorphic Reactions 62
4.4.3 Along-Strike Variations 67
4.5 Discussion 68
4.6 Conclusions 74

5 Three-Dimensional Thermal Model of the Costa Rica-Nicaragua Subduction Zone 77

5.1 Introduction 78
5.2 Model Set Up 83
5.3 Results 89
5.3.1 Three-Dimensional Flow Field 91
5.3.2 Three-Dimensional Thermal Structure 94
5.4 Thermal Structure of the Costa Rica-Nicaragua Subduction Zone . . 99
5.4.1 Megathrust Earthquake Seismogenic Zone 99
5.4.2 Slab Temperatures and Eclogitization of the Cocos Plate . . . 104
5.4.3 Mantle Wedge Temperatures and Flow Field 105
5.5 Conclusions 107

5.6 Appendix 110

6 Three-Dimensional Mantle Wedge Flow and Thermal Structure in the Mexican Subduction Zone 116

6.1 Introduction 117

6.2 Model Description 125

6.3 Results 131

6.3.1 Three-dimensional flow field 131

6.3.2 Thermal structure and comparison to two-dimensional models 133

6.4 Mantle Flow and Anisotropy 136

6.5 Discussion 137

6.5.1 Is the Cocos plate fragmented along the OFZ? 138

6.5.2 Tzitzio Gap and termination of the Ultra-Slow Velocity Layer 139

6.6 Summary and Conclusions 142

7 Conclusions 144

7.1 Main Conclusions 145

7.2 Future Work 148

Bibliography 152

List of Figures

1.1 Subduction zones around the world 2

1.2 Subduction zones diagram 3

1.3 Pressure field in 2D corner flows at different angles 8

2.1 Heat transport in a subduction zone and surface heat flow 15

2.2 Generic model created with PGCtherm3D 20

2.3 Dislocation creep viscosity for the mantle wedge. 26

2.4 Diagram of 3D model 27

2.5 Oceanic and backarc geotherms 30

3.1 Velocity field for analytical corner flow and thermal model with isoviscous rheology developed with PGCtherm3D 33

3.2 Finite-element mesh for the benchmark model 36

3.3 Thermal structure of the benchmark model 37

3.4 Geotherms and temperature difference between 3D and 2D codes . . 39

3.5 Generic models 40

4.1 Map of the Costa Rica-Nicaragua subduction zone, with location of 2D models 45

4.2 Several geophysical and geochemical observations in the Costa Rica-Nicaragua subduction zone. 47

4.3 Schematic diagram of 2D models and boundary conditions. 54
4.4 Surface heat flow, thermal structure and hydrothermal cooling of 2D models. 60
4.5 *PT* paths for models with and without hydrothermal circulation. . . . 64
4.6 *PT* paths for all 2D models 66
4.7 Earthquake locations and 2D models of the Costa Rica-Nicaragua subduction zone 70

5.1 Map of the Costa Rica-Nicaragua subduction zone 80
5.2 Schematic diagram of the 3D Costa Rica-Nicaragua model and boundary conditions 84
5.3 2D models with an isoviscous and non-Newtonian rheology 90
5.4 Mantle wedge pressure field and flow direction for the Costa Rica-Nicaragua subduction zone 92
5.5 Mantle wedge streamlines for the Costa Rica-Nicaragua subduction zone 93
5.6 3D thermal model of the Costa Rica-Nicaragua subduction zone . . . 95
5.7 Temperature difference between 3D and 2D model: isoviscous case . . 96
5.8 Temperature difference between 3D and 2D model: non-Newtonian case 97
5.9 *PT* paths for the Costa Rica-Nicaragua subduction zone 101
5.10 Earthquake locations and proposed seismogenic zone for the Costa Rica-Nicaragua subduction zone 102
5.11 Volcanic arc geotherms for profiles A through D in the Costa Rica-Nicaragua subduction zone 106
5.12 Slab geometry of the extended model 112
5.13 Temperature difference between 3D model and extended model for profiles A and B 113

5.14 Temperature difference between 3D model and extended model for profile D 114

6.1 Map of the Mexican subduction zone 118

6.2 Geophysical observations around the Mexican subduction zone and location of the Trans-Mexican Volcanic Belt 123

6.3 Boundary Conditions for the Model from Mexico 127

6.4 Mantle streamlines for the mantle wedge of Mexico 132

6.5 3D thermal structure of the Mexican subduction zone 133

6.6 Along-strike velocity and thermal structure of cross-sections AA' and BB' 135

6.7 Anisotropy and flow direction at a depth of 100 km 138

List of Tables

2.1 Parameters for the Karato and HK viscosities 24

4.1 Material properties and model parameters for the 2D models of the Costa Rica-Nicaragua subduction zone 56

5.1 Material properties of 3D model of Costa Rica-Nicaragua 86

6.1 Thermal properties for 3D model of the Mexican subduction zone. . . 129

Chapter 1

Introduction

For this thesis, I examine the three-dimensional thermal structure of subduction zones. As a tectonic plate moves away from a mid-ocean ridge, it cools and its density increases, therefore becoming gravitationally unstable with respect to the underlying asthenosphere, and thus susceptible to subduction [Cloos, 1993]. Subduction has two major geodynamic consequences. The first one is that it provides most of the force driving plate motions. Forsyth and Uyeda [1975] performed a systematic analysis of plate size and plate motion to show that large, fast-moving plates are always connected to large convergent boundaries with subduction zones, demonstrating that the gravitational potential energy of the downgoing plates provides the dominant force governing plate tectonics. The second major consequence is that subduction of ocean lithosphere serves as the main mechanism for recycling of materials into the depper mantle. Given the variety of processes occurring at subduction zones, the output or by-products of these processes, and their importance for the evolution of the planet, subduction zones are also informally known as *subduction factories*. Figure 1.1 shows the location of most of the subduction zones around the world.

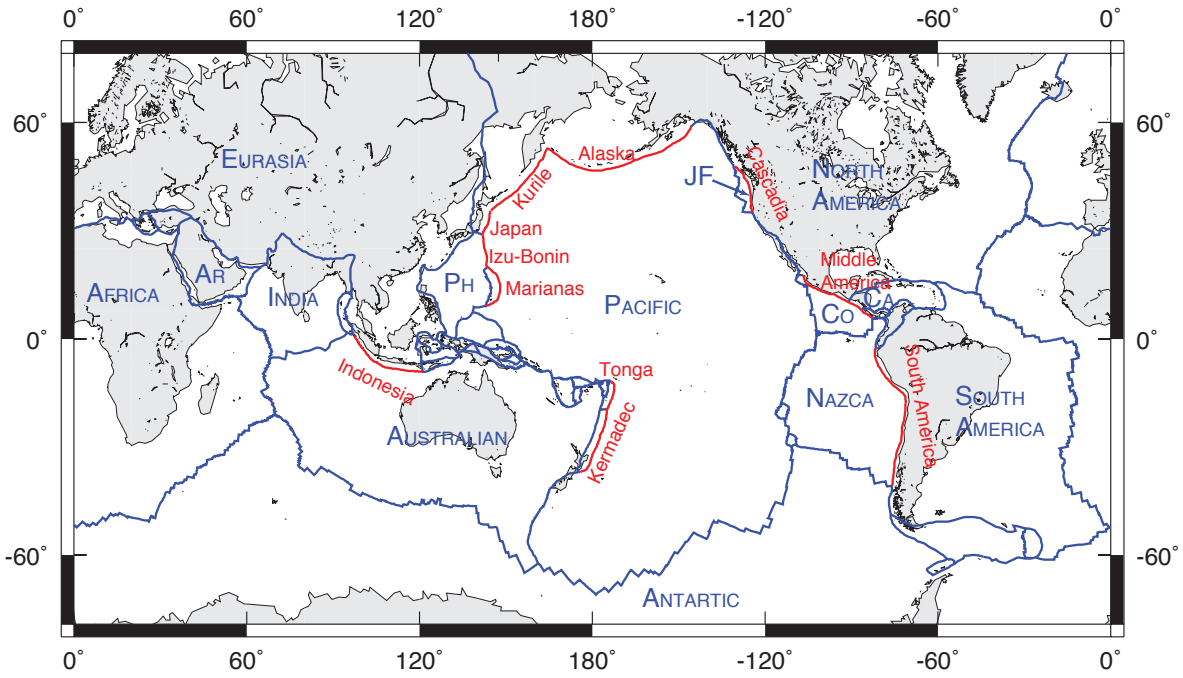

Figure 1.1 Plate boundaries around the world (blue), with main subduction zones shown (red). The name of the subduction zones and most important plates is also shown. AR: Arabian plate; PH: Philippine plate; CO: Cocos plate; CA: Caribbean plate; JF: Juan de Fuca plate. Plate boundaries taken from Bird [2003].

1.1 General Structure and Processes Ocurring at the Subduction Factory

The main components of a subduction zone are the downgoing oceanic plate (referred to as the slab), the upper plate (which can be continental or oceanic), and the mantle wedge. The negative buoyancy of the slab sinks it into the deep mantle; along its way, the slab interacts with the upper plate first and further down with the mantle wedge. The nature of the interaction depends on factors such as the temperature, the velocity of the slab, and the materials that are being carried down by the slab. The structure of a subduction zone and the location of its main processes are shown in Figure 1.2. The slab is the vehicle that transports materials into the deep mantle, and

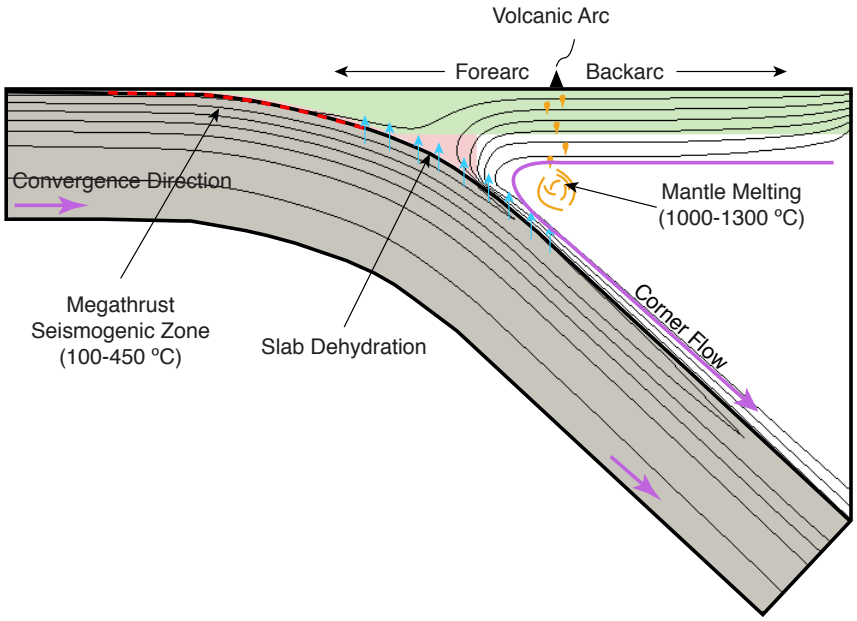

Figure 1.2 Schematic diagram of a subduction zone, with the slab (light grey), mantle wedge (white), and upper plate (light green) shown. Location of principal temperature-controlled processes is shown, including the megathrust seismogenic zone (red dashed line), slab dehydration (light blue arrows), mantle melting (light orange), and arc volcanism (black triangle). The volcanic arc divides the subduction zone into forearc region and backarc region. Serpentinized forearc is also shown (light red). Thick purple arrows show subduction direction and corner flow in the mantle wedge. Due to this downward motion and the low thermal conductivity of the slab, the temperature within the slab (isotherms shown with thin black lines) are depressed with respect to the surroundings.

thus its structure and composition plays a fundamental role in most of the processes occurring in the subduction factory. The slab can be divided into three main sections, namely the oceanic sediments, the oceanic crust, and the oceanic lithosphere. The sediments tend to have a low permeability ($10^{-18} - 10^{-19}$ m^2) with respect to the underlying material [Spinelli et al., 2004], and as such serve as a sealing layer for any water trapped in the hydrated basalts of the oceanic crust. The oceanic crust is composed of several layers of igneous mafic rocks, mostly basalt and gabbro, with a total thickness of 6-8 km [van der Pluijm and Marshak, 2003]. Finally, the oceanic

lithosphere shows an ultramafic composition, with peridotite (specifically harzburgite) being the most abundant rock [Irifune, 1993]. Hydration and serpentinization of the oceanic lithosphere can also occur through long, vertical faults at the outer trench that allow ocean water to penetrate before subduction [Abers et al., 2003; Van Avendonk et al., 2011].

As the slab subducts and is exposed to increasing temperatures and pressure, it releases hydrous fluids along much of its path. In the shallow interface between the slab and the upper plate, it is commonly accepted that dehydration of stable-sliding smectite clays results in a possible transition from aseismic to seismic slip along the subduction interface, representing the updip limit of the *megathrust seismogenic zone* [Hyndman et al., 1997]. This region is the locked portion of the subduction interface, where powerful earthquakes nucleate and nearly 90% of total worldwide seismic energy is released [Stern, 2002]. Although recent experiments suggests that the updip limit may not be entirely temperature-controlled [Saffer and Marone, 2003; Saffer et al., 2012], the megathrust seismogenic zone is typically placed between the 100-150°C isotherms and either the 350-450°C isotherms or the continental Moho, whichever occurs first [Hyndman et al., 1997]. At greater depths, slab dehydration and subsequent hydration of the mantle wedge results in serpentinization of the fore-arc mantle, and a reduction of the solidus temperature of the mantle wedge, leading to melting, magma generation and, ultimately, arc volcanism [Anderson et al., 1978; Furukawa, 1993; Schmidt and Poli, 1998]. From within the plate, dehydration results in the tranformation of the oceanic gabbro and basalts into eclogite, and the triggering of intraslab earthquakes through dehydration embrittlement [Kirby et al., 1996; Peacock and Wang, 1999]. At larger depth (>150 km), water stored in the serpentinized mantle is transported to the deep Earth, affecting the global H_2O cycle [Rupke et al., 2004; Hacker, 2008].

1.2 Overview of the Thermal Structure of Subduction Zones

Given the role of temperature on the processes occurring in subduction zones, the thermal structure of subduction zones has been a recurrent topic in geodynamic modeling. The basic ideas were quickly developed after the establishment of the Plate Tectonic Theory. The first analysis of the thermal structure of a sinking slab was performed by McKenzie [1969], who constructed a generic model with a fixed geometry and a constant subduction rate. Given the low thermal conductivity of the slab, it takes time for it to thermally-equilibrate with the surrounding mantle. The time is proportional to the time scale of heat diffusion, t_d, through the slab:

$$t_d \sim \frac{\rho c_p r^2}{k} \ , \tag{1.1}$$

where ρ is the density of the slab, c_p is the specific heat, r is the length (thickness) scale of the slab, and k is the thermal conductivity. Assuming a thickness of 100 km, typical subduction values for the variables above (see Table 5.1) give time scales in the order of the 100's Myr, indicating subducting slabs are inefficient heat conductors. Depending on the velocity of the plate, the slab can reach a significant depth and still remain cold, leading to a depression of the isotherms around the slab (Figure 1.2). Subduction zones are thus inherently cold and susceptible to brittle failure even at large depths (>300 km).

An important constrain on the thermal structure of subduction zones comes from surface heat flow. As discussed in Chapter 2, surface heat flow shows a steady decrease from the mid-ocean ridge to the forearc, followed by a sudden increase in its intensity landward of the volcanic front [Oxburgh, 1968]. Finite-difference models de-

veloped by Toksoz et al. [1971] showed that a downgoing slab does not reproduce this landward increase, indicating a secondary heat transport mechanism, likely a form of convection, was needed. The concept of two-dimensional (2D) corner flow (Figure 1.2), in which a forced-convection pattern in the wedge due to the drag applied by the downgoing slab, was later incorporated into subduction thermal modeling in order to account for the missing heat source [McKenzie, 1969; Minear and Toksoz, 1970; Andrews and Sleep, 1974]. The drag results from the coupling between the plate and the mantle due to similar strengths in the interface, and is numerically-imposed through a no-slip condition in the mantle interface. The resultant flow field follows a very specific pattern, with mantle coming from the backarc region into the wedge corner.

As it will explained in Chapter 2, 2D corner flow models with a kinematic slab ignore any dynamic factors that might affect the evolution of the slab, as well as any other type of flow mechanism within the wedge (e.g. buoyancy-driven convection). Their advantage is their large resolution inside the slab and in the mantle wedge relative to more dynamic models. Compared to early models, recent 2D corner flow models with a kinematic slab benefited from a better understanding of the incoming plate (better constrained plate motion and slab structure), an improved mantle rheology [Andrews and Sleep, 1974; Tovish et al., 1978; Karato and Wu, 1993; Hirth and Kohlstedt, 2003], and a better understanding of the thermal state of the plate prior to subduction [Stein and Stein, 1992], but were conceptually similar to the first models. 2D corner flow models have also been widely applied to several subduction zones, such as Cascadia [Currie et al., 2004; Wada et al., 2008], Mexico [Currie et al., 2002; Manea et al., 2004; Manea and Manea, 2011; Perry et al., 2016], Central America [Harris and Wang, 2002; Harris et al., 2010b; Wada et al., 2011], Japan [Peacock and Wang, 1999; Spinelli and Wang, 2008, 2009; Spinelli and Harris, 2011], among

others, as well as to infer particular aspects of the thermal and petrological structure [Peacock, 1996; Peacock and Wang, 1999; van Keken et al., 2002; Wada et al., 2008; Wada and Wang, 2009; Rotman and Spinelli, 2013].

1.3 Thesis Motivation and Objectives: from 2D to 3D modeling

Despite the great success of 2D corner flow models, there are indicators that this modeling approach fails to capture the full complexity of wedge flow. 2D corner flow models are usually taken as cross-sections from a subduction zone, with the mantle wedge flow being trench-perpendicular. In reality, however, mantle flow has been observed to have a complex three-dimensional (3D) pattern. Shear-wave splitting studies in subduction zones indicate the mantle wedge flows by the movement of dislocations through crystal lattices in olivine minerals (referred to as dislocation creep) [Long and Silver, 2008]. Assuming the mantle is an a-type olivine fabric in which the fastest direction of the splitted wave, known as the a-axis or fast directions, is aligned with the flow direction, we could expect to see the fast directions to be trench-perpendicular, as in 2D corner flow models. What is observed instead, is that fast directions tend to be more trench-parallel, indicating the 2D corner flow is not fully valid [Kneller and van Keken, 2007; Zandt and Humphreys, 2008; Hoernle et al., 2008; Soto et al., 2009; Stubailo et al., 2012].

Candidates for the generation of lateral (or along-strike) flow that deviates from the fully 2D corner flow are changes in the subduction angle of the slab, curvature of the trench, and an oblique convergence with respect to the trench. Proximity to slab edges and slab windows also induces along-strike flow [Kneller and van Keken,

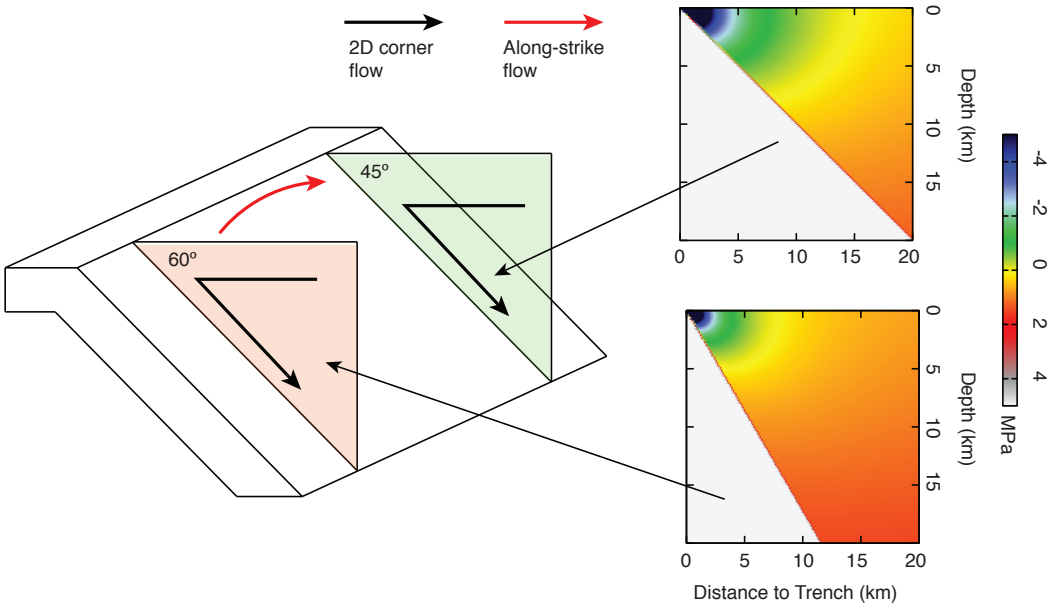

Figure 1.3 Schematic diagram showing the effect of a change in the along-strike angle of subduction. The pressure field comes from the analytic corner flow solution [Turcotte and Schubert, 2002] for a slab subducting at 45° (light green) and 60° (light orange). Red arrow shows direction of induced along-strike flow for such geometry. Color scale is the dynamic pressure.

2008; Bengtson and van Keken, 2012]. To understand the importance of along-strike changes in the subduction geometry, let us analyze the effect of a change in the dip on the wedge flow. For simplicity, I will analyze an isoviscous (constant viscosity) mantle wedge. A general analytic solution for this flow in the case of a slab with constant dip exists [Batchelor, 2000; Turcotte and Schubert, 2002]. The pressure field on such flow is given by

$$P \sim \frac{\eta U}{r} \ , \tag{1.2}$$

where η is the viscosity, U is the plate velocity and r is the distance from the wedge corner. Figure 1.3 shows the pressure field induced by the corner flow for slabs dipping at 45° and 60°. A low pressure region is observed near the corner, with its size depending on the angle of subduction. This low-pressure region is what drives the

corner flow; as the plate subducts, the low-pressure region generated pulls backarc mantle into the corner. If, on top of the corner flow, these two slabs are connected as a single, continous slab, an along-strike, low-pressure channel will appear which will drive flow laterally, from steep dip (small low-pressure region) to shallow dip (large low-pressure region). As heat in the mantle wedge is transferred by advection, we should expect differences in the thermal structure from 2D flow if there is a significant flow component parallel to the strike. It is obvious that the 2D corner flow model may be an oversimplification, as many subduction zones exhibit along-strike changes in slab geometry. In these regions, the thermal state is likely not adequately described by 2D models.

The overarching objective of this thesis is to understand the three-dimensional thermal structure of a subduction zone. Several steps have been taken in this direction by other authors [Kneller and van Keken, 2008; Bengtson and van Keken, 2012; Morishige, 2015; Wada et al., 2015]. However, the effect of along-strike flow on the thermal structure has not been quantitatively addressed in detail. I specifically selected subduction zones along the Middle America Trench (MAT), namely, the Costa Rica-Nicaragua subduction zone, and the Mexico subduction zone. With the exception of the Marianas and the Andes [Kneller and van Keken, 2007], and Japan [Morishige, 2015; Wada et al., 2015], 3D corner flow models of specific subduction zones have not been developed. The MAT was chosen for several reasons:

- There are significant changes in the along-strike geometry of the subducting plate, which changes from flat-slab (subhorizontal) subduction in central Mexico, to a dip of more than 70° in some sections along the MAT [Pardo and Suárez, 1995; Pérez-Campos et al., 2008; Kim et al., 2010; Kyriakopoulos et al., 2015].

- There are significant changes in the along-strike thermal structure of the incoming oceanic plate, due to either changes in its age at the trench [DeMets and Traylen, 2000; von Huene et al., 2000; Barckhausen et al., 2001], or lateral variations in the efficiency of hydrothermal circulation within the oceanic crust[Ziagos et al., 1985; Prol-Ledesma et al., 1989; Harris et al., 2010a].

- A range of observations for the region, including arc magma geochemistry [Carr et al., 2003; Gómez-Tuena et al., 2007; Ferrari et al., 2012; Carr et al., 2014] and seismic anisotropy studies [Hoernle et al., 2008; Soto et al., 2009; Stubailo et al., 2012], indicate along-strike mantle wedge flow.

- There are several 2D thermal models for various sections of the MAT that can be used for comparison with 3D models [Langseth and Silver, 1996; Harris and Wang, 2002; Currie et al., 2002; Manea et al., 2004; Peacock et al., 2005; Harris et al., 2010b; Wada et al., 2011; Manea and Manea, 2011].

The main objectives of this thesis are:

1. To quantify the thermal changes associated with along-strike flow compared to 2D corner models, for both an isoviscous and a non-Newtonian mantle wedge rheology.

2. To investigate the relationship between along-strike flow and the seismic anisotropy pattern in the mantle wedge.

3. To explore the effect of along-strike changes in the thermal structure of the subducting plate, where lateral heat diffusion due to changes in the plate age or the efficiency of hydrothermal circulation could take place.

1.4 Outline of Thesis

The outline of this thesis is as follows. Chapter 2 focuses on the theoretical description of subduction modeling. A brief introduction to the main contraints on the thermal structure, governing equations and boundary conditions used in the models is given. Chapter 3 gives a description of the benchmarking of the modeling code PGCtherm3D. This follows the approach used in benchmarking of the 2D version of the code, PGCtherm2D [van Keken et al., 2008]. Chapters 4 and 5 are research papers that have been through the peer review process, with Chapter 5 already published and Chapter 4 currently undergoing a second revision. Chapter 6 will soon be send to submission.

In Chapter 4, the effect of hydrothermal circulation on the thermal structure of the Costa Rica-Nicaragua subduction zone is explored. In this subduction zone, significant changes in arc geochemistry and mantle wedge hydration are observed [Abers et al., 2003; Carr et al., 2003; Rychert et al., 2008; Syracuse et al., 2008]. These changes correlate with variations in surface heat flux intensity near the trench, which are interpreted to indicate changes in the efficiency of hydrothermal circulation [Harris et al., 2010b]. Our objectives are to investigate if variations in hydrothermal circulation can result in along-strike changes in the thermal structure of the Cocos plate, and to study whether this change may explain the variations in arc geochemistry and wedge hydration. We investigate this through 2D corner flow models, as the effects of wedge flow on the shallow thermal structure are thought to be minimum.

For Chapter 5, a 3D thermal model of the Costa Rica-Nicaragua subduction zone is presented. The effect of along-strike changes in slab geometry on the wedge flow field are explored using an isoviscous and a non-Newtonian mantle rheology. Comparison to 2D models show that corner flow models underpredict temperatures by as much

as 50°C in the mantle wedge, but the flow field does not match the one inferred by arc geochemistry variations [Herrstrom et al., 1995; Johnston and Thorkelson, 1997; Abratis and Worner, 2001; Hoernle et al., 2008]. Our main conclusion is that the thermal structure is controlled by slab rollback and the presence of a slab window in Panama, as opposed to changes in the subduction geometry.

In Chapter 6, I explore the effects of flat-slab subduction on the 3D thermal structure of the Mexican subduction zone. The flat-slab is the most prominent feature of this subduction zone, and several seismic anisotropy studies in the area show trench-parallel flow that departs from the 2D corner flow [Soto et al., 2009; Stubailo et al., 2012]. These studies have been used to make assumptions about the geometry of the Cocos plate, in particular the existence of a gap between the flat-slab and the normal-dipping section. Our results show that the fast axis from seismic anisotropy are mostly aligned with the flow direction induced by a continuous slab, rather than by the presence of a slab gap.

Finally, in Chapter 7, the main conclusions from this work are summarized, and a discussion of possible future directions for 3D subduction zone modeling is given.

Chapter 2

Modeling the Thermal Structure of Subduction Zones

2.1 Introduction

The thermal structure of a subduction zone depends mainly on three factors: (1) the temperature of the oceanic subducting plate, (2) the plate-convergence rate, and (3) the flow pattern of the overlying mantle wedge. The thermal state of the subduction zone is usually characterized by the thermal parameter [Kirby et al., 1996],

$$\phi = Av \sin\theta \ , \tag{2.1}$$

where A is the age of the slab, v is the convergence rate, and θ is the angle of subduction. As thermal conduction dominates heat transfer in the slab, the downward motion of the slab advects cold temperatures to the mantle. Thus, subduction zones with old (cold) and fast-moving slabs tend to have a large thermal parameter, indicating the slab remains cold to large depths. For the mantle wedge, heat is transferred

mainly through advection by solid-state flow.

2.2 Mantle Wedge Dynamics

The flow pattern of the wedge can roughly be classified into two main types: (1) free convection and (2) forced convection.

In free convection, the flow is driven by density differences created by temperature gradients in the vertical direction. We refer to it as thermal convection, or buoyancy-driven flow. For the case of forced convection, the flow is driven by an external mechanism. In the case of the mantle wedge, this external mechanism is supplied by the drag of the downgoing plate. This type of flow is known as the *corner flow* [Batchelor, 2000; Turcotte and Schubert, 2002; King, 2007], and it is shown in Figure 2.1. Under the corner flow, hot mantle from the backarc is brought into the wedge corner, and then dragged down by the slab through viscous coupling. The driving force are pressure gradients created by this the drag, as described in Chapter 4.1.

Although the flow in the wedge is likely a combination of thermal convection and corner flow, corner flow appears to be the dominant mechanism as indicated by surface heat flow observations.

2.2.1 Surface Heat Flow

Surface heat flow shows a very specific pattern in subduction zones [Oxburgh, 1968; Wada et al., 2008]. Due to the cooling effect of the descending oceanic plate, heat flow decreases from the trench to the volcanic arc to reach minimum values of 20-40 mW/m^2. This is followed by a sudden increase near the volcanic arc and into the backarc over a distance of 10-30 km (Figure 2.1), where values of 70-90 mW/m^2 are achieved [Currie and Hyndman, 2006; Wada et al., 2008]. Given the heat sink that

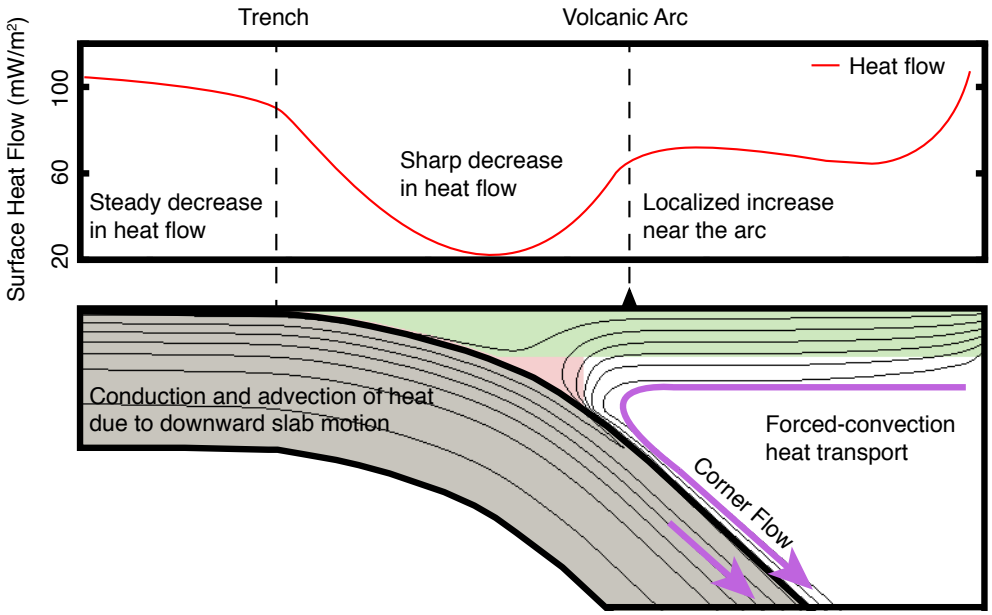

Figure 2.1 Heat transport in a subduction zone and associated surface heat flow pattern. Colors are the same as in Figure 1.2. Locations of the trench and volcanic arc (dashed black lines) are shown. In the slab, heat transport is controlled by conduction and advection due to the downward slab motion. For the mantle, the corner flow dominates, and heat is primarily transported by advection due to fluid motion. For the heat flow, a steady decrease in heat flow before the trench is followed by a sharper decrease due to the cooling effect of the subducting slab. A sudden increase in heat flow is observed near the volcanic arc. This increase is associated with wedge corner flow. As the corner flow does not penetrate to the forearc mantle (pink region), the increase in heat flow is located near the volcanic front.

the slab represents, the increase in surface heat flow near the arc appears puzzling. The low temperatures of the subducted slab with respect to the surrounding mantle suggest the heat flow should continue to decrease into the backarc. Through numerical modeling, it has been demonstrated that the heat flow increase can be explained by heat transport in the mantle wedge in the form of the corner flow that replenishes the wedge corner with hot asthenospheric material from the backarc [van Keken et al., 2002; Currie et al., 2004; Wada et al., 2008].

Surface heat flow also reveals several characteristics of mantle wedge dynamics.

As the increase of heat flow from the arc to the backarc indicates heat advection from the backarc, the low heat flow observed in the forearc indicates the mantle does not flow into the wedge corner tip [Wada et al., 2008; Wada and Wang, 2009]. Forearc stagnation is a consequence of the release of hydrous fluids from the subducting slab, which results in serpentinization of the forearc. This is indicated by an observed 10-20% reduction in seismic speeds from the v_s =4.5-4.8 m/s expected for normal mantle peridotite [Hyndman and Peacock, 2003]. Serpentinization of the forearc leads to a weakening of the subduction interface and a reduction of the drag force imposed on the mantle by the slab. 2D numerical models have shown that a small layer (<1 km-thick) with a reduced viscosity can lead to decoupling between the slab and the mantle wedge, resulting in a surface heat flow pattern similar to that shown in Figure 2.1 [Wada et al., 2008]. The decoupling depth is controlled by the viscosity contrast between the layer and the overlying mantle, and is commonly set at 70-75 km depth. At this depth, the high temperatures required for mantle melting and arc volcanism (¿1100 °C) are met above the point where the slab reaches ∼100 km deep regardless of the thermal structure of the slab (i.e. its age and velocity) [Wada and Wang, 2009]. Surface heat flow thus places an important constraint on the dynamics of the mantle wedge and the thermal structure of subduction zones.

2.2.2 Corner Flow vs Thermal Convection

Although the corner flow pattern explains the regional surface heat flow observations of subduction zones, thermal convection within the wedge may also occur. The models presented in this thesis employ only the corner flow, and therefore it is important to address the issue of whether thermal convection can be neglected when studying the large-scale thermal structure of the mantle wedge.

The physical mechanism of thermal convection is as follows: in a layer of fluid in which the temperature increases with depth, the hotter material at the bottom will expand and reduce its density. This situation is potentially unstable, as the cold and heavier material in the upper part of the layer sits on top of hot and lighter fluid. If this instability is large enough to overcome the viscous resistance of the fluid, the system will tend to reorganize itself to correct the imbalance, and motions within the fluid will develop until equilibrium is restored [Chandrasekhar, 1961].

The onset of thermal convection is expressed through the Rayleigh number:

$$\mathrm{Ra} \equiv \frac{\alpha \Delta T g d^3}{\nu \kappa} \ . \tag{2.2}$$

where α is the coefficient of thermal expansion, ΔT is the temperature difference between the upper and lower boundaries (for the mantle wedge, the upper and lower boundaries would be the continental Moho and the surface of the slab), g is the gravitational acceleration, d is the separation between the upper and lower boundaries, ν is the kinematic viscosity, and κ is the thermal diffusivity. The critical Rayleigh number (at which convection starts) for Equation 2.2 is 657.5 [Turcotte and Schubert, 2002].

To test the possible occurrence of thermal convection in the mantle wedge, first-order estimates of Equation 2.2 can be made. The Rayleigh number depends on several parameters, but it has a strong dependency on the vertical size of the region (the third power of its length, as shown in Equation 2.2). Assuming typical mantle values of $\alpha = 3 \times 10^{-5}$ °C $^{-1}$, $g = 9.81$ m/s^2, $\kappa = 7 \times 10^{-7}$ m$^2/s$, and $\rho = 3300$ km/m^3, the Rayleigh number scales as:

$$\mathrm{Ra} \approx 1.38 \times 10^6 \frac{\Delta T d^3}{\eta} \ , \tag{2.3}$$

where $\eta = \rho\nu$ is the dynamic viscosity. Further, we can take $d = 25$ km, the approximate thickness of the flowing part of the mantle below the volcanic arc (located where the slab reaches a depth of ∼105 km, as noted by Syracuse and Abers [2006]), and a temperature difference of 300°C between both surfaces. Estimates of the viscosity of the mantle rely mostly in geophysical observations, such as postglacial rebound [Haskell, 1935; Peltier, 1974]. From these, the viscosity of the uppermost mantle is inferred to be $10^{19}-10^{21}$ Pa s [Karato, 2010]. Such viscosities would give us a Rayleigh number of ∼640-6, which is below the critical Rayleigh number. Additionally, Wirth and Korenaga [2012] investigated the possible ocurrence of small-scale thermal convection in the mantle wedge of the subduction zone of Japan, and concluded that a viscosity of 10^{18} Pa s is needed for significant thermal convection to occur, consistent with the first-order estimates of the Rayleigh number presented above. The corner flow thus appears to be the dominant mechanism of heat transport in the mantle wedge.

Despite the applicability of the corner flow in the mantle wedge corner, the flow pattern may be more complex in the backarc region. Given the high temperatures (∼1200°C) inferred to exist throughout the backarc, Currie and Hyndman [2006] suggest that a component of thermal convection is also required, as the corner flow alone does not provide the sufficient heat to account for these temperatures. Also, other types of small-scale flow motions may be superimposed on the corner flow, such as the upward motion of fluids and melt that creates the volcanic arc, or localized convection induced by cold plumes or sediment plumes. The transport mechanism of aqueous fluids from the slab into the mantle wedge and the subsequent ascent of melt to the surface is not well-understood [Gerya, 2011]. Fluids from the slab travel several kilometers across the wedge until sufficiently hot mantle is found for melting to occur. Assuming porous flow through the mantle, numerical models have shown these fluids

are transported laterally by the corner flow, suggesting the volcanic arc does not need to be directly above the region where the slab dehydrates, with the specific location of melting depending on factors such as the thermal state of the wedge or the dip of the subducting slab [Cagnioncle et al., 2007]. Once melting occurs, it rises to the surface probably as diapiric upwellings [Hall and Kincaid, 2001]. For the case of cold plumes, they are generated as a Rayleigh-Taylor instability in a hydrated layer above the slab [Gerya and Yuen, 2003]. These plumes are characterized by cold temperatures (300-400°C colder than the asthenosphere) and are driven by compositional convection. Sediment plumes, on the other hand, are the result of the continued subduction of low-density sediments that are not accreted into the accretionary prism [Currie et al., 2007]. The detached elements can later interact with the mantle wedge and intrude the continental lithosphere causing delamination. Foundering of the lower crust also results in a three-dimensional flow field that departs from the corner flow [Behn et al., 2007].

Despite these complexities, it is generally assumed that corner flow dominates mantle wedge motions on a regional scale. In this thesis, I am mostly interested in the thermal structure related to arc volcanism, slab dehydration and seismic activity. These processes occur at or near the wedge corner, where the corner flow dominates, and not in the backarc, where thermal convection can be approximated through the backarc boundary conditions (Section 2.3.3). For this reason, in this thesis I employ the corner flow scheme to model the thermal structure of subduction zones.

2.3 Numerical Methodology

For the modeling of the thermal structure, I employ the finite-element code PGC-therm3D, developed by Jiangheng He from the Pacific Geoscience Centre (Geo-

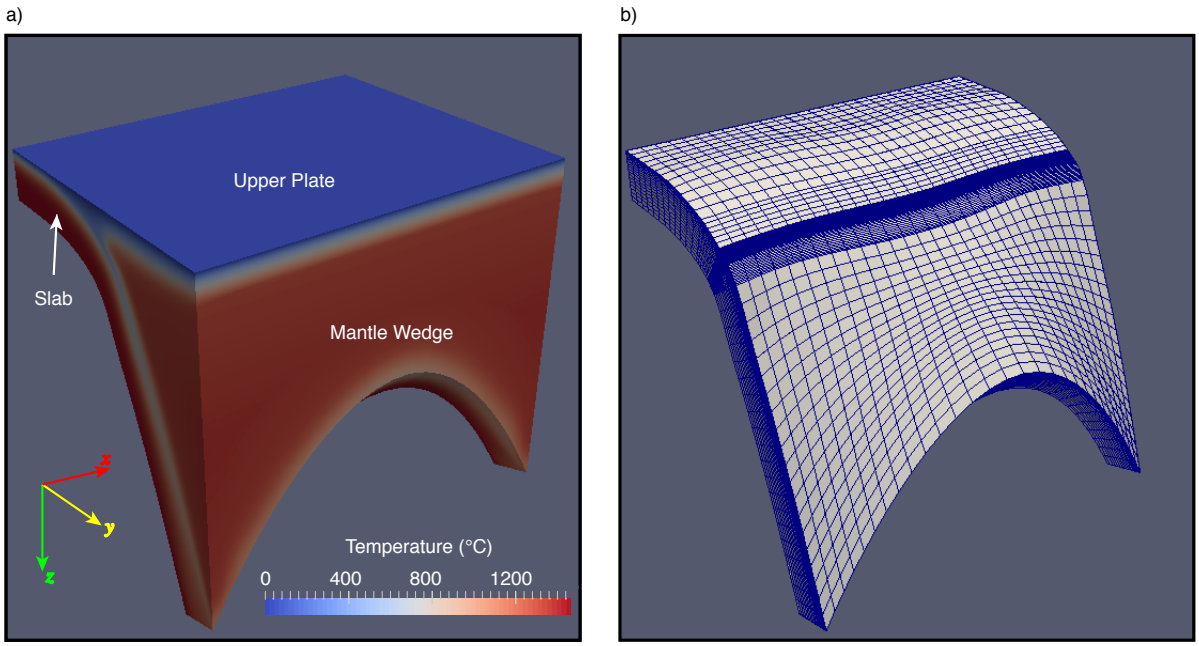

Figure 2.2 **a)** Thermal structure of a generic model of a subduction zone with along-strike changes in the angle of subduction. Main domains are labeled. Cartesian coordinate axis is also shown. **b)** Finite-element mesh of the slab.

logical Survey of Canada). The models presented are steady-state models with a kinematically-prescribed slab (fixed geometry and convergence rate) and a mantle wedge that flows dynamically in response to viscous drag from the slab. While I recognize the existence of fully dynamic models in which the slab is driven by its own buoyancy with respect to the rest of the mantle (e.g Jadamec and Billen [2010, 2012]), the advantage of the kinematic-dynamic approach presented in this thesis is that it allows for a greater resolution in the wedge area and the slab interior, and therefore represents a better choice to investigate the detailed thermal and petrological structure [Billen, 2008].

The model domain is divided into three main units: the slab, the mantle wedge, and the upper plate. Each domain is then divided into isoparametric elements of variable size, ranging from a few meters near the wedge corner to several kilometers

in the backarc and crust. The geometry of all models is such that the x-axis runs in the along-strike distance (subparallel to the trench), the y-axis is the landward distance from the trench, and the z-axis is the depth. Figure 2.2 shows the thermal structure of a generic model and the corresponding finite-element mesh for the slab.

2.3.1 Governing Equations

Using index notation, the governing equations for fluid motion in their most general form, are given by:

$$\begin{aligned} \text{Conservation of Mass:} \qquad \partial_t \rho &= -\partial_i(\rho u_i) \ , \\ \text{Conservation of Momentum:} \qquad \rho(\partial_t u_i + u_i \partial_j u_i) &= \rho F_i - \partial_i P + \partial_j \sigma_{ij} \ , \\ \text{Conservation of Energy:} \qquad \partial_t T + u_i \partial_j T &= \frac{k}{\rho c_p} \partial_i^2 T + \frac{A}{\rho c_p} \ , \end{aligned} \tag{2.4}$$

where ρ is the density, u is the velocity, F are the external body forces, P is the pressure, σ_{ij} is the deviatoric stress tensor, T is the temperature, k is the thermal conductivity, ρ is the density, c_p is the specific heat at constant pressure, and A is the radiogenic heat generated [Schubert et al., 2001].

There is a large number of physical situations in which the governing equations can be simplified. For the mantle, for example, a common simplification is to take the mantle as an infinite Prandtl number fluid. The Prandtl number expresses the ratio of viscous diffusion to thermal diffusion,

$$\mathrm{Pr} \equiv \frac{\text{viscous diffusion}}{\text{thermal diffusion}} = \frac{\nu}{\kappa} \ , \tag{2.5}$$

where $\nu = \eta/\rho$ is the kinematic viscosity (or momentum diffusivity), and $\kappa =$

$k/\rho c_p$ is the thermal diffusivity. A large Prandtl number (Pr>>1) indicates that convection is a more efficient mechanism for heat transport than conduction. The mantle has a kinematic viscosity and thermal diffusivity of 3×10^{17} m^2/s and 7×10^{-7} m^2/s, respectively, and thus the Prandtl number is of the order of Pr $\sim 10^{23}$. This indicates the mantle can be considered as a momentum-free fluid, in which convection dominates heat transport. Through a dimensional analysis [Schubert et al., 2001], it can be shown that such a large Pr (infinite for practical purposes) results in the cancellation of the left-hand-side terms of the momentum equation 2.4. If the mantle is also assumed to be an incompressible fluid (constant density), the governing equations take the form:

$$\begin{aligned} \nabla \cdot \mathbf{u} &= 0 \,, \\ \nabla P &= \mathbf{f} + \nabla \cdot \boldsymbol{\sigma} \,, \\ \partial_t T + \mathbf{u} \cdot \nabla T &= \kappa \nabla^2 T + \frac{A}{\rho c_p} \,, \end{aligned} \tag{2.6}$$

where $\mathbf{f}$ are the external forces divided by the density. The term $\mathbf{f}$ takes different forms depending on what is being investigated. If the Boussinesq approximation is applied (in which density variations are ignored in all terms except on the gravitational force), then the driving force for mantle motion is thermal buoyancy (thermal convection). In that case, the body forces are given by $\mathbf{f} = \alpha \Delta T \mathbf{g}$, where α is the thermal compressibility of the mantle, ΔT is the thermal difference between the upper and lower boundaries (in the case of whole-mantle convection, between the surface and the core-mantle boundary), and $\mathbf{g}$ is the gravitational acceleration. Additionally, buoyant forces due to phase transformation from olivine to wadsleyite ($\alpha \rightarrow \beta$ spinel structure) between the upper mantle and the transition zone (~410 km depth), and from a γ-spinel structure to perovskite and magnesiowustite ($\gamma \rightarrow \mathrm{Pe} + \mathrm{Mw}$) between

the transition zone and the lower mantle (∼660 km depth) can also be incorporated, as they involve a density change of ∼6% and ∼8% for the slab, respectively [Helffrich and Wood, 2001]. For corner flow in subduction zones, the driving force is assumed to be the pressure gradient due to the drag of the slab ($\mathbf{f} = 0$). This is imposed through a no-slip condition along the interface between the slab and the mantle, i.e. zero relative velocity between them (Figure 2.4). If the models are also steady-state, the set of governing equations are:

$$\begin{aligned} \nabla \cdot \mathbf{u} &= 0 \ , \\ \nabla P &= \nabla \cdot (2\eta \dot{\boldsymbol{\epsilon}}) \ , \\ \mathbf{u} \cdot \nabla T &= \kappa \nabla^2 T + \frac{A}{\rho c_p} \ , \end{aligned} \tag{2.7}$$

where $\dot{\boldsymbol{\epsilon}}$ is the strain-rate tensor. Note that, in an incompressible fluid, the deviatoric stress tensor is proportional to the strain-rate tensor through

$$\boldsymbol{\sigma} = 2\eta \dot{\boldsymbol{\epsilon}} \ , \tag{2.8}$$

with the proportionality constant being 2η. Equations 2.7 are the set of governing equations for modeling the corner flow, and these are used throughout this thesis.

2.3.2 Rheology of the Mantle Wedge

Two types of mantle rheology are employed:

1. Isoviscous rheology, with a constant viscosity of 10^{21} Pa s for the mantle wedge.

2. Dislocation creep rheology, under which a deviatoric stress causes the imperfections in the crystal structure of olivine to move across the lattice by dislocating

Table 2.1 Rheological Parameters for the rheologies given by Karato and Wu (1993) (KW; Equation 2.9) and Hirth and Kohlsted (2003) (HK; Equation 2.10)

Rheology	B or D	E (kJ/mol)	n	r	C_{OH} (H/10^6 Si)
KW: wet	28968.6 Pa $s^{1/n}$	430	3.0	–	–
KW: dry	28968.6 Pa $s^{1/n}$	540	3.5	–	–
HK	3.0×10^{-20} Pa^{-n} s^{-1}	480	3.5	1.2	500-3000

succesive atomic layers. For this rheology, two types of effective viscosity can be assigned. The first one employs flow parameters estimated by Karato and Wu [1993], and is given by:

$$\eta = B\dot{\epsilon}^{\frac{1-n}{n}} \exp\Big(\frac{E}{nRT}\Big) \ , \tag{2.9}$$

where B is the pre-exponential factor, E is the activation energy, R is the universal gas constant, and n is the power-law exponent. The second one uses flow parameters estimated by Hirth and Kohlstedt [2003], with the effective viscosity given by:

$$\eta = (DC_{\mathrm{OH}}^{r})^{-\frac{1}{n}} \dot{\epsilon}^{\frac{1-n}{n}} \exp\Big(\frac{E}{nRT}\Big) \ , \tag{2.10}$$

where D is the pre-exponential factor, C_{OH} is the water content in the mantle wedge, and r is the water exponent.

The value for each parameter is given in Table 2.1. Note that because the power-law exponent, n, is different from zero for all cases, substitution of Equations 2.10-2.9 into Equation 2.8 gives a non-linear relation between the deviatoric stress and the strain-rate, indicating the flow under a dislocation creep rheology is non-Newtonian. Figure 2.3 shows the viscosity of the mantle wedge as given by Equations 2.9 and 2.10. As observed, low viscosities within the wedge are focalized through a small

channel into the wedge corner. Below the arc region, there is a thin channel with viscosities as low as 10^{18} Pa s. The top of the wedge develops a high-viscosity region, referred to as the stagnant lid [Currie et al., 2004]. Further away from the arc and into the backarc, the viscosity remains low throughout much of the wedge, although the applicability of the corner flow in this region has been questioned by other studies [Currie and Hyndman, 2006], as discussed in Section 2.2.2.

Equations 2.9-2.10 are similar except in the pre-exponential factors (B vs $(DC_{\mathrm{OH}}^{r})^{-\frac{1}{n}}$). For the viscosity given by Equation 2.9, the values for B, E and n depend on the water content, having specific values whether a dry olivine or a wet olivine (water-saturated) rheology is employed. For the models shown in Chapters 4 and 5, I use a wet olivine rheology. I prefer this rheology over the dry olivine rheology due to the fact that the mantle wedge is expected to be hydrated in Central America due to water released from the subducting slab [Rychert et al., 2008].

In comparison to Equation 2.9, the viscosity given by Equation 2.10 includes a term for the water content, C_{OH}, with values of 500 H/10^6 Si used for a dry mantle, and 3000 H/10^6 Si for a heavily-hydrated mantle [Behn et al., 2009; Goes et al., 2012]. For the models presented in Chapter 6, I employ the viscosity given by Equation 2.10 with a water content of 1000 H/10^6 Si, consistent with mantle attenuation measurements in the region [Chen and Clayton, 2009].

It is important to mention that, from high-temperature studies for the flow of crystalline solids, it is known that diffusion creep is also a valid plastic deformation mechanism for olivine in the mantle [Gordon, 1967]. The current consensus on mantle viscosity is that the uppermost mantle should flow as non-Newtonian dislocation creep. As depth increases, the reduction on the deviatoric stress leads to diffusion creep taking over as the dominant creep mechanism in most of the upper mantle and the lower mantle [Ricard, 2007]. As the models presented in Chapters 4-6 extend

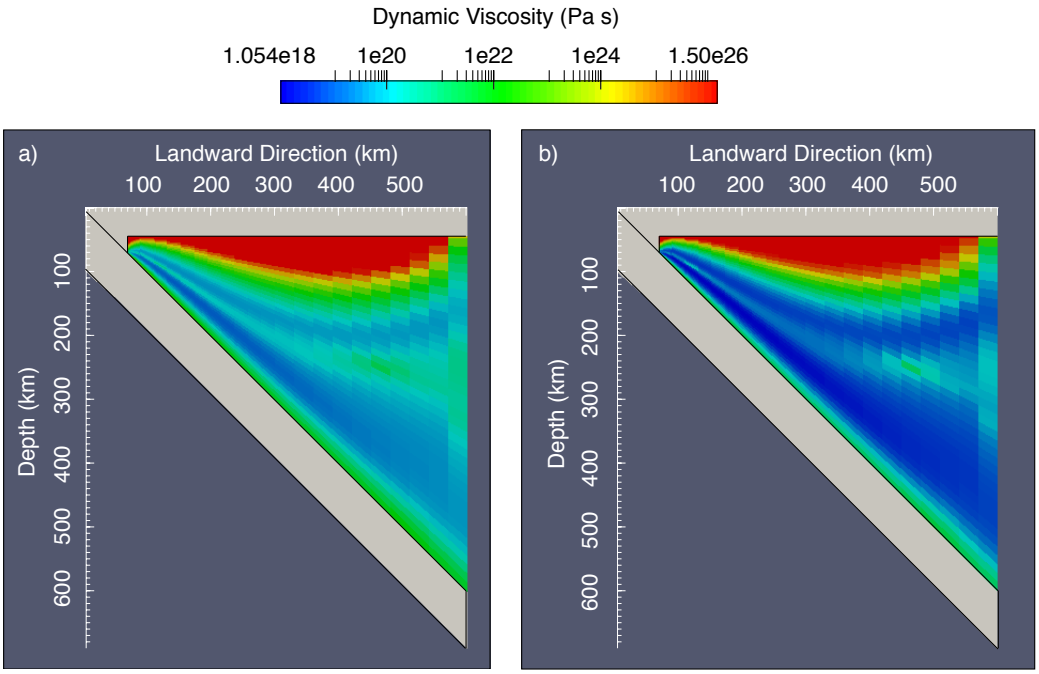

Figure 2.3 Dislocation creep viscosity of the mantle wedge using the flow parameters of **a)** Karato and Wu [1993] for a wet mantle (Equation 2.9), and **b)** Hirth and Kohlstedt [2003] with $C_{\mathrm{OH}} = 1000$ H/10^6 Si (Equation 2.10).

down to depth of 300 km, a dislocation creep rheology is employed throughout this thesis, and not a diffusion creep rheology. Dislocation creep also results in a seismic-anisotropic mantle. Shear-wave splitting studies in subduction zones have shown an anisotropic mantle wedge [Hoernle et al., 2008; Soto et al., 2009; Stubailo et al., 2012; Bernal-López et al., 2015], which further confirms the mantle flows by dislocation creep.

2.3.3 Model Geometry and Boundary Conditions

All models developed with PGCtherm3D have the same design, shown in Figure 2.4. As mentioned in Section 2.3, the x-axis is parallel to the trench, the y-axis is the landward direction, and the x-axis is the depth. The three main sections are

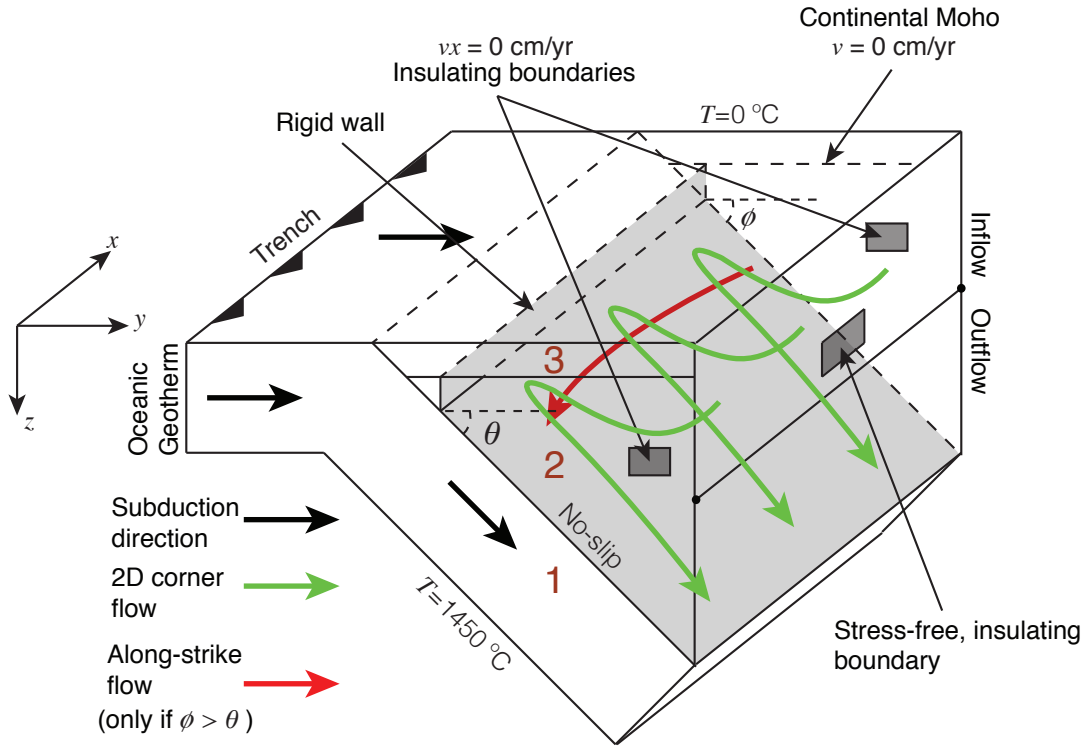

Figure 2.4 Diagram of 3D model, with boundary conditions shown. Subducting slab (1), mantle wedge (2) and upper plate (3) are shown. A no-slip condition between slab and mantle wedge induces 2D corner flow (green arrow); along-strike changes in geometry (for example, changes in angle of subduction θ and ϕ) induces along-strike flow (red arrow).

the subducting slab, the mantle wedge, and the upper plate. The slab is further subdivided in an oceanic sediment layer, a subducting aquifer and the oceanic Moho at a depth of 7 km. The aquifer represents a high-permeability region of the upper oceanic crust in which hydrothermal circulation can take place. The thickness of the sediment layer and the aquifer is different for each model. For the upper plate, the continental Moho is fixed according to the regional characteristics of each model. For the models of Central America, the Moho is placed at a depth of 35 km; for the models of Mexico, is placed at a depth of 40 km.

Finally, a fixed vertical boundary or rigid wall is included near the wedge corner.

This separates the mantle wedge into a stagnant forearc region, and an arc/backarc region which can flow. The wall is consistent with the decay in surface heat flow described in Section 2.2.1, which requires a decoupling between the slab and the mantle beneath the forearc. An alternate way of decoupling the slab and the forearc mantle is provided by Wada et al. [2008], in which a small thin layer with a reduced viscosity is placed along the top of the slab. When the difference in viscosity between the layer and the mantle is high enough, a decoupling occurs. If the viscosity of the mantle is temperaturs-dependent, then the decoupling depth is also thermally controlled as well. Wada and Wang [2009] showed that a common depth of decoupling is 70-75 km to explain the heat flow pattern of most subduction zones. In the models presented in this thesis, the forearc mantle is prevented from flowing by placing the rigid wall at the point at which the slab reaches a depth of 70 km for all models.

The boundary conditions for the model are also shown in Figure 2.4. The upper surface of the models has a zero velocity, while the bottom boundary (bottom surface of the slab) is moving at the convergence rate. A no-flow condition is imposed throughout the rigid wall separating the forearc mantle from the arc/backarc mantle. The corner flow pattern is established through a no-slip condition between the mantle and the slab. At the continental Moho, a no-velocity condition is used for the mantle wedge. The side boundaries are always aligned with the y-axis, with a $v_x = 0$ condition imposed throughout these boundaries. The effect of the side boundaries is discussed for each separate model in Chapters 5 and 6. In general, the $v_x = 0$ condition leads to a thermal structure near the bondaries that resembles that of a 2D model. For the backarc boundary, a stress-free (σ=0) condition is employed. The transition point between the region of inflow and outflow (Figure 2.4) determined dynamically.

For the top ($T(z = 0)$) and bottom of the model, fixed temperature of 0°C and

1450°C , respectively, are used. For the oceanic boundary conditions, a plate-cooling model is employed [Stein and Stein, 1992]. For the models presented in Chapters 4-6, the age of the plate is in the range 11-24 Myr. Two additional factors will affect the oceanic boundary condition at shallow depths. The first one is the effect of sedimentation on the top of the slab. Depending on the rate of sediment deposition and compaction, the thermal gradient near the plate can be affected. The thickness of the sediment layer also plays an important role. For the case of the Cocos plate, the sediment thickness at the trench is 200-400 m. I incorporate the thermal effects of this layer through a numerical algorithm developed by Wang and Davis [1992], based on the theory of heat transfer through sediments developed by Hutchison [1985].

The second factor is the effect of hydrothermal circulation. Hydrothermal circulation refers to buoyancy-driven convection in the porous, high-permeability area below the sediment layer (referred to as the basement aquifer). Water trapped in this area circulates and redistributes heat. I impose a zero vertical thermal gradient for the aquifer, simulating the thermal effects of rapid fluid circulation [Davis et al., 1997], and consistent with what has been done in studies investigating the effect of hydrothermal circulation [Spinelli and Wang, 2009; Harris et al., 2010b; Cozzens and Spinelli, 2012]. The thickness of the aquifer is fixed at 500 m for all models, consistent with previous estimates for the Cocos plate [Harris et al., 2010b]. Figure 2.5a shows a typical oceanic geotherm used in this thesis.

For the backarc boundary, two separate thermal regimes are observed. Within the lithosphere, heat is transported by conduction, I employ an equilibrium geotherm obtained from the heat conduction equation. This equation is given by the energy equation 2.7, assuming all heat is transfered by conduction and a steady-state thermal distribution has been achieved:

$$\partial_z^2 T = -\frac{A}{k} \ . \tag{2.11}$$

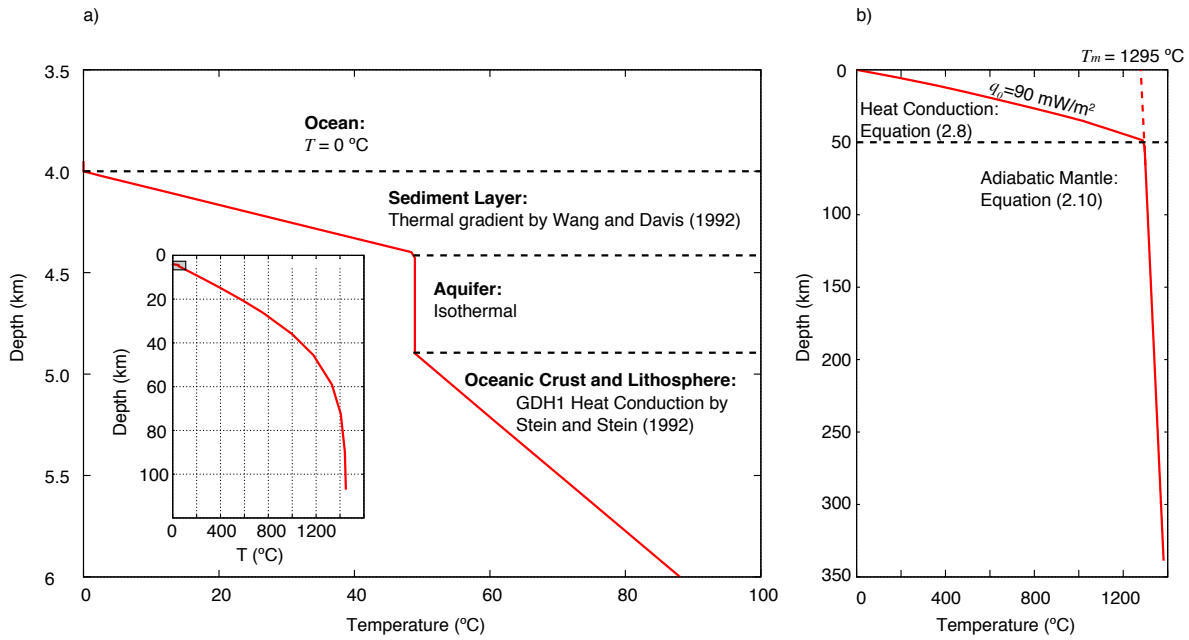

Figure 2.5 **a)** Oceanic geotherm for an oceanic plate age of 20 Myr. Each section is labeled, along with its thermal gradient. The sediment layer has a thickness of 400 m, and the aquifer a thickness of 500 m. Inset shows the oceanic geotherm at large scale. **b)** Backarc geotherm. Thermal regimes for the conductive part of the model (Equation 2.12) and the convecting part of the model (Equation 2.14) are shown. Surface heat flow is set at 90 mW/m^2, and a potential temperature of 1295°C is employed.

In the models presented in this thesis, a surface heat flow, q_0, at the top of the model is assigned (80-90 mW/m^2, as proposed for subduction zone backarcs [Currie and Hyndman, 2006]). This, along with the $T(z = 0) = 0$ condition, gives a solution for Equation 2.11 of the form:

$$T(z) = T_0 + \frac{q_0}{k} z - \frac{A}{2k} z^2 \ . \tag{2.12}$$

If the lithosphere is divided into layers with different thermal parameters (such as the

upper and lower crust), then Equation 2.12 can be coupled with

$$q = q' - A\Delta z \ , \tag{2.13}$$

where q' and q are the heat flow on the top surface and bottom surface of the layer, respectively, and Δz is the thickness of the layer. Equation 2.13 can be substituted into Equation 2.12, with z being the depth with respect to the top of each layer, to obtain a complete geotherm for the entire lithosphere.

For the sublithospheric mantle, I assume an adiabatic thermal gradient. This condition can be derived from very simple thermodynamic arguments [Landau et al., 1959], and is given by:

$$\frac{dT}{dz} = \frac{g\alpha T}{c_p} = 0.3^\circ \text{ C/km} \ , \tag{2.14}$$

where $T = 1427°\text{C}$, $\alpha = 3 \times 10^{-5} °\text{C}^{-1}$, $g = 9.81$ m/s^2, and $c_p = 1.25 \times 10^3$ J Kg/°C , typical values of the upper mantle [Fowler, 2005]. The intersection between Equations 2.12 and 2.14 is emerges naturally by choosing adequate values for q_0 and the potential temperature of the mantle (T_m). The potential temperature is the temperature a fluid mantle element would have it is allowed to rise adiabatically (no heat is lost or gained) to the surface. For the case of Mexico, Manea and Manea [2011] showed that a T_m of less than 1350°C gives backarc temperatures that are consistent with seismic velocities in the mantle. In most thermal models, a T_m of 1295°C is used, consistent with the thermal structure of the mantle near the transitions zone [Ito and Katsura, 1989]. Figure 2.5b shows the complete backarc geotherm.

Chapter 3

Benchmarking the Numerical Code

3.1 Introduction

In this Chapter, I present the benchmarking results for PGCtherm3D. As the code is relatively new and had not been previously used in scientific publications, a necessary step in the thesis project was the proper testing of PGCtherm3D. This process uncovered some errors in the code that had to be fixed before it could be applied to scientific problems. The approach is to compare the results from PGCtherm3D with those obtained using the two-dimensional version of the code, PGCtherm2D.

Benchmarking of PGCtherm2D was performed and reported in van Keken et al. [2008]. For this, the flow, temperature and the pressure field were estimated for a simple subduction geometry (straight slab dipping at 45° with constant convergence rate). Three types of rheology were used: an isoviscous wedge, a wedge that flows by diffusion creep, and a wedge that flows by dislocation creep. For both diffusion and dislocation creep, the flow parameters given by Karato and Wu [1993] were used. In the case of an isoviscous rheology, an analytical solution for 2D corner flow is available [Batchelor, 2000; Turcotte and Schubert, 2002]. As given by Turcotte and Schubert

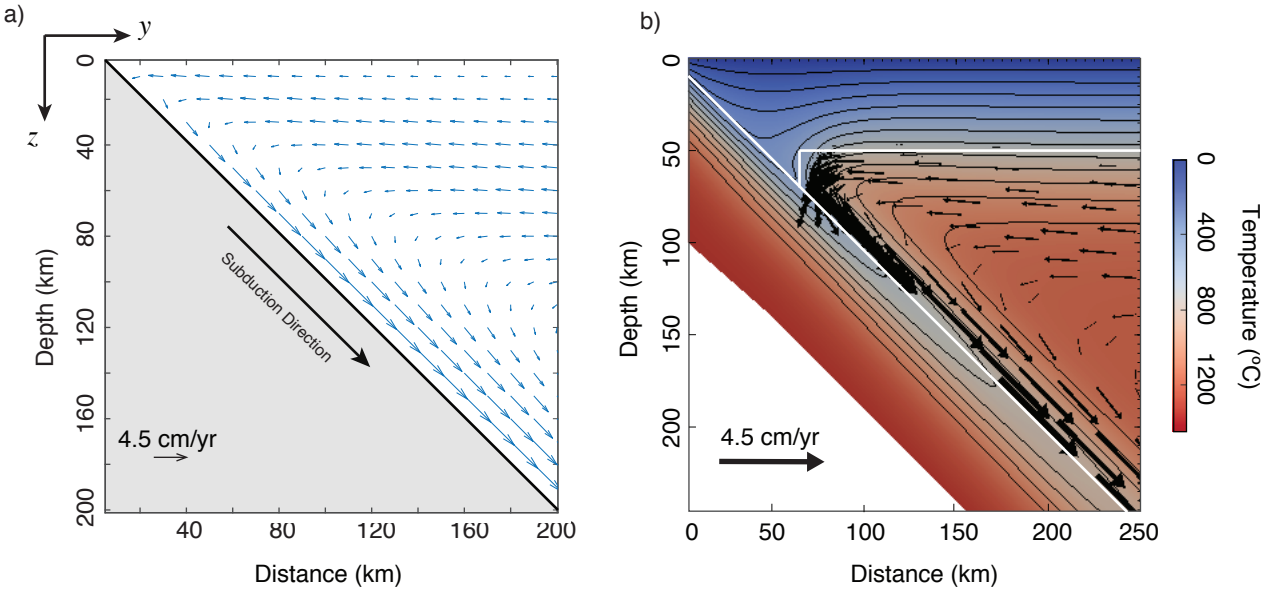

Figure 3.1 **a**: Velocity field for analytical corner flow (blue arrows), as obtained by Equation 3.1. **b**: Thermal model for an isoviscous rheology developed with PGCtherm3D. Solid white lines are the boundaries between the slab, the mantle wedge and the upper plate. Black arrows are velocity vectors for the mantle. Several isotherms with a 100°C spacing are shown. Angle of subduction is 45° and convergence rate is 4.5 cm/yr is used for both models.

[2002], the solution has a streamfunction formulation:

$$\psi(y,z) = (Ay + Bz) + (Cy + Dz)\arctan\left(\frac{z}{y}\right) , \tag{3.1}$$

where ψ is the streamfunction, y is the landward horizontal direction, z is the depth, and A, B, C, and D are constants of integration that depend on the boundary conditions. The flow components along the y and z directions, u_y and u_z, respectively, are related to the streamfunction by $u_y = -\partial_z\psi$ and $u_z = \partial_y\psi$. Figure 3.1a shows the analytical flow field for the benchmark corner flow. For an isoviscous wedge, the flow in the backarc is subhorizontal. As it will be shown in Section 3.3, a disloca-

tion creep rheology results in a flow that is more focalized into the wedge corner. The pressure field is shown in Figure 1.3. The temperature field is obtained through a finite-difference solution of the heat-advection equation with no heat production [Minear and Toksoz, 1970]. The temperature of the analytical corner flow is then estimated at several locations. This can be then compared to the temperatures obtained from numerical codes that use different numerical schemes. A thermal model with an isoviscous wedge is shown in Figure 3.1b. For finite-element codes (such as PGCtherm2D and PGCtherm3D), it was found that a high resolution near the thermal boundaries is needed.

3.2 Benchmark Model Setup

For the benchmarking of PGCtherm3D, I constructed 3D and 2D models that employ a similar geometry than that given by van Keken et al. [2008]. However, the approach is different, as I do not compare the results with those shown in van Keken et al. [2008]. Instead, I calculate the thermal structure of our model with PGCtherm3D, and compare the result with that obtained with PGCtherm2D. As PGCtherm2D has been already benchmarked, similar results between the 2D and 3D codes would indicate the proper functionality of PGCtherm3D.

The geometry of the benchmark model is as follows. In a three-dimensional space, the strike of the trench is aligned with the x-axis, the y-axis is in the landward direction, and the z-axis represents the depth (Figure 3.2). The domain is a cubic box with each side having a length of 600 km. It is comprised of a 45° dipping slab with a constant thickness of 85 km, an overriding continental plate with a thickness of 45 km, and a mantle wedge that is allowed to flow due to the drag of the slab. The fact that the geometry of the slab is constant along the strike ensures a two-

dimensional flow field, allowing for a direct comparison between the 2D and 3D codes. The entire domain is divided into 5776 volumetric elements and 383 surface elements, with smaller elements in the wedge corner. The total number of nodes of 70227. The velocity and age of the slab are 4.5 cm/yr and 8 Myr, respectively. A vertical flow boundary is placed on the wedge, located at the point in which the slab reaches a depth of 70 km, and extending from the surface of the slab to the base of the upper plate lithosphere (Figure 4a). The purpose of this boundary is to prevent the flow from entering the wedge corner, as this would require a very high resolution in this area. Also, in real subduction zones, stagnation of the wedge corner is a required condition to match observations of low heat flow in the forearc and high values near the volcanic arc and into the backarc, as explained in Chapter 2 [Wada et al., 2008].

The velocity boundary conditions on the wedge are constant velocity on the interface between the slab and the wedge and zero velocity on the base of the upper plate lithosphere. For the backarc boundary, I use a no-stress boundary condition. The temperature boundary conditions are given by a half-space cooling geotherm on the oceanic boundary for an oceanic plate age of 8 Myr [Stein and Stein, 1992]. For simplicity, the continental boundary is composed of a linear temperature change from $T = 0$ °C at the surface to $T = 1300$ °C at the base of the continental lithosphere (45 km depth). Below this, a constant temperature of 1300°C is used to a depth of 600 km, consistent with van Keken et al. [2008]. On the surface of the domain ($z = 0$) and bottom of the slab, the temperatures are set to $T = 0$ °C and $T = 1450$ °C, respectively.

For the benchmarking, I use a dislocation creep rheology for dry olivine [Karato and Wu, 1993], with an effective viscosity given by Equation 2.9. The parameters for Equation 2.9 are given in Table 2.1. The governing equations are given by Equations 2.7. I do not include radiogenic heat production ($Q = 0$). For the material properties,

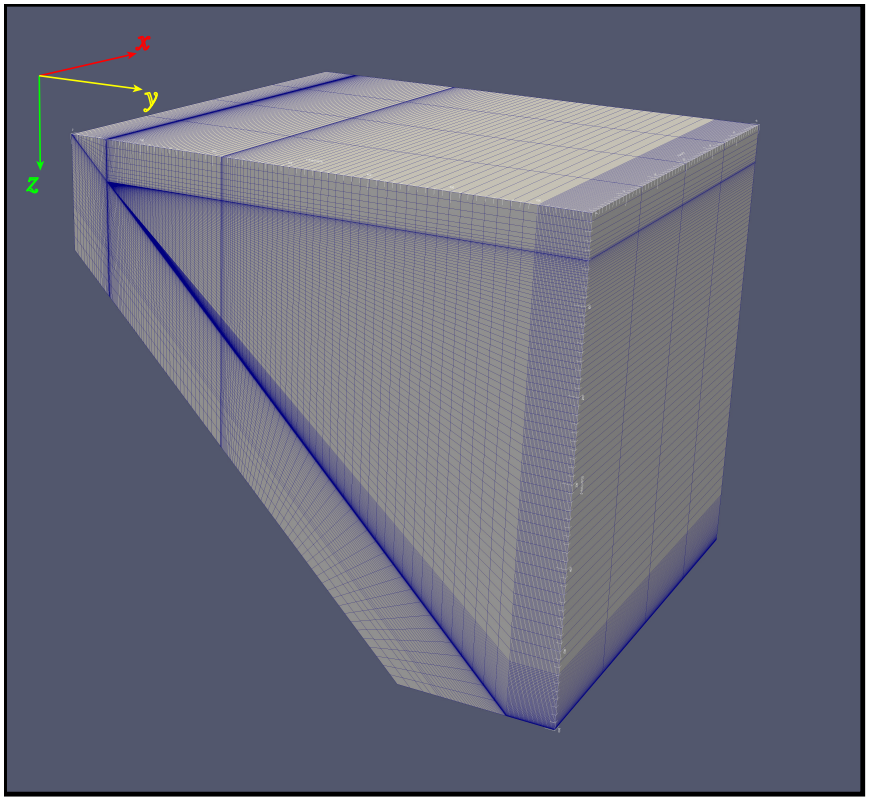

Figure 3.2 Three-dimensional finite-element mesh for the benchmark model. The x-axis is parallel the trench, the y-axis is in the landward direction, and the z-axis is the depth.

I use a constant thermal conductivity of $k = 3.1$ W/mK, a constant density of $\rho = 3300$ kg/m^3, and constant specific heat of $c_p = 1250$ J/kgK for all of the subdomains [van Keken et al., 2008].

3.3 Results

The thermal structure for the benchmark model is shown in Figure 3.3. Qualitatively, the temperature looks as expected for a subduction model: the flow carries heat into the wedge corner and is then dragged down with the slab. The stagnation of the mantle wedge in the backarc at depths <150 km results from the temperature- and

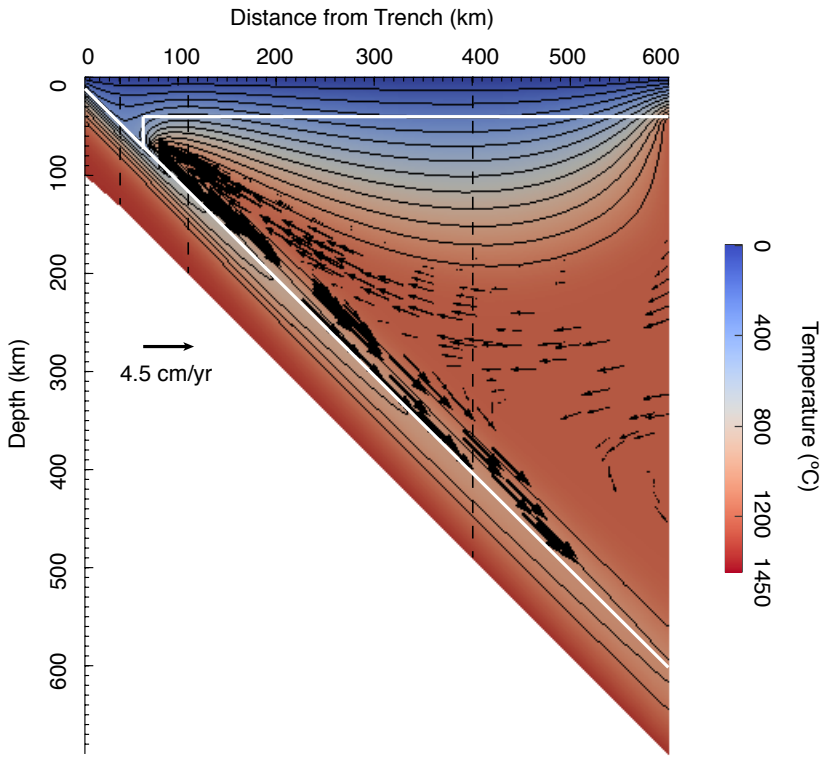

Figure 3.3 2D cross-section through the thermal structure of the 3D benchmark model. A non-Newtonian, dislocation creep viscosity is employed. Solid white lines are the boundaries between the slab, the mantle wedge and the upper plate. Black arrows are velocity vectors for the mantle. Mantle flow is focalized into the wedge corner due to its temperature-dependent viscosity. Thin black lines are isotherms with a separation of 100°C . Dashed lines are the locations shown in Figure 3.4.

stress-dependency of the viscosity of the mantle under a dislocation creep rheology; temperatures at such depths are not hot enough for the viscous mantle to flow. This results in a flow pattern that is much more focalized than for an isoviscous wedge (Figure 3.1), as well as higher temperatures below the volcanic arc.

To quantify the differences between PGCtherm3D and PGCtherm2D, we extract vertical temperature profiles from both models at locations in the forearc ($y = 40$ km), volcanic arc ($y = 110$ km) and backarc ($y = 400$ km). These are shown in Figure 3.4a,

and no significant difference between the models is evident. In the continental crust, there is a linear increase in temperature. For the mantle wedge, the temperature increases to a maximum of ~ 1175°C at a depth of 90 km in the volcanic arc region, and to nearly 1300°C in the backarc. Both profiles show a temperature decrease near the slab surface. The increase in temperature in the wedge is expected, as hot flow is driven into the corner to replace the mantle that is dragged down. The decrease on the surface of the slab is due to the fact that the slab remains relatively cold until greater depths, as conductive heating is slow (see Section 1.2).

Figure 3.4b shows the difference between the three temperature profiles for both codes ($\Delta T = T_{2\mathrm{D}} - T_{3D}$). The agreement between 2D and 3D codes is quite remarkable, never exceeding 8°C (less than 0.7% of the maximum temperature below the volcanic arc) at all depths and locations.

For the isoviscous model with a mantle wedge viscosity of 10^{21} Pa s (not shown), the results show a similar agreement. For an isoviscous wedge results in temperatures < 100°C with respect to a dislocation wedge below the volcanic arc,

In general, the results obtained with PGCtherm3D are comparable (within less than 1%) to those obtained with the 2D code. This demonstrates that PGCtherm3D is an appropriate code for subduction zone modeling.

3.4 Generic Models

The benchmarking results shown in the previous section demonstrates the accuracy of PGCtherm3D. The thermal models developed were consistent with the results given by PGCtherm2D, a code that has already been benchmarked [van Keken et al., 2008], indicating that PGCtherm3D is suitable for subduction thermal modeling.

Once the benchmarking was completed, a second step in the testing of the code

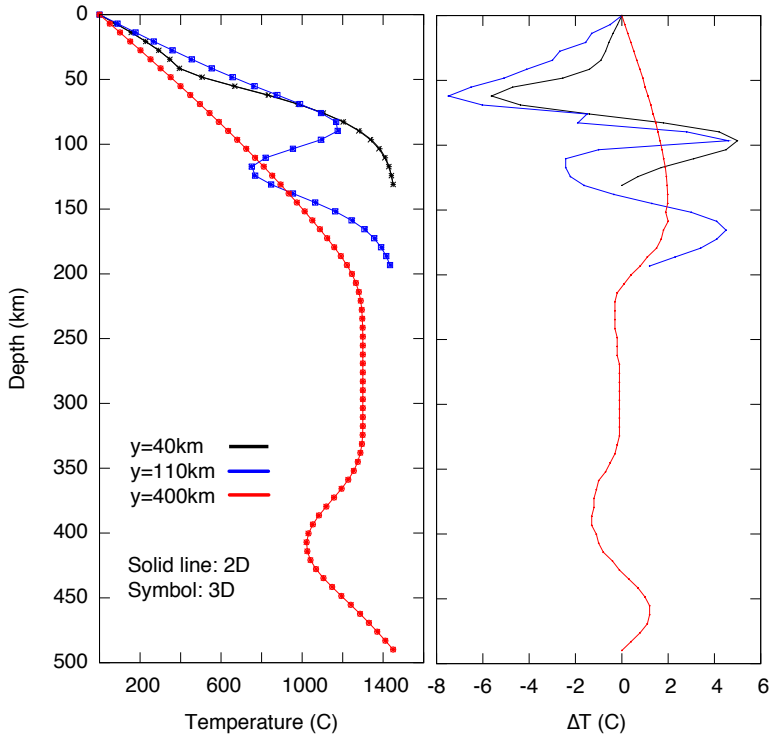

Figure 3.4 **a)**: Geotherms at specific locations (Figure 3.3) for the benchmark model. **b)**: Diferences in temperatures ($\Delta T = T_{2D} - T_{3D}$) in temperatures between PGCtherm2D and PGCtherm3D.

was to develop a series of generic models with several subduction geometries. The objective of the generic models was to gain basic understanding on the limitations and capabilities of PGCtherm3D. Several aspects of the modeling process, such as the generation of a 3D, finite-element mesh of the slab or the proper resolution of the mesh were thoroughly tested. I now briefly described the main conclusions regarding the resolution requirements for PGCtherm3D.

Figure 3.5 shows several of the generic models. Figures 3.5a-3.5c are models with a dip of 45° in the middle section, and with the side boundaries dipping at a different angle. Figures 3.5d-3.5f are models with an along-strike change in the dip across an specific distance. For the models in Figures 3.5a-3.5f, an isoviscous rheology for the mantle was employed. These models showed that a high resolution near the wedge

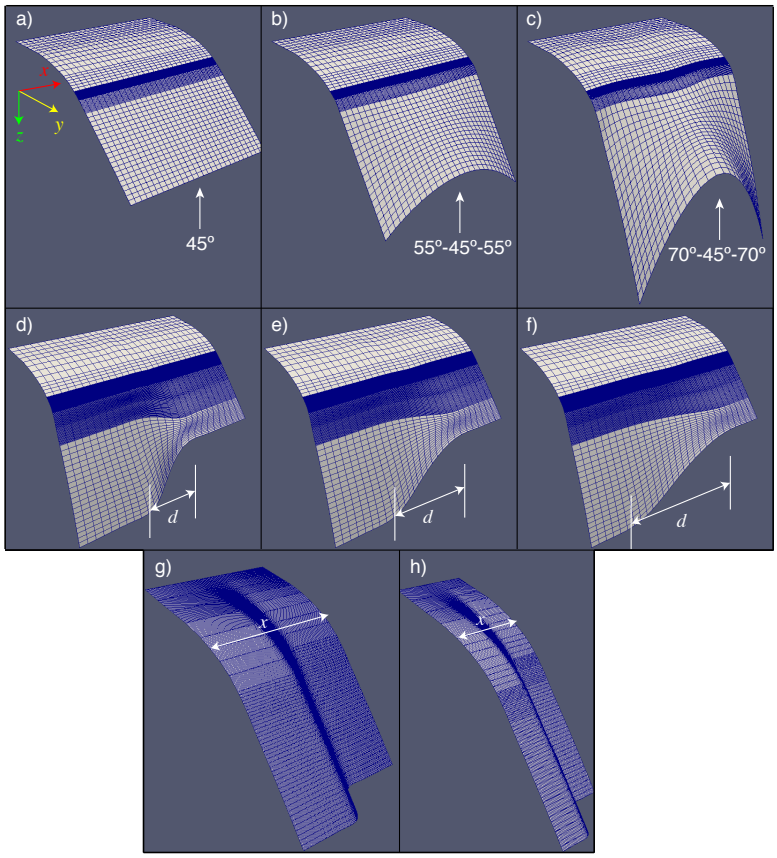

Figure 3.5 Finite-element meshes for generic models. **a)**: Constant dip of 45°. **b)** and **c)**: Dip on side boundaries is 55° and 70°; a dip of 45° is assigned in the middle section for both cases. **d)**, **e)** and **f)**: Along-strike change in the dip from 45° to 75° in a distance $d = 200$ km, $d = 400$ km, and $d = 600$ km, respectively. **g)** and **h)**: Landward shift of 100 km in the location of the mantle wedge with along-strike width of x =400 km and x =200 km, respectively.

corner is needed, with an element size of less than 1 km in the landward (y-axis) direction. In the along-strike direction (x-axis), the width of each element is fixed at 40 km per element.

Figures 3.5g-3.5h are models in which the mantle wedge is displaced forward by 100 km in the y-axis. The along-strike width of the models is 400 km and 200 km. For both models, the element size in the x-axis is 4.75 km, a resolution significantly higher than that used for the models shown in Figures 3.5a-3.5f. The models shown

in Figures 3.5g-3.5h were the first succesfull models to employ a dislocation creep rheology for the mantle wedge, indicating that for a non-Newtonian rheology, a large along-strike resolution (<5 km-width per element in the x-axis) was needed, a result that is consistent with other 3D subduction modeling studies [Kneller and van Keken, 2008; Bengtson and van Keken, 2012; Wada et al., 2015]. The models presented in Chapters 5 and 6 employed a similar element size.

Chapter 4

Effect of Hydrothermal Circulation on Slab Dehydration for the Subduction Zone of Costa Rica and Nicaragua

This chapter has been published.
Rosas, J., Currie, C., Harris, R. and He, J. (2015). *Effect of Hydrothermal Circulation on Slab Dehydration for the Subduction Zone of Costa Rica and Nicaragua.* Physics of the Earth and Planetary Interiors, DOI: 10.1016/j.pepi.2016.03.009

Abstract

Dehydration of subducting oceanic plates is associated with mantle wedge melting, arc volcanism, intraslab earthquakes through dehydration embrittlement, and the flux of water into the mantle. In this study, we present two-dimensional thermal models of the Costa Rica-Nicaragua subduction zone to investigate dehydration reactions within the subducting Cocos plate. Seismic and geochemical observations

indicate that the mantle wedge below Nicaragua is more hydrated than that below Costa Rica. These trends have been hypothesized to be due to a variation in either the thermal state or the hydration state of the subducting slab. Despite only small variations in plate age along strike, heat flow measurements near the deformation front reveal significantly lower heat flow offshore Nicaragua than offshore Costa Rica. These measurements are interpreted to reflect an along-strike change in the efficiency of hydrothermal circulation in the oceanic crust. We parameterize thermal models in terms of efficient and inefficient hydrothermal circulation and explore their impact on slab temperature in the context of dehydration models. Relative to models without fluid flow, efficient hydrothermal circulation reduces slab temperature by as much at 60°C to depths of ∼75 km and increases the predicted depth of eclogitization by ∼15 km. Inefficient hydrothermal circulation has a commensurately smaller influence on slab temperatures and the depth of eclogitization. For both regions, the change in eclogitization depth better fits the observed intraslab crustal seismicity, but there is not a strong contrast in the slab thermal structure or location of the main dehydration reactions. Consistent with other studies, these results suggest that observed along-strike differences in mantle wedge hydration may be better explained by a northwestward increase in the hydration state of the Cocos plate before it is subducted.

4.1 Introduction

Subduction zones are sites where water is recycled into the mantle, making them an integral part of the global H_2O cycle (e.g. Rupke et al., 2004; Hacker, 2008). In the subducting plate, water exists as free water in pore spaces and bound in hydrated basalts in the oceanic crust and serpentine in the oceanic mantle lithosphere. For oceanic crust and mantle, hydration begins at and near mid-ocean ridges through the weathering of basalt and serpentinization of peridotite [Cannat et al., 1992; Kelley et al., 2001; Schroeder et al., 2002; Schmidt and Poli, 2003; Rouméjon and Cannat, 2014]. Hydration continues through the life of the plate and may be enhanced near

subduction zones where plate bending faults at the outer rise provide regions of enhanced permeability [Ranero et al., 2003]. As the plate subducts, increasing pressure and temperature induce several metamorphic dehydration reactions, resulting in water release from the plate. The depth of these reactions is controlled by the thermal structure of the subduction zone. The released water lowers the melting temperature in the mantle wedge above the oceanic plate, inducing melting and arc magmatism [Schmidt and Poli, 1998], as well as intraslab earthquakes through dehydration embrittlement [Kirby et al., 1996; Peacock and Wang, 1999].

In this study, we address slab dehydration for the Costa Rica-Nicaragua section of the Middle-America Trench (MAT). Here, subduction of the Cocos plate is characterized by the rapid convergence of the young (16-24 Myr) Cocos plate below the Caribbean plate, at an average dip angle that changes from $\sim 70^{\circ}$ below Nicaragua to $\sim 45^{\circ}$ below Costa Rica at depths exceeding 60 km. The Cocos plate is generated at two different spreading centers, the East Pacific Rise (EPR) and the Cocos-Nazca Spreading Centre (CNS), with both sides juxtaposed and subducting together offshore the Nicoya Peninsula (Figure 4.1). Subduction in this area is associated with volcanism and the formation of the Central America Volcanic Arc [Carr et al., 2003], as well as megathrust earthquakes along the subduction interface (e.g. Protti et al., 2014). Here, we investigate the relationship between thermal conditions, slab metamorphism and hydration of the overlying mantle wedge. Early studies suggested that there were no significant along-strike variations in the level of hydration of the mantle wedge for the Costa Rica-Nicaragua margin (e.g Carr et al., 2007). However, recent seismic tomography and attenuation studies of the mantle wedge show $P-$ to $S-$ wave velocity ratios of 1.86 and 1.7 and Q_s of 76-78 and 84-88 below Nicaragua and Costa Rica, respectively [Syracuse et al., 2008; Rychert et al., 2008; Dinc et al., 2011]. These results are interpreted to indicate greater hydration of the Nicaraguan mantle.

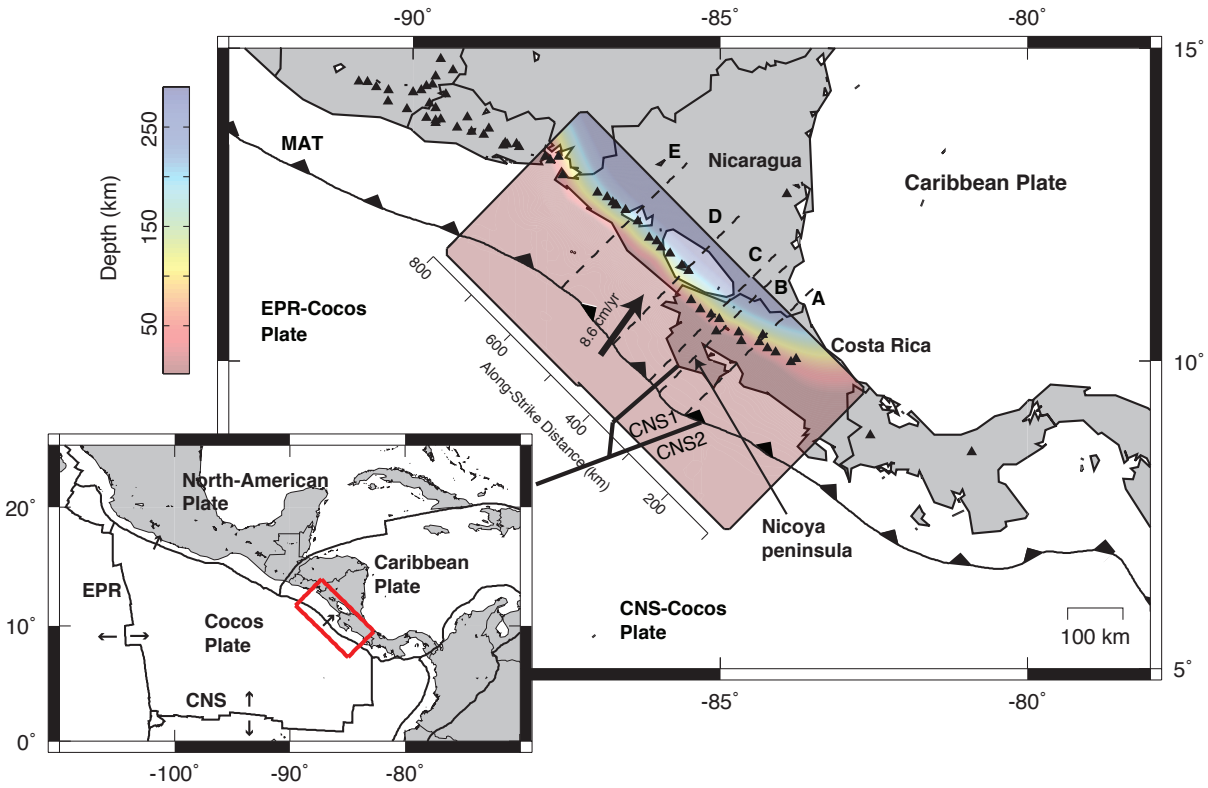

Figure 4.1 Modeling area in Costa Rica-Nicaragua, with the regional tectonics shown in the inset. Color scale denotes slab depth, as obtained from Kyriakopoulos et al. [2015]. Active volcanoes are shown with small black triangles. The Middle America Trench (MAT) runs approximately parallel to volcanic arc. Boundaries between EPR and CNS lithospheres are also shown [Barckhausen et al., 2001]. Locations of profiles A through E are shown by dashed lines, and the along-strike coordinate system in this study is given. Plate boundaries are from Bird [2003].

This interpretation is supported by geochemical studies. Arc magma geochemistry data show that Ba/La and Ba/Th concentrations are relatively low (25-50 and 0-500, respectively) above the CNS section of the subduction zone (Figure 4.2a). Over the EPR section, these values increase steadily to the northwest [Patino et al., 2000], indicating that the arc magmas here are enriched in slab-derived fluids. Both sets of data are consistent with greater slab dehydration in the Nicaraguan part of the subduction zone [Carr et al., 2003].

To explain the trends in mantle wedge hydration and arc geochemistry, two hypotheses have been explored: the slab hydration hypothesis and the thermal hypothesis. The slab hydration hypothesis calls on a variable hydration state of the subducting slab with larger amounts of water at the trench for the EPR side compared to the CNS side of the Cocos plate [Abers et al., 2003; Ranero et al., 2003; Naif et al., 2015]. This extra water is proposed to be bound in the form of serpentinized harzburgite, as indicated by $P-$ wave velocities of 7-7.5 km/s for the uppermost oceanic lithosphere near the trench that are consistent with 20-30% serpentinization [Hyndman and Peacock, 2003]. The increase in water content correlates with a greater number of fault-bending fractures in the outer rise, indicating they might serve as pathways for water to penetrate to depths of $\sim$12 km [Ranero et al., 2003; Van Avendonk et al., 2011].

The thermal hypothesis draws on variations in the along-strike thermal structure of the Costa Rica-Nicaragua subduction zone to explain the variable mantle wedge hydration. In general, the thermal structure of a subduction zone is controlled primarily by the age, convergence rate and geometry of the oceanic slab, as well as the rheology and flow pattern of the mantle wedge above the slab [Peacock, 1996; van Keken et al., 2002]. Peacock et al. [2005] developed two-dimensional thermal models for different sections of the MAT to study slab dehydration and mantle wedge melting. These models are tailored to the age, convergence rate, geometry and material properties of the subduction zone and include a mantle wedge flow induced by viscous coupling with the subducting slab [Peacock, 1996; Batchelor, 2000]. Their models demonstrate that a non-Newtonian mantle rheology is needed to obtain melting temperatures in the mantle wedge. However, age-dependent conductive cooling of the lithosphere yields only small differences in the thermal state of the subduction zone for different sections of the MAT, suggesting minimal along-margin variations

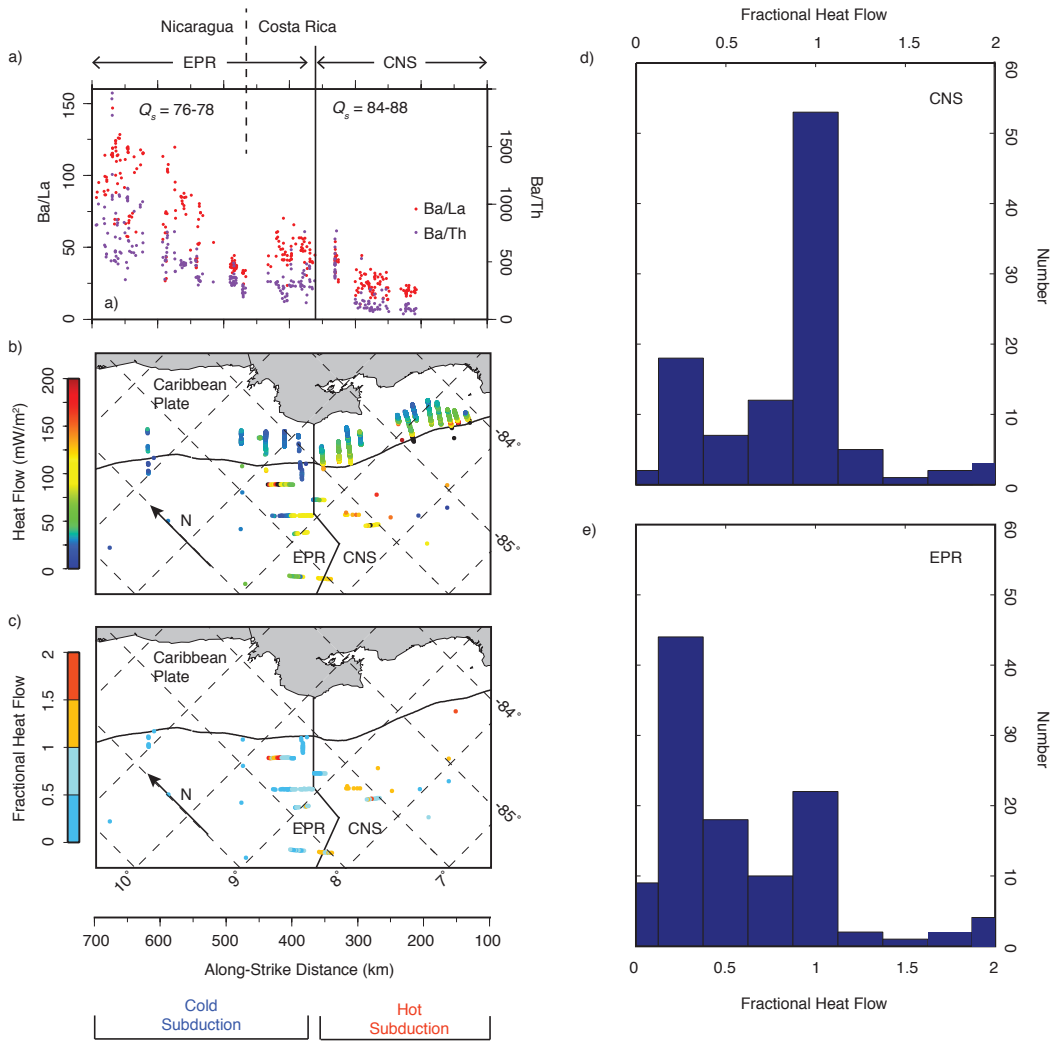

Figure 4.2 **a**: Geochemical ratios Ba/La and Ba/Th from arc magmas along the Central America Volcanic Arc [Carr et al., 2014]. Solid line represents division between EPR-generated lithosphere and CNS-generated lithosphere (see Figure 1). Dashed line represents approximate location of the political boundary between Costa Rica and Nicaragua. Values for mantle wedge seismic quality factor (attenuation) are shown [Rychert et al., 2008]. **b**: Surface heat flow measurements seaward and landward of the MAT. Data from Grevemeyer et al. [2005] and Harris et al. [2010a]. **c**: Fractional heat flow, defined as the ratio of expected heat flow (based on the age of the crust at that location) and observed heat flow. **d** and **e**: Histograms of the fractional heat flow for the EPR and CNS sides, respectively.

in the slab dehydration depth. These models imply that the observed trends in arc geochemistry and mantle attenuation are not associated with variations in typical subduction parameters (e.g., slab age, convergence rate, and slab dip).

However, seaward of the trench, surface heat flow measurements show the impact of hydrothermal circulation (HC) within the oceanic crust [Fisher et al., 2003b; Hutnak et al., 2008; Harris et al., 2010b] which is not incorporated in age-dependent conductive cooling models of oceanic lithosphere. Figure 4.2b shows the available heat flow data landward [Harris et al., 2010a] and seaward [Fisher et al., 2003b; Hutnak et al., 2007] of the trench. CNS-generated crust has a mean and standard deviation of 103 and 75 mW/m^2, respectively. These values correspond to a mean and standard deviation fractional heat flow, defined as the ratio of observed to conductively predicted heat flow, of 0.9 and 0.7 (Figure 4.2c and 4.2d). In contrast, heat flow for EPR-generated crust offshore of the Nicoya Peninsula has a heat flow mean and standard deviation of 69 and 79 mW/m^2, respectively, corresponding to a fractional heat flow mean of 0.6 with a standard deviation of 0.7 (Figure 4.2c and 4.2e). The approximate transition in these heat flow regimes coincides with the plate suture between CNS- and EPR-generated crust (Figure 4.1) but is modified by the proximity of seamounts [Fisher et al., 2003b]. These heat flow distributions appear to reflect different HC regimes for CNS and EPR crust. HC in EPR crust is much more efficient at removing heat than HC on CNS crust [Hutnak et al., 2008] and depends on factors such as crustal permeability, thickness of the crustal aquifer and overlying sediment layer and the distribution of recharge and discharge sites [Fisher et al., 2003b]. In contrast, HC in CNS crust appears to mostly redistribute heat and is largely inefficient at removing heat from the crust.

HC can significantly change subduction zone temperatures [Kummer and Spinelli, 2008; Kummer and Spinelli, 2009; Rotman and Spinelli, 2013], as demonstrated by

thermal models for the Cascadia and Nankai subduction zones that show an increase in the depth of the phase change from oceanic crust basalt to eclogite by more than 15 km [Spinelli and Wang, 2009; Cozzens and Spinelli, 2012]. Harris et al. [2010b] developed models for the Costa Rica-Nicaragua margin that include HC to investigate the shallow thermal structure of the plate interface. By including along-strike changes in the efficiency of HC, these models predict a surface heat flow that is in agreement with the observations. The models also offer a relatively good match with the observed megathrust earthquake distribution, with the rupture area corresponding to the region of the interface between the 100°C isotherm and the continental Moho [Hyndman et al., 1997].

The low surface heat flux on the EPR side and the high surface heat flux on the CNS side suggest contrasting thermal regimes for the Cocos plate; broadly speaking, the EPR side is expected to be cooler than the CNS side. For a given amount of hydration, a colder slab would allow a larger fraction of water to be transported to greater depth [Peacock and Wang, 1999], and therefore, more fluids may be available to hydrate the mantle wedge on the EPR side. The spatial correlation between anomalous surface heat flux and the geochemical trends shown in Figure 4.2 supports this hypothesis.

Harris et al. [2010b] investigated the relationship between HC, surface heat flow, and the temperatures along the shallow subduction interface, but did not address dehydration of the subducting slab. In this study, we extend these models to investigate the effects of HC and mantle wedge flow on slab temperatures for the Costa Rica-Nicaragua subduction zone. Our objectives are: (1) to examine whether HC results in along-strike changes in the thermal structure to depths of 150 km, and (2) to assess whether the changes are large enough to affect the depth of slab dehydration and explain the correlations shown in Figure 4.2. Our models consider only the thermal

structure of the slab and not the presumed along-strike variations in water content of the Cocos plate. If indeed the Cocos plate stores more water along its Nicaraguan section, changes in the thermal structure could aid (or inhibit) slab dehydration.

4.2 Hydrothermal Circulation and Geotectonic Setting

Hydrothermal circulation may affect subduction zone temperatures through heat advection associated with fluid motions in the oceanic crustal aquifer. In this region, vigorous buoyancy-driven convection takes place and is inferred to continue after subduction, provided its permeability remains high [Spinelli and Wang, 2008].

From the top down, the convective system consists of three layers: (1) a sediment layer, (2) the basement or crustal aquifer, and (3) a low-permeability crustal section [Davis et al., 1997]. For the sediment layer, the permeability can be as low as 10^{-19} m^2 [Spinelli et al., 2004]. For the aquifer, in-situ borehole measurements for the upper 500 m of the crust taken in Deep Sea Drilling Project/Ocean Drilling Program (DSDP/ODP) locations in the Pacific give a permeability of $10^{-12} - 10^{-15}$ m^2 [Fisher, 1998]. The underlying sheeted dykes have a permeability estimated to be several orders of magnitude lower ($\sim 10^{-17}$ m^2) that does not support vigorous HC [Anderson et al., 1985]. The low permeability of the sediment layer and the deeper part of the crust creates a sealed environment for the aquifer, where hydrothermal circulation can occur. The intensity of the fluid circulation depends on the Rayleigh number (Ra; the ratio of thermal buoyancy forces to viscous resistance of the fluid), which is given by:

$$\mathrm{Ra} \equiv \frac{\alpha g k L^2 q}{\eta \kappa \lambda} \ , \tag{4.1}$$

where α is the coefficient of thermal expansion of the fluid, g is the gravitational acceleration, k is the permeability of the aquifer, L is the thickness of the aquifer, q is the heat flow at the base of the aquifer, η is the dynamic viscosity of the fluid, κ is the thermal diffusivity of the aquifer, and λ is the thermal conductivity of the aquifer [Wang, 2004]. Numerical modeling of HC within an aquifer suggests that stable, steady-state convection starts at Ra > 40; for non-steady, chaotic convection (which is generally the case in subduction zones), Ra can be $>> 10000$ [Davis et al., 1997]. The specifics of the modeling of HC in this study are given in Section 4.3.

The efficiency of HC in Central America may be linked to the structure of the uppermost Cocos plate. The mean sediment thickness along the MAT is $350 - 400$ m, but the occurrence of basement outcrops in some sections of the Cocos plate results in lateral changes in hydrothermal activity [Hutnak et al., 2007, 2008; Harris et al., 2010b]. These changes are reflected in significant along-margin variations in surface heat flow measurements near the trench. The main transition in heat flow values occurs over an along-strike distance of a few kilometers in front of the Nicoya Peninsula [Fisher et al., 2003b; Hutnak et al., 2007] (Figures 4.1 and 4.2b). The transition approximately coincides with the plate suture between lithosphere generated at the CNS and lithosphere generated at the EPR [Fisher et al., 2003b].

The CNS lithosphere can be divided into two sections: CNS1 and CNS2 [von Huene et al., 2000; Barckhausen et al., 2001]. These domains are a consequence of the break-up of the Farallon plate into the Cocos and Nazca plates in the early Miocene, resulting in a change in magnetic lineation orientations of nearly 20° clockwise [Barckhausen et al., 2008]. The CNS1 section is a smooth-topography, 80 km-wide segment extending from mid-Nicoya to south Nicoya. Further south, the CNS2 section has a rougher topography, with a higher concentration of seamounts. For both sections, the sediment layer is inferred to effectively seal the aquifer [Harris et al., 2010a].

HC operating in systems in which the aquifer is sealed from the overlying ocean has been described as insulated HC [Harris et al., 2010b; Rotman and Spinelli, 2013]. In general, HC along the CNS section of the MAT has a redistributive effect on the subduction thermal structure, tending to homogenize the temperature (see Section 4.4). Figure 4.2d shows an histogram of fractional heat flow for the CNS crust for the locations shown in Figure 4.2c. The results show significant scatter in heat flow values, but the majority of the locations are close to conductive predictions, indicating that HC in this section is inefficient in removing heat from the crust. In addition to the MAT along the CNS section, inefficient HC is inferred to occur along the Nankai, Cascadia and the Queen Charlotte margins [Spinelli and Wang, 2009; Spinelli and Harris, 2011; Cozzens and Spinelli, 2012; Wang et al., 2015]. A general observation is that HC in these regions yields anomalously high surface heat flow near the trench. This results from heat that is advected updip from the deeper subduction zone, which elevates the temperature near the trench and results in strong thermal gradients near the surface (see Section 4.4). For the CNS lithosphere, Harris et al. [2010b] showed that the anomalously high heat flow near the trench (Figure 4.2b) can be explained using thermal models that include this inefficient mode of HC.

North of the plate suture, from mid-Nicoya to Mexico, the subducting Cocos plate consists of EPR lithosphere. Seaward of the trench, the EPR crust is characterized by a large number of highly-permeable ($10^{-10} - 10^{-9}$ m^2) basement outcrops that penetrate through the sediment layer and are exposed at the seafloor [Hutnak et al., 2007, 2008]. Heat flow observations at the outcrops range from 10-50 mW/m^2 to 200 mW/m^2 (Hutnak et al. [2008]). The anomalous heat flow and high permeability of the outcrops indicate that they serve as regions of recharge and discharge of water between the aquifer and the ocean [Fisher et al., 2003a; Hutnak et al., 2007]. Water transport through these outcrops advects heat into the ocean and reduces the tem-

perature in the oceanic crust. HC in systems with ocean-aquifer communication has been referred to as ventilated HC [Harris et al., 2010b; Rotman and Spinelli, 2013]. In contrast to the CNS section, HC along the EPR section is highly efficient at removing heat from the crust, as indicated by the fractional heat flow histogram in Figure 4.2e. The anomalously low heat flow values for the EPR section along the MAT shown in Figure 4.2b [Harris et al., 2010a] result from the cooling of the subducted slab. Thermal models that include this efficient type of HC successfully reproduce the low surface heat flow in this area [Harris et al., 2010b]. Based on the available heat flow data [Ziagos et al., 1985; Grevemeyer et al., 2005] and thermal models [Currie et al., 2002; Perry et al., 2016], this efficient HC may also exist in Nicaragua and Mexico.

4.3 Description of Models

In this study, we investigate the effect of hydrothermal circulation on the thermal structure of the Costa Rica-Nicaragua subduction zone. In particular, we explore whether the difference in the thermal regime between CNS and EPR crust at the trench results in significant along-margin variations in slab temperature deeper in the subduction zone. For this, we use steady-state, two-dimensional (2D) numerical models for the five profiles that are shown in Figure 4.1. Profiles A and B are associated with the CNS crust, and C, D, and E are associated with the EPR crust. These cross-sections correspond, from A to D, to transects SO81-15, SO81-8, BGR99-44, and BGR99-41 of Harris et al. [2010b]. Profile E corresponds to the Nicaragua profile of Grevemeyer et al. [2005]. The geometry of the subducting plate for each profile is from Kyriakopoulos et al. [2015].

The numerical models use a kinematic-dynamic approach, with fixed geometries and velocities for the subducting slab and continental lithosphere. The viscous mantle

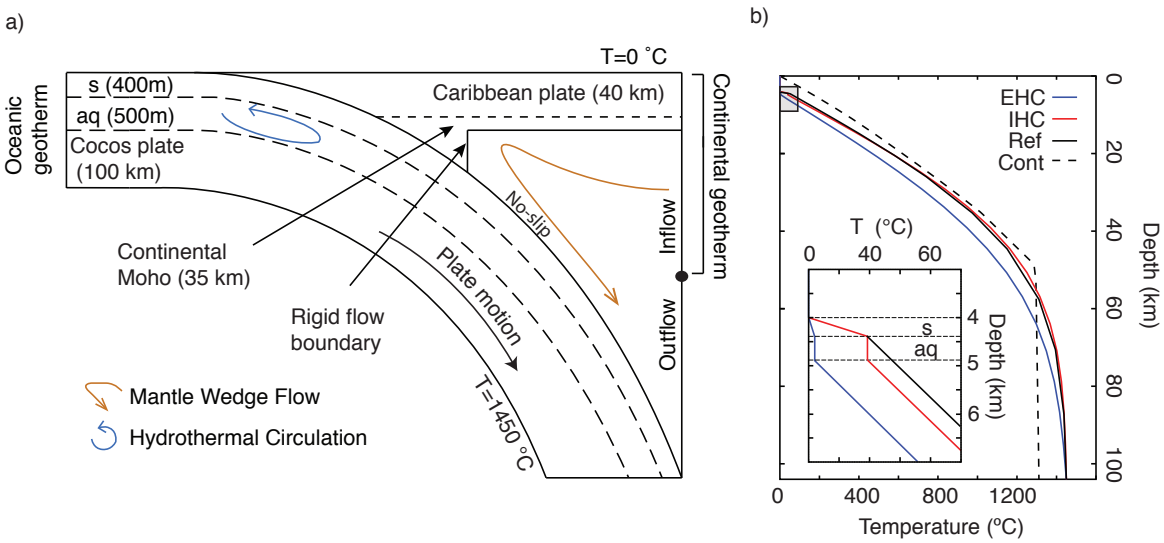

Figure 4.3 **a**: 2D model geometry (not to scale) with main subdomains and boundary conditions. Thicknesses of Cocos and Caribbean plates, as well as the sediment layer (s) and basement aquifer (aq) are shown. Hydrothermal circulation and mantle wedge flow are denoted schematically by blue and brown arrows, respectively. Inflow and outflow transition point on the backarc boundary is also shown. **b**: Typical oceanic geotherms for models with efficient hydrothermal circulation (EHC, blue), inefficientI hydrothermal circulation (IHC, red) and for models without hydrothermal circulation (Ref, black), as well as the backarc continental geotherm (dashed). The inset shows the oceanic geotherms at shallow depths, with sediments and aquifer shown.

wedge flows in response to downward motion of the subducting slab. This sets up a corner flow pattern of wedge flow, which affects the deep thermal structure of the subduction zone [Peacock, 1996; Batchelor, 2000]. The kinematic-dynamic approach allows for high-resolution calculations of the thermal structure of the subducting slab and mantle wedge from the trench to the vicinity of the volcanic arc [van Keken et al., 2002; Currie et al., 2004; Billen, 2008].

Computations are carried out using the finite-element code PGCtherm2D, which has been used in several studies of subduction zone thermal structure [Currie et al., 2004; Wada et al., 2008; Wada and Wang, 2009; Wada et al., 2011; Wang et al., 2015;

Völker and Stipp, 2015] and has been benchmarked [van Keken et al., 2008]. The governing equations for mass, momentum and energy are:

$$\nabla \cdot \mathbf{u} = 0 \ , \tag{4.2}$$

$$\nabla P - \nabla \cdot \boldsymbol{\sigma} = 0 \ , \tag{4.3}$$

$$\mathbf{u} \cdot \nabla T = -\frac{k}{C}\nabla^2 T + \frac{A}{C} \ , \tag{4.4}$$

where $\mathbf{u}$ is the velocity, P is the dynamic pressure, $\boldsymbol{\sigma}$ is the deviatoric stress tensor, T is the temperature, k is the thermal conductivity, A is the radiogenic heat production, and C is the heat capacity. In Equations 4.2-4.4, the mantle is assumed to be a fluid with infinite Prandtl number driven by traction from the downgoing slab. The model domain is discretized using quadrilateral elements of variable size, ranging from a few meters near the wedge corner to several kilometers in the backarc and crust.

The model domain is divided into 5 material subdomains: oceanic lithosphere and crust, sediments, aquifer, continental lithosphere, and mantle wedge (Figure 4.3a). Table 1a gives the thermal properties of each material, following the values used by Harris et al. [2010b]. The sediment layer has a thickness of 400 m for profiles A to D, and 300 m for profile E. The aquifer thickness is 500 m for each model, consistent with previous models of HC in subduction zones and the permeability estimates given in Section 4.2 [Davis et al., 1997; Fisher, 1998; Kummer and Spinelli, 2008; Spinelli and Wang, 2008; Kummer and Spinelli, 2009; Harris et al., 2010b]. In total, the Cocos plate has a thickness of 100 km. For the Caribbean plate, the crustal thickness for all models is 35 km, with 5 km for the mantle lithosphere. This is compatible with the observed Moho depth for Central America [MacKenzie et al., 2008]. The models have the following boundary conditions. The upper plate is stationary and the oceanic

Table 4.1 Material properties and model parameters

Subdomain	Radiogenic heat A (μW/m^3)	Thermal conductivity k (W/m K)	Heat capacity C (MJ/K m^3)
Continental Crust (35 km)	0.2	2.9	3.3
Oceanic Slab (100 km)	0.2	2.9	3.3
Sediment Layer (400 m)	0.2	0.9	2.6
Mantle Wedge	0.02	3.1	3.3

Profile	Age (Myr)	Convergence rate (cm/yr)	HC mode
A (Central Costa Rica)	20	9.3	IHC
B (South Nicoya)	22	9.1	IHC
C (North Nicoya)	24	8.8	EHC
D (North Costa Rica)	24	8.6	EHC
E (Nicaragua)	25	7.9	EHC

plate has a prescribed velocity, using the value in Table 1b for each profile [DeMets, 2001]. Flow in the mantle wedge is driven by the subducting slab. The wedge has a no-slip boundary condition at the contact with the slab and a velocity of 0 cm/yr at its upper boundary. For the forearc mantle, low surface heat flow values suggest that the mantle wedge is stagnant (does not flow), possibly due to serpentinization that decouples the mantle wedge and subducting slab [Wada et al., 2008]. Seismic velocities of 7-7.5 km/s in the mantle wedge corner below Nicoya are consistent with a 20-30%-serpentinized forearc mantle [Hyndman and Peacock, 2003; DeShon and Schwartz, 2004]. To create a stagnant forearc mantle in the models, a no-flow vertical boundary is placed near the wedge corner (Figure 4.3a). The boundary is located at the point where the slab surface is at 70 km depth [Wada and Wang, 2009], and it extends from the surface of the slab to the base of the continental plate.

Shear-wave splitting studies reveal a highly-anisotropic mantle wedge [Long and

Silver, 2008; Long and Wirth, 2013], which indicates that the mantle deformation occurs through dislocation creep. Thus, the mantle wedge in our models has a non-Newtonian rheology, based on the parameters of dislocation creep of wet olivine [Karato and Wu, 1993]. The effective viscosity is given by:

$$\eta = A\dot{\epsilon}^{\frac{1-n}{n}} \exp\Big(\frac{E}{nRT}\Big) \ , \tag{4.5}$$

where $A = 28968.6$ Pa $s^{1/n}$ is the pre-exponential factor, $\dot{\epsilon}$ is the strain rate, $E = 430$ kJ/mol is the activation energy, R is the universal gas constant, T is the temperature, and $n = 3$ is the power-law exponent. At the landward (backarc) boundary, stress-free conditions are used. No heat flow is assumed through this boundary, and the inflow-outflow transition point is determined dynamically (Figure 4.3a)

The top and bottom boundaries of the model have temperatures of 0°C and 1450°C, respectively. The backarc side boundary temperatures are given by a conductive geotherm that intersects a mantle adiabat with a potential temperature of 1295°C. The resulting surface heat flux at this boundary is 90 mW/m^2, consistent with the thermal structure of most subduction zone backarcs [Currie and Hyndman, 2006]. The oceanic thermal boundary condition depends on the age of the oceanic plate and the efficiency of HC [Harris et al., 2010b]. The initial geotherm is given by the GDH1 plate-cooling model [Stein and Stein, 1992], using the plate ages in Table 1b. This is then modified for the effect of HC. For CNS crust (profiles A, B), we prescribe a thermal gradient that incorporates sedimentation and compaction in the sediment layer [Hutchison, 1985]. For EPR crust (profiles C, D, E), water transport between the ocean and the aquifer cools the sediment layer. For this section, we prescribe a thermal gradient of 10°C/km. The aquifer section is assumed to be isothermal, consistent with previous models of Central America [Harris and

Wang, 2002; Harris et al., 2010b]. The deeper oceanic plate employs a normal GDH1 geotherm. Both types of geotherms are shown in Figure 4.3b.

The oceanic geotherm prescribes the temperature along the oceanic boundary depending on the type of HC. Within the aquifer, however, heat is transported by vigorous, non-steady convection. To avoid solving the complex, high-Rayleigh number fluid equations of convective heat transport, we employ a conductive proxy for the aquifer based on the Nusselt number (Nu) [Davis et al., 1997; Spinelli and Wang, 2008; Kummer and Spinelli, 2008; Kummer and Spinelli, 2009; Harris et al., 2010b; Spinelli and Harris, 2011; Rotman and Spinelli, 2013]. Nu is defined as the ratio of convective to conductive heat transport; a high Nu implies that heat is dominantly transported by convection [Wang, 2004]. An empirical relationship between Nu and Ra, given by $\mathrm{Nu} = 0.08\mathrm{Ra}^{0.89}$, was provided by Spinelli and Wang [2008]. Assuming vigorous HC in the aquifer (high Ra), an estimate for Nu can be obtained; the conductive proxy for the aquifer is thus given by $\lambda' = \lambda\mathrm{Nu}$, where $\lambda = 2.9$ W/mK is the original conductivity of the aquifer [Davis et al., 1997]. In this way, a high thermal conductivity is applied to the aquifer in order to model the thermal effects of vigorous convective heat transport. Our models use the proxy parameters given by Harris et al. [2010b] which are based on a regional fitting of the observed offshore surface heat flow for the Costa Rica-Nicaragua subduction zone.

4.4 Results

To study the effects of HC on subduction zone temperatures, we first present thermal models for profiles B and C. These two profiles have different thermal regimes, as they are located to the south and north of the plate suture, respectively. For profile B, the oceanic boundary condition is given by a CNS-type geotherm. For profile C,

an EPR-type geotherm is used. As described in section 4.2, the chosen boundary condition results from the inferred thermal regime for each side of the Cocos plate (Figure 4.2). HC along the EPR side is much more efficient at removing heat than HC along the CNS side. Therefore, for models located on the EPR side, the term efficient HC (EHC) is used; for models located on the CNS side, the term inefficient HC (IHC) is used. For each profile, we compare models with HC to models with no HC. We refer to the models in which there is no HC as the reference models.

Models for profiles B and C are shown in Figure 4.4. For each profile, two models are presented: the reference model and the model with HC. For all models, the temperature distribution has the same general structure as previous subduction zone thermal models (e.g. van Keken et al., 2002; Currie et al., 2004; Peacock et al., 2005). Motion of the subducting plate drags the overlying mantle wedge downward, creating a corner flow pattern. Hot mantle from the backarc replenishes the mantle wedge corner region, elevating temperatures in the wedge and creating a strong thermal gradient along the interface between the mantle wedge and the slab. The forearc mantle seaward of the rigid flow boundary remains cold.

Figure 4.4d shows the thermal effects of HC for each profile, determined by taking the difference between the reference model and the model with HC. For profile B, HC increases the temperature of the oceanic plate near the trench by almost 30°C. This is similar in magnitude to thermal models with IHC for other subduction zones [Spinelli and Wang, 2009; Rotman and Spinelli, 2013]. IHC causes temperatures to decrease by 15-30°C along the subduction interface at depths between ∼15 km and 40 km from the ground surface. For the deep section of the slab, a small drop in the temperature of 10-15°C is observed, and this change persists to large depths. This temperature distribution results from IHC extracting heat from the deeper subducting slab and transporting it updip.

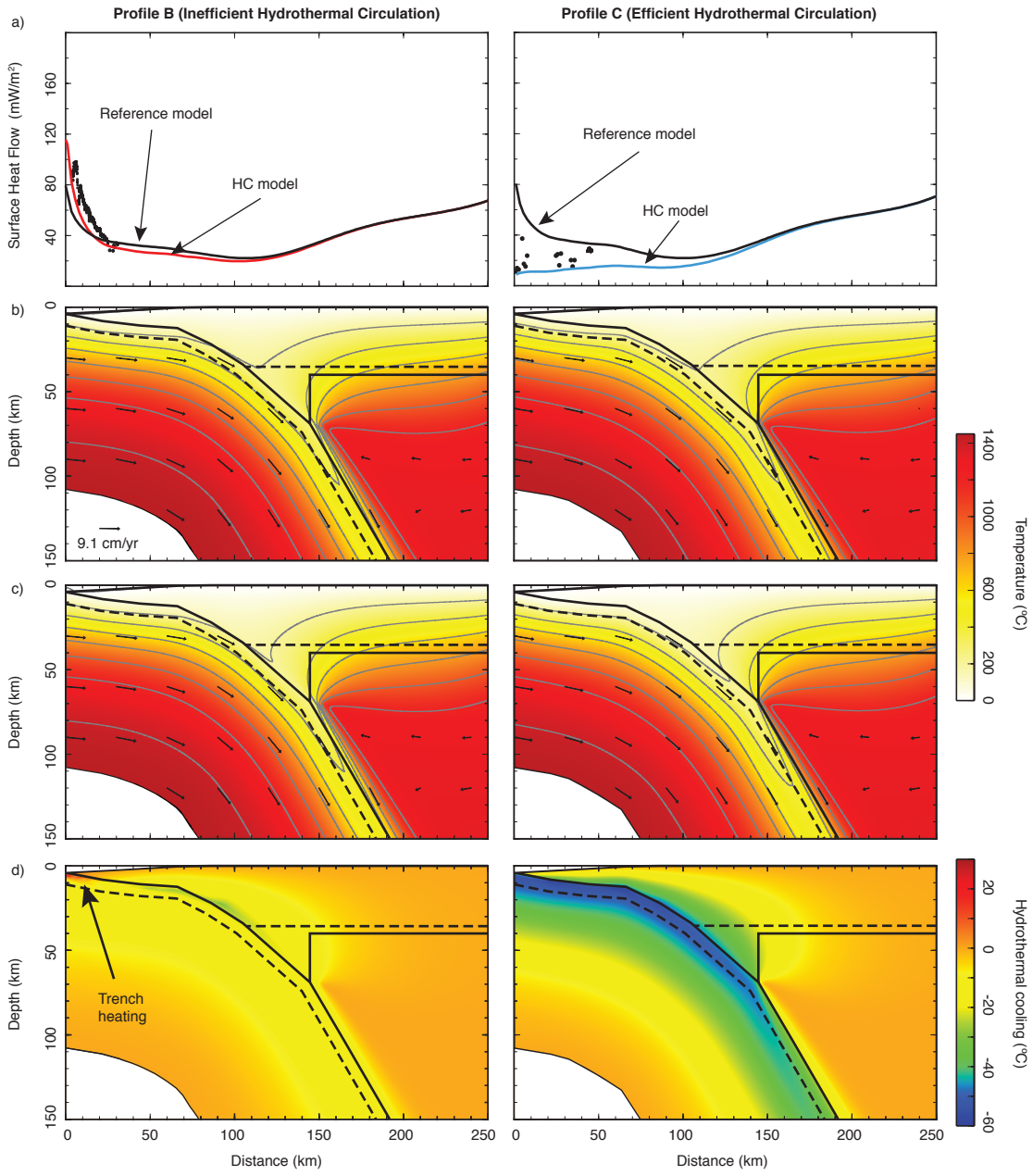

Figure 4.4 Modeling results for profiles B and C. **a**: Surface heat flow for the reference model (black line), IHC model (red line) and EHC model (blue line). Surface heat flow data [Harris et al., 2010a] are shown (black dots). **b** and **c**: Thermal models for the reference case (no HC) and with HC, respectively. Solid lines are plate boundaries, dashed lines are the oceanic and continental Mohos. Temperature contours are every 200°C and flow arrows for the slab and mantle are shown. **d)**: Temperature difference between the reference model and model with HC for each profile. IHC heats the near-trench area but cools the deeper slab. EHC results in cooling of the entire slab.

In contrast, EHC along profile C has a larger effect on subduction zone temperatures. EHC cools the oceanic crust by as much as 60°C at the trench, and this cooling remains to depths as large as 70 km, coinciding with the transition from stagnant to non-stagnant mantle. EHC also affects the oceanic mantle lithosphere, with temperatures dropping by 40°C to a depth of 40 km below the surface of the slab. Similar to IHC, the temperature change persists to depths > 150 km. Unlike IHC, EHC lowers subduction zone temperatures throughout the slab due to the colder (ventilated) oceanic plate prior to subduction.

4.4.1 Surface Heat flow

Figure 4.4a shows observed heat flow data [Harris et al., 2010a], as well as the modeled heat flow curves for the reference models and models with HC for profiles B and C. For the reference models, the modeled heat flow decreases landward of the trench owing to conductive cooling of the overlying material by the cold subducting plate. Heat flow then increases landward of the stagnant mantle wedge corner as the mantle wedge is heated by induced corner flow [Currie and Hyndman, 2006; Wada et al., 2008]. For both profiles, the surface heat flow for the reference models does not agree with the observations.

In contrast, models with HC offer a better fit to heat flow values. For profile B, the inclusion of IHC increases the surface heat flow at the trench by 30-40 mW/m^2. This results from enhanced heating of this region by HC, as described above. IHC also creates a steeper decrease in heat flow landward of the trench. Both the high trench heat flow and landward decrease provide a better fit to the observed heat flow. For profile C, EHC causes a more uniform drop in slab temperatures, which results in low heat flow of 10 to 20 mW/m^2 for the trench and forearc region. This is in

relatively good agreement with the observed heat flow.

Our modeled heat flow curves are consistent with previous models of Central America that include HC [Langseth and Silver, 1996; Harris and Wang, 2002; Harris et al., 2010b]. In our models, HC is implemented using the parameters of Harris et al. [2010b], based on a regional analysis of the offshore surface heat flow. As our focus is on the deeper slab temperatures, we do not attempt a detailed fit of the heat flow on the profiles in our study. In addition, this approach does not incorporate local areas of heat exchange between the ocean and seafloor, which may explain some of the scatter in the observations on profile C.

4.4.2 Dehydration and Metamorphic Reactions

We now use the thermal models to evaluate the predicted depth of metamorphism and dehydration of the subducting Cocos plate for profiles B and C. Figure 4.5 shows pressure-temperature (PT) paths for the top of the oceanic plate, the oceanic Moho (7 km below the slab top), and a surface 12 km below the top of the slab (i.e, within the oceanic mantle lithosphere). These paths are superimposed on phase diagrams for mid-ocean ridge basalt (MORB) and harzburgite [Hacker et al., 2003], the main components of the oceanic crust and the uppermost lithospheric mantle [Irifune, 1993]. For the oceanic crust, metamorphic reactions ultimately transform basalt into several eclogite facies, releasing a substantial amount of fluid, increasing the density of the slab, and facilitating the occurrence of intraslab earthquakes [Kirby et al., 1996]. For the oceanic mantle lithosphere, hydration of harzburgite leads to serpentinization of the mantle. Serpentinite carried in subducting slabs is generally stable until significant depths ($>$ 60-70 km) for most subduction zones [Schmidt and Poli, 2003]. Depending on the temperature and pressure, the oceanic mantle may

later undergo dehydration. In general, water trapped in serpentinized harzburgite may be the most efficient transport mechanism of water to the deep mantle [Rupke et al., 2004].

Oceanic Crust

Owing to the effect of HC on slab temperatures observed in Figure 4.4, changes in the depth of dehydration could occur. To quantify this effect, PT paths for the top (solid line) and bottom (dashed line) of the oceanic crust are shown in Figures 4.5a and 4.5b for profiles B and C, respectively. Here, it is assumed that the crustal phase changes happen as soon as the required PT conditions are met, i.e, we are not considering sluggish kinetics. This assumption is common in the analysis of subduction zone thermal models [Peacock and Wang, 1999; van Keken et al., 2002; Peacock et al., 2005; Cozzens and Spinelli, 2012]. In reality, it is not clear if thermodynamical equilibrium is fully valid, but textural data indicates kinetic hindrance of the uppermost crust may not be significant, although retardation has been observed for the deeper, gabbroic rocks [Hacker, 1996].

For both profiles, the models with HC are cooler than the reference models at depths less than 50 km, with profile C experiencing a greater hydrothermal cooling. The maximum hydrothermal cooling is approximately 30°C and 60°C for IHC and EHC models, respectively, and it is reached at 15-20 km depth. The temperature change tends to decay with depth, but for the EHC model, a relatively large cooling (> 30°C) persists to greater depths.

As the plate subducts, it undergoes several metamorphic reactions that release water. At shallow depths, the top of the slab goes through lawsonite blueschist (LB), jadeite lawsonite blueschist (JLB), and lawsonite amphibole eclogite (LAE) facies for profiles B and C. The water content for these facies is between 7 and 15 wt%. The

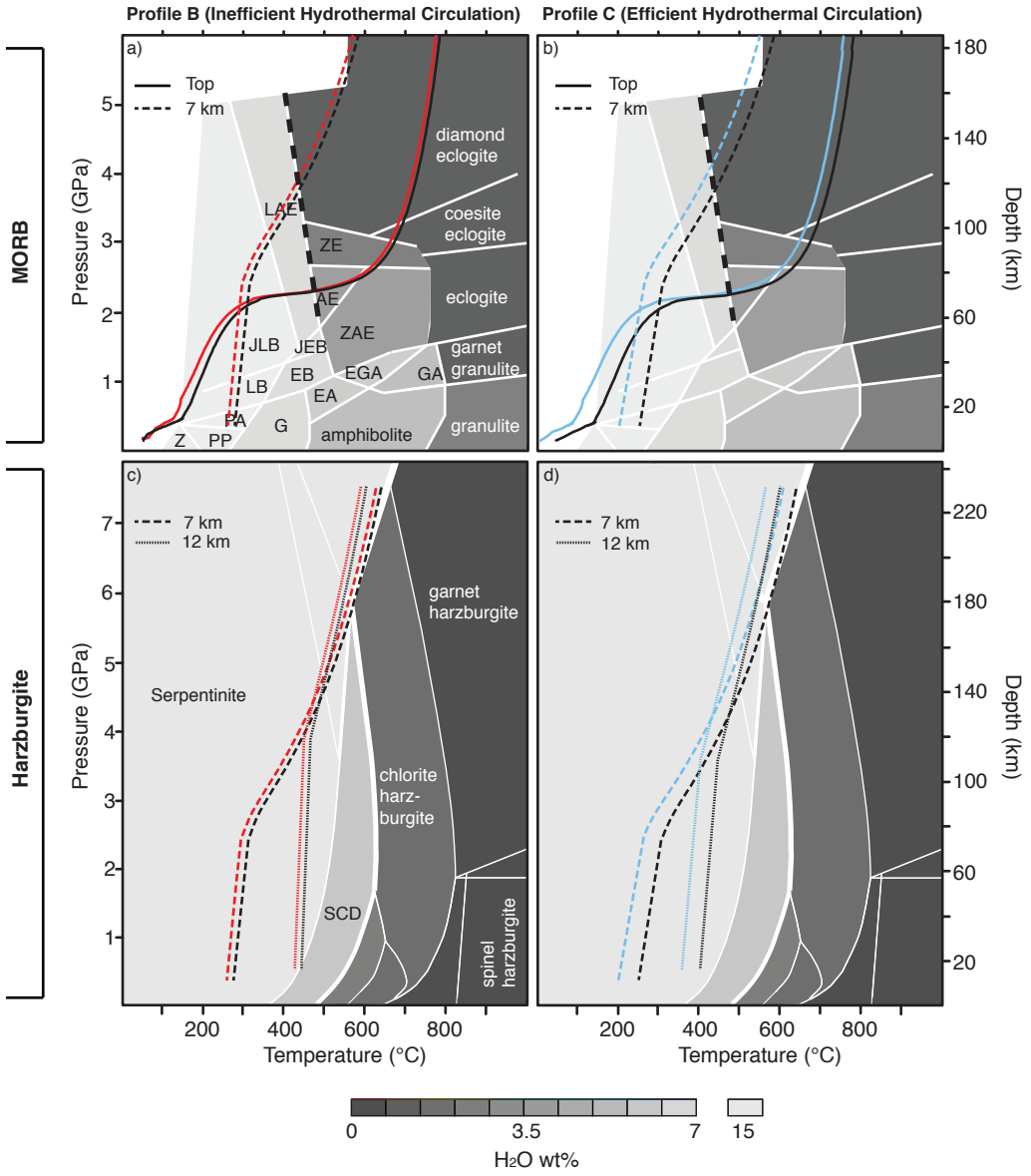

Figure 4.5 *PT* paths for the oceanic crust (**a** and **b**) and the oceanic lithosphere (**c** and **d**) for profiles B and C. Paths are for the top of the oceanic crust (solid line), for the oceanic Moho (dashed line) and a surface located 12 km below the slab top (dotted line). The black lines are the reference models; the blue line is the model with IHC and the blue line is the model with EHC. Thick dashed line shows location of major dehydration pulse. *PT* paths are superimposed on the phase diagrams for MORB (top row) and harzburgite (bottom row), from [Hacker et al., 2003]. The gray shading indicates the water content in each phase. Metamorphic facies: AE, amphibole eclogite; EA, epidote amphibolite; EB, epidote blueschist; EGA, epidote garnet amphibolite; G, greenschist; GA, garnet amphibolite; JLB, jadeite lawsonite blueschist; JEB, jadeite epidote blueschist; LAE, lawsonite amphibole; JLB, jadeite lawsonite blueschist; LB, lawsonite blueschist; PA, prehnite-actinolite ;PP, prehnite pumpellyite; SCD, serpentine chlorite dunite; Z, zeolite; ZE, zoisite eclogite; ZAE, zoisite amphibole eclogite.

addition of HC slightly modifies the depth of these dehydration reactions for the top of the oceanic crust with respect to the reference models. For the profile B, IHC increases the depth of dehydration by approximately 10 km, where it enters the JLB facies. For profile C, crustal dehydration starts nearly 25 km deeper than in the reference model.

The most important reactions in Figure 4.5 are the transformation to diamond eclogite, zoisite eclogite (ZE), and amphibole eclogite (AE), at which point the crust experiences significant dehydration and has ≤ 3 wt% water. This is shown on Figure 4.5a by a thick dashed line. For both profiles with HC, the top of the crust enters the amphibole eclogite (AE) field at 65 km depth. The depth of this transition is similar to that in the reference models. This is because at this depth the slab is in contact with the mantle wedge, and the temperatures at the surface of the slab are now mostly controlled by the corner flow.

For the bottom of the crust, profiles B and C enter the diamond eclogite facies at a depth of $\sim$115 km in the reference models, at which point the modeled slab is completely dry. For models with HC, there is a moderate increase in the depth of this transition. Our profile B predicts a completely dry crust at no more than 5 km deeper than the reference model. For profile C, the change is larger, with transformation to diamond eclogite occurring $\sim$15 km deeper than that in the reference model. The depth at which the crust transforms to diamond eclogite is referred to as the depth of complete eclogitization of the crust (full crustal dehydration).

Oceanic Mantle

Figures 4.5c and 4.5d show the *PT* paths for the oceanic Moho (dashed line) and a surface located 12 km below the top of the slab (dotted line) for profiles B and C, respectively. These are compared to the phase diagram of harzburgite [Hacker et al.,

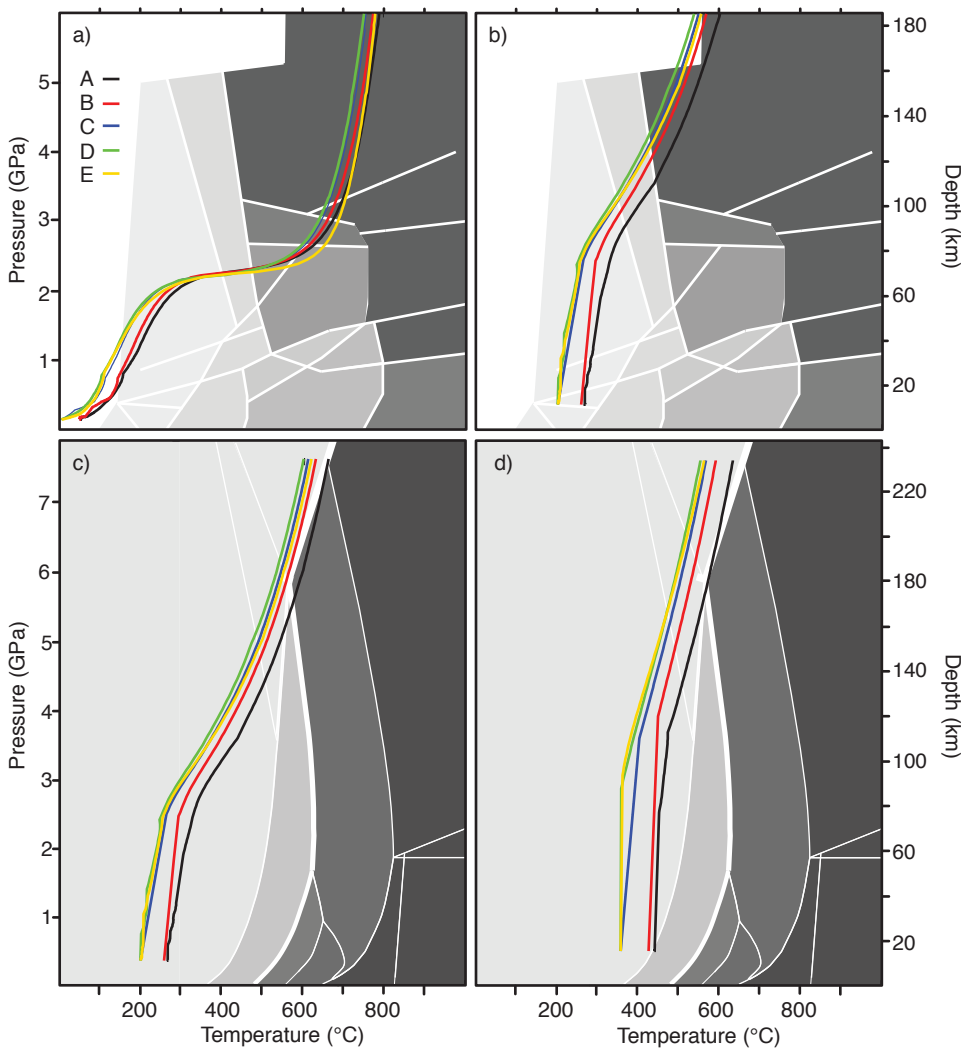

Figure 4.6 *PT* paths for all profiles for models with HC. **a**: top of the oceanic crust; **b**: bottom of oceanic crust (Moho); **c**: top of ocean lithosphere; **d**: surface 12 km below top of the oceanic crust. *PT* paths are superimposed on phase diagrams for MORB (top row) and harzburgite (bottom row). Gray shading is the same as in Figure 4.5.

2003] to predict the depth of dehydration of oceanic mantle.

For profiles B and C, the reference models predict that the uppermost oceanic mantle (between 7 km and 12 km depth) retains a substantial amount of water (40%) to depths of 170-180 km. At this depth, there is a transition to chlorite harzburgite near the top of the oceanic mantle. When HC is included, the oceanic lithosphere is cooled slightly, especially for profile C with EHC. As a result, the uppermost mantle lithosphere stays within the serpentine stability region to depths greater than 180 km. Due to the larger cooling effect of EHC (Figure 4.4), ventilated slabs might offer the better chance of transporting large quantities of water to the deeper mantle.

4.4.3 Along-Strike Variations

The previous discussion focused on profiles B and C. We have also developed thermal models for the remaining three profiles on Figure 4.1. We use these to predict the depth of dehydration of oceanic crust and mantle. In all cases, models with HC give PT paths for the top of the oceanic crust in which the transition to amphibole eclogite occurs at approximately 65 km (Figure 4.6a), regardless of HC mode. The crust transforms to diamond eclogite at depths between 110 km in profile A and 125 km in profile E, with the profile D having the deepest transformation at 135 km (Figure 4.6b). Along the strike, the most significant difference in the depth of complete eclogitization occurs between profiles A and C (15-20 km), where the age of the Cocos plate along the MAT is 20-24 Myr. Between Profiles D and E, the depth of eclogitization varies by less than 10 km, coinciding with an age variation of only 1 Myr. This suggests that plate age has a larger effect on dehydration and metamorphism than HC.

For the oceanic mantle, the region below the Moho may undergo dehydration

at a depth of 165-170 km on profile A (Figure 4.6c). For deeper parts of the slab, the Cocos oceanic mantle appears to be cool enough to transport water to large depths, especially for the profiles in the northwest part of the subduction zone (EPR lithosphere) (Figure 4.6d).

4.5 Discussion

Geophysical and geochemical observations of the Costa Rica-Nicaragua subduction zone show that there is a northwestward increase in mantle wedge hydration (Figure 4.2) [Rychert et al., 2008; Syracuse et al., 2008; Hoernle et al., 2008; Dinc et al., 2011; Ivandic et al., 2010; Harris et al., 2010a; Carr et al., 2014]. The numerical models in this study investigate whether this spatial variation is related to an along-strike change in the thermal structure of the subducting oceanic plate. Compared to previous models in the region [Peacock et al., 2005; Harris et al., 2010b], our models incorporate HC along the subducting crust and a non-Newtonian rheology for the mantle wedge, as these two factors can have a significant impact on the thermal structure [van Keken et al., 2002; Currie et al., 2004; Kummer and Spinelli, 2008; Kummer and Spinelli, 2009; Rotman and Spinelli, 2013].

Figures 4.4 and 4.5 show that the along-strike thermal structure of the Cocos plate in models with HC changes with respect to models without fluid flow. The difference can be up to 30°C in the profiles located in the CNS section of the Cocos plate (A and B), and 60°C in profiles located in the EPR section (profiles C through E). These changes persist to depths > 150 km (Figure 4.4d). The temperature differences between models with and without HC are mostly the result of the initial oceanic geotherm employed for each profile (Figure 4.3b). For the EPR side, the boundary condition results in lower temperatures for the Cocos plate at the trench when com-

pared to the CNS side. The change is due to the slow rate of conductive heating relative to slab advection. Additional model tests show that a lower convergence rate results in a reduced effect of HC at large depths, as the hydrothermally cooled slab is conductively heated as it descends.

However, the thermal differences induced by the two regimes of HC are not large enough to significantly change the depth of the different dehydration reactions relative to models with no HC (Figure 4.5). Transformation to amphibole eclogite, zoisite eclogite, and diamond eclogite releases most of the water stored in the oceanic crust. In the models with HC, for the top of the slab, no changes in the depth of transformation to amphibole eclogite are observed between the profiles. The transformation occurs at a depth of 65-70 km, consistent with the intersection between the flowing mantle wedge and the slab, indicating that mantle wedge flow controls the temperature at the slab interface. The deeper crust fully transforms to eclogite at depths of 110-135 km, at which point the crust is completely dry. When HC is included in the models, the depth of eclogitization increases by only $\sim$15 km for profiles C through E. For profiles A and B, the change is less than 10 km between models with and without HC. HC does not strongly affect the depth of eclogitization and does not appear to fully explain the differences in mantle hydration between Nicaragua and Costa Rica suggested by geochemical [Carr et al., 2003; Patino et al., 2000; Carr et al., 2014] and seismic [Syracuse et al., 2008; Rychert et al., 2008; Dinc et al., 2011] studies. Most of the predicted dehydration, however, does take place below the mantle wedge.

Figure 4.7 shows the modeled thermal structure, the seismicity, and the predicted depth of complete eclogitization of the oceanic crust for each profile for the reference models and models with HC. Along the strike of the MAT, the maximum depth of slab seismicity is approximately 180-200 km below central Nicaragua and Nicoya, 150-160 km in central Costa Rica, and $<$100 km in south Costa Rica [Protti et al.,

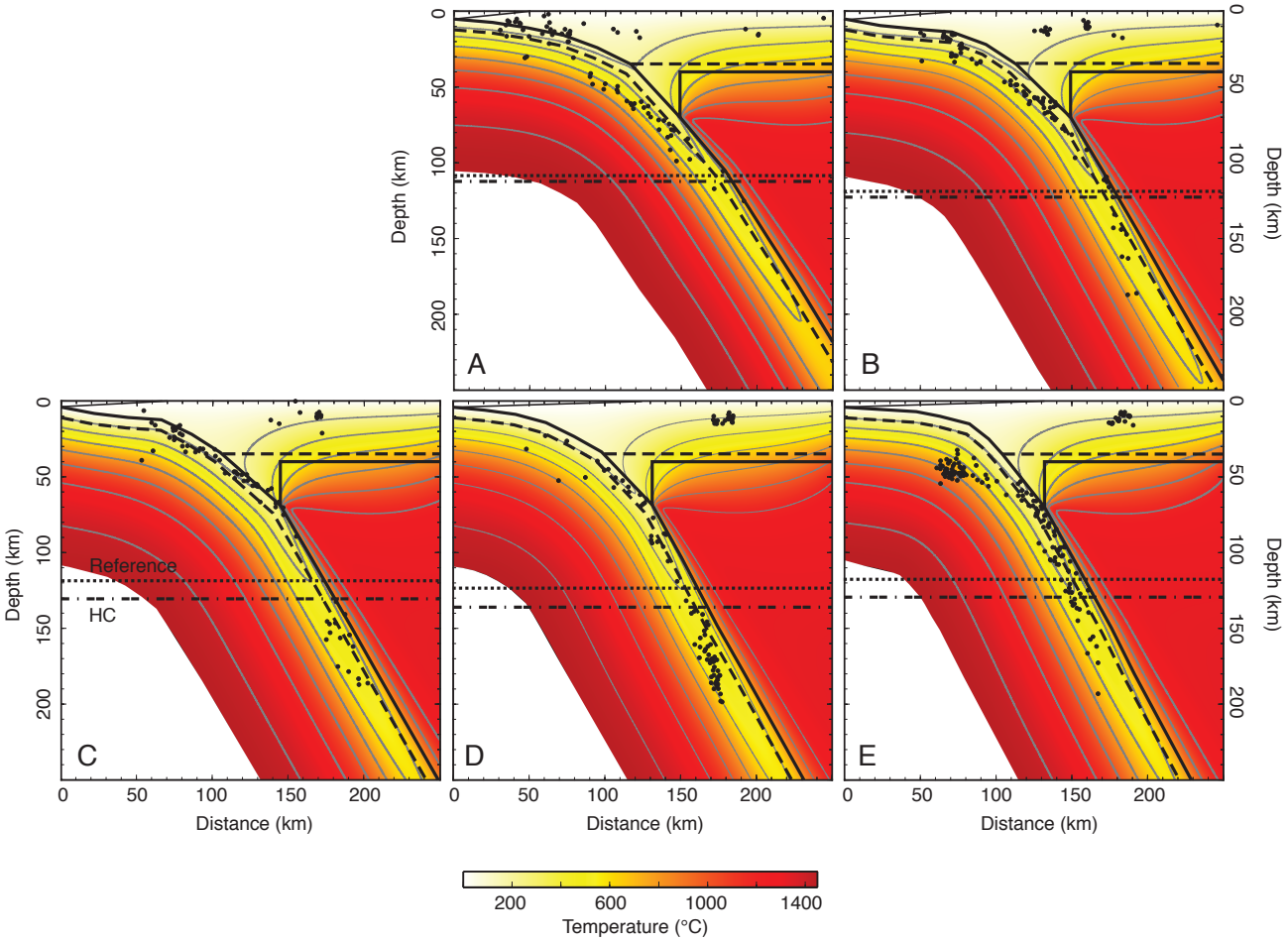

Figure 4.7 Thermal models with HC for profiles A through E. Gray lines are isotherms with a 200°C spacing. Black dots are earthquakes recorded by the TUCAN (`http://www.ldeo.columbia.edu/~abers/TUCAN.html`) and CRSEIZE (`http://es.ucsc.edu/~hdeshon/crseize_homepage.html`) networks. Each profile contains earthquakes within a 10 km region to the south and north of each profile line. Depth of full crustal eclogitization for the reference models (dotted line) and for models with HC (dashed-dotted line) is shown.

1995; MacKenzie et al., 2010]. Earthquakes at these depths are thought to be the result of slab dehydration, which releases water and can reactivate old faults by dehydration embrittlement [Kirby et al., 1996]. For the reference models, seismicity within the crust for profiles A, B, and C is largely absent below the modeled depth of eclogitization, with a few earthquakes occurring possibly at greater depths within the crust in profiles B and C. For Profiles D and E, crustal earthquakes appear to occur deeper than the modeled depth of eclogitization. The inclusion of HC in the models offers a better fit to the observed seismicity. Along profiles A and B, models with HC exhibit only minor differences with respect to the reference models. For profiles C, D and E, crustal earthquakes are restricted to depths shallower than the predicted depth of eclogitization. A few earthquakes are observed at greater depths; these may reflect kinetic hindrance in the basalt-to-eclogite phase change.

For the oceanic lithosphere, the addition of HC facilitates water transport to the deep mantle. Transport of water trapped in serpentinized harzburgite increases in the northwestward direction, consistent with a cooler slab (Figures 4.6c and 4.6d). For central Costa Rica and southern Nicoya (profiles A and B), there is a clear shift of the PT paths towards the serpentinite stability region; for northern Nicoya, north Costa Rica and Nicaragua (profiles D, C and E), PT paths for the oceanic lithosphere do not show significant differences. As the age of the slab does not change significantly for these segments, we conclude the age of the slab is more important than HC in controlling the depth at which water can be transported to large depths.

The effect of HC on subducton zone thermal structure has also been studied for the Cascadia and Nankai margins. For Cascadia, HC shifts the location of the transition to eclogite downdip by as much as 15 km [Cozzens and Spinelli, 2012]; for Nankai, the change is 10-15 km [Spinelli and Wang, 2009]. For both of these subduction zones, the dominant hydrothermal regime is IHC. In the case of Costa Rica-Nicaragua, the

models in this study show that IHC does not significantly affect the depth of transition to eclogite. The reason for this was discussed by Rotman and Spinelli [2013]. IHC tends to homogenize temperatures laterally along the aquifer (Figure 4.4), and therefore the effect of IHC will be largest for subduction zones that have strong lateral temperature gradients within the aquifer without any fluid circulation. The lateral gradients are largest for subduction zones with young, steeply dipping, and slowly convergent slabs [Rotman and Spinelli, 2013]. Although the Cocos plate is relatively young in its CNS section (20-22 Myr), both Cascadia and Nankai are younger, with ages of 5-9 Myr and 15-20 Myr, respectively. The convergence rate in the CNS section is also greater ($\sim$9 cm/yr) than for Cascadia and Nankai ($\sim$5 cm/yr). Therefore, the overall effect of IHC on slab temperatures and metamorphism is relatively small for Costa Rica-Nicaragua.

For the EPR side, EHC shifts the transition to eclogite downdip by $\sim$15 km. Generic models predict that EHC may have the largest impact in subduction zones such Mexico and Solomon Islands, with an hydrothermal cooling of $\sim$125-180°C [Rotman and Spinelli, 2013]. Recent models for the Mexican subduction zone have shown that HC can lower slab temperatures by as much as 180°C [Perry et al., 2016]. This change is significantly larger than for the EPR side of the Cocos plate, where hydrothermal cooling is $\sim$60°C . We thus confirm previous studies that predict HC will likely have a larger effect on young ($<$ 15 Myr), ventilated subduction zones with a small convergence rate [Rotman and Spinelli, 2013].

Our 2D models predict only minor changes in the deep slab thermal structure due to HC along the Costa Rica-Nicaragua subduction zone, emphasizing the large role mantle wedge flow plays in controlling the thermal structure at these depths. Our study has focused only on the along-strike variations in oceanic plate structure. Possible three-dimensional (3D) variations in mantle wedge flow structure may also

lead to along-strike variations in slab and wedge temperatures. Along the MAT, rapid along-strike mantle wedge flow has been inferred based on arc geochemistry [Herrstrom et al., 1995; Johnston and Thorkelson, 1997; Abratis and Worner, 2001] and shear-wave splitting studies [Hoernle et al., 2008]. The flow has been estimated to be 6-19 cm/yr in the northwest direction. Recent studies have shown that even a relatively small (∼4 cm/yr) along-strike mantle wedge flow below Costa Rica-Nicaragua changes mantle wedge temperatures by as much as 50°C [Rosas et al., 2016]. Thus, it is reasonable to expect a larger change in wedge temperatures if a 6-19 cm/yr along-strike flow magnitude is incorporated into future models. This change in the temperature of the mantle wedge affect the temperatures of the slab and possibly change the depth of dehydration.

To summarize, our results suggests that the temperature difference induced by HC on the subducting Cocos plate does not significantly affect the predicted depth of slab dehydration. Hence, the observed along-strike changes in arc geochemistry [Patino et al., 2000; Carr et al., 2003, 2014], seismic attenuation [Rychert et al., 2008] and seismic velocities [Syracuse et al., 2008; Dinc et al., 2011] (Figure 4.2), are not related to along-strike changes in the thermal structure of the Cocos plate (the thermal hypothesis, as discussed in Section 4.1). For the entire region, our models predict that the subducting oceanic crust dehydrates at depths of 70 to 130 km. Thus, the overlying mantle wedge is predicted to be hydrated at every location along the strike of the trench. Although we do not model water transport from the slab to the mantle, this result suggests that northwestward increase in wedge hydration for the Costa Rica-Nicaragua subduction zone may be the result of an increase in the amount of water stored in Cocos plate offshore Nicaragua, where outer rise bending and faulting allow ocean water to penetrate and hydrate the crust and the mantle [Abers et al., 2003; Ivandic et al., 2010; Van Avendonk et al., 2011]. For the serpentinized mantle,

the models predict that dehydration starts at depths greater than 160 km for all parts of the region. The slab is predicted to retain most of its water to depths larger than 180 km (Figure 64.6.

4.6 Conclusions

In this study, we presented 2D thermal models of the subduction zone below Costa Rica and Nicaragua. The models incorporate hydrothermal circulation (HC) and non-Newtonian wedge flow. These factors have competing effects on the deep thermal structure of the slab; HC cools it, while wedge flow heats it. An accurate assessment of the slab thermal structure therefore needs to consider both of these effects.

Offshore heat flow observations indicate that HC occurs in the upper oceanic crust [Harris et al., 2010b]. Along-strike variations in heat flow suggest that two distinct types of HC are present in Central America: inefficient (IHC) and efficient (EHC). Their respective effects on subduction temperatures are shown in Figures 4.4 and 4.5. For the Cocos-Nazca Spreading Centre (CNS) lithosphere, IHC cools the slab interface by 25-30°C to depths of 50 km with respect to models with no HC. For the East-Pacific Rise (EPR) lithosphere, EHC cools the slab by as much as 60°C along the subduction interface to a depth of 70 km. For larger depths, a cooling of 40°C occurs in the upper 30 km of the slab. Overall, EHC has a greater cooling effect on the Cocos plate than IHC.

Based on our models, we conclude the following points:

1. HC does affect the thermal structure at depths >20 km with respect to models without fluid flow (Figure 4.4), but the magnitude of the temperature difference does not significantly change the predicted depth of the metamorphic phase change to eclogite (Figure 4.5), the major water-release transformation occur-

ring in the oceanic crust. For the top of the crust, the transition occurs where the slab encounters the mantle wedge, indicating that the effect of mantle flow is more important in regulating the temperature. For the bottom of the crust, the depth of complete eclogitization shifts ∼15 km downdip with respect to models with no fluid flow.

2. For the intraslab crustal seismicity, models with and without HC predict similar eclogitization depths for the CNS side and both are in good agreement with the seismicity. For the EPR side, models with HC fit the seismicity slightly better than models with no fluid flow.

3. HC reduces slab temperatures throughout the slab in the EPR side. While this aids in the large-scale water transport from the oceanic lithosphere to the mantle, the closeness of the *PT* paths for profiles C, D and E in Figure 4.6 indicates that the age of the slab is the most important parameter in controlling water transport to the mantle for this subduction zone.

4. Our models show that the depth of slab dehydration increases to the northwest along the subduction zone, but the variation is fairly small, despite the greater degree of hydrothermal cooling in the northwest. Therefore, the observed along-margin increase in mantle wedge hydration is likely related to a greater amount of water within the oceanic plate offshore Nicaragua (slab hydration hypothesis, as discussed in Section 4.1), as suggested by other studies [Abers et al., 2003; Van Avendonk et al., 2011; Ivandic et al., 2010]. Greater slab hydration in Nicaragua is probably due to enhanced outer rise fracturing in this regions [Ranero et al., 2003; Van Avendonk et al., 2011].

Acknowledgments

We thank Christodoulos Kyriakopoulos for providing the updated geometry of the Cocos plate prior to publication, and Geoffrey Abers and Ellen Syracuse for providing earthquake locations in Costa Rica-Nicaragua. We also thank Harm Van Avendonk for helpful and thoughtful reviews and Mark Jellinek for his editorial handling of the manuscript. Research was funded by the Natural Sciences and Engineering Research Council of Canada (NSERC) and the National Council for Science and Technology of Mexico (CONACYT).

Chapter 5

Three-Dimensional Thermal Model of the Costa Rica-Nicaragua Subduction Zone

This chapter has been published.
Rosas, J., Currie, C., and He, J. (2015). *Three-dimensional thermal model of the Costa Rica-Nicaragua subduction zone.* Pure and Applied Geophysics, 1-23, DOI: 10.1007/s00024-015-1197-4

Abstract

The thermal structure of a subduction zone controls many key processes, including subducting plate metamorphism and dehydration, the megathrust earthquake seismogenic zone and volcanic arc magmatism. Here, we present the first three-dimensional (3D), steady-state kinematic-dynamic thermal model for the Costa Rica-Nicaragua subduction zone. The model consists of the subducting Cocos plate, the overriding Caribbean Plate, and a viscous mantle wedge in which flow is driven by interactions with the downgoing slab. The Cocos plate geometry includes along-strike variations in slab dip, which induce along-strike flow in the mantle wedge. Along-strike flow

occurs primarily below Costa Rica, with a maximum magnitude of 4 cm/yr (∼40 % of the convergence rate) for a mantle with a dislocation creep rheology; an isoviscous mantle has lower velocities. Along-margin flow causes temperatures variations of up to 80°C in the subducting slab and mantle wedge at the volcanic arc and backarc. The 3D effects do not strongly alter the shallow (<35 km) thermal structure of the subduction zone. The models predict that the megathrust seismogenic zone width decreases from ∼100 km below Costa Rica to just a few kilometers below Nicaragua; the narrow width in the north is due to hydrothermal cooling of the oceanic plate. These results are in good agreement with previous 2D models and with the rupture area of recent earthquakes. In the models, along-strike mantle flow is induced only by variations in slab dip, with flow directed toward the south where the dip angle is smallest. In contrast, geochemical and seismic observations suggest a northward flow of 6-19 cm/yr. We do not observe this in our models, suggesting that northward flow may be driven by additional factors, such as slab rollback or proximity to a slab edge (slab window). Such high velocities may significantly affect the thermal structure, especially at the southern end of the subduction zone. In this area, 3D models that include slab rollback and a slab edge are needed to investigate the mantle structure and dynamics.

5.1 Introduction

A subduction zone delineates the convergent boundary between tectonic plates, where oceanic lithosphere descends below a less dense oceanic or continental plate [Stern, 2002]. As an oceanic plate moves away from a mid-ocean ridge, it thickens and its density increases, eventually becoming negatively buoyant and sinking into the deep Earth [Cloos, 1993]. It is generally accepted that this gravitational instability is the primary force driving the motion of the tectonic plates [Forsyth and Uyeda, 1975], and therefore it is not surprising that subduction zones are a topic of intense study. Among subduction zones, the Costa Rica-Nicaragua section of the Middle America Trench (MAT) has received particular attention in recent years. Figure 5.1 shows

the configuration of the MAT in Central America, with the Cocos plate subducting beneath the Caribbean Plate. Subduction in this region is associated with the formation of the Central America Volcanic Arc [Carr et al., 2003]. It is also responsible for earthquakes that occur within both the Cocos plate and the Caribbean plate, as well as megathrust earthquakes that occur on the inclined subduction interface. The most recent megathrust earthquake was the magnitude Mw 7.6 event that occurred on September 5th, 2012 below the Nicoya Peninsula of Costa Rica [Protti et al., 2014].

Despite the predominantly trench-perpendicular direction of plate convergence, there are numerous observations that suggest significant along-strike changes in the characteristics of this subduction zone. These include variations in the width of the megathrust seismogenic zone [Newman et al., 2002; DeShon et al., 2006; Schwartz and Deshon, 2007; Audet and Schwartz, 2013], variable amounts of hydrothermal circulation in the Cocos plate crust [Fisher et al., 2003b; Hutnak et al., 2008; Harris et al., 2010a], and different levels of hydration for the descending slab and overlying mantle [Abers et al., 2003; Syracuse et al., 2008; Rychert et al., 2008; Van Avendonk et al., 2011; Dinc et al., 2011]. The geochemistry of arc magmas also varies along strike, with geochemical gradients in radiogenic isotope ratios, such as B/La and Ba/La, that are associated with fluid loss from the slab [Patino et al., 2000; Carr et al., 2003]. In addition, $^{208}Pb/^{204}Pb$ and $^{143}Nd/^{144}Nd$ ratios suggest that the magma source includes a component related to ocean-island basalt (OIB) from the Galapagos Hot Spot track [Herrstrom et al., 1995; Johnston and Thorkelson, 1997; Abratis and Worner, 2001; Hoernle et al., 2008]. These data, together with seismic anisotropy observations, have been used to argue for an along-strike flow of 6.3-19 cm/yr within the mantle above the subducting Cocos plate in Costa Rica and Nicaragua [Hoernle et al., 2008]; flow is inferred to go from southeast to northwest (Figure 5.1).

Many subduction zone processes, including the earthquake distribution, slab de-

hydration and arc volcanism, depend strongly on the thermal structure. A common approach to study the temperature distribution is to create two-dimensional (2D) steady-state numerical models of the subduction system (oceanic plate, overriding plate, and viscous mantle wedge) in which dynamically calculated mantle wedge flow is driven by a kinematically prescribed subducting plate (e.g., Peacock [1996]).

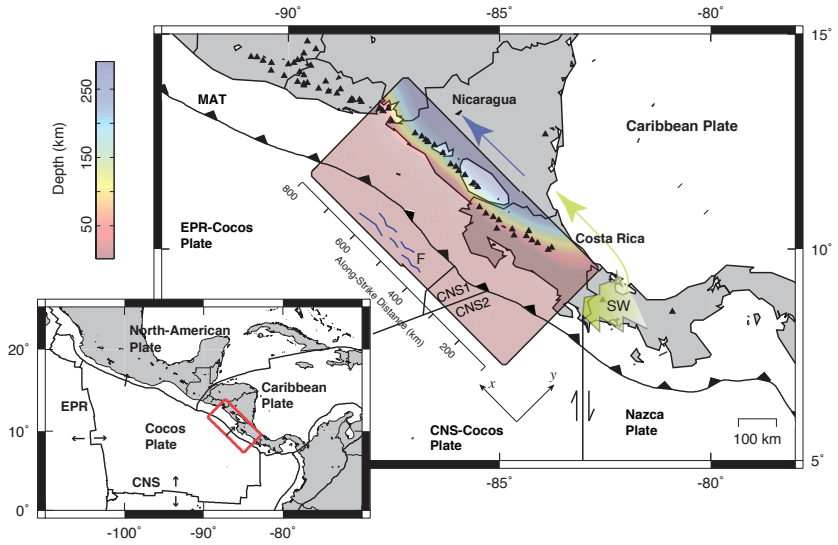

Figure 5.1 Map of the study area at the Costa Rica-Nicaragua subduction zone. Colors indicate the depth to the top of the subducted Cocos plate, as obtained from Kyriakopoulos et al. [2015]. Scale denotes along-strike distance ($x-$axis). 3D model extends from $x = 200$ km to $x = 700$ km, and from the trench landward until the slab reaches a depth of 300 km along the $y-$axis. Dashed black lines are the location of profiles A through D. Volcanoes are shown with black triangles. The Middle America Trench (MAT) runs approximately parallel to volcanic arc. Location of the Nicoya peninsula is shown. Plate boundaries between lithosphere generated at the East Pacific Rise (EPR) and lithosphere generated at the Cocos-Nazca Spreading Centre (CNS) are also shown [Barckhausen et al., 2001]. Location of slab window (SW) is shown in light green[Johnston and Thorkelson, 1997], with light green arrow showing possible direction for oceanic-island basalt (OIB). B/La and Ba/ La signal (blue arrow) increase in the northwest direction, indicating greater hydration in the mantle below Nicaragua. Inset shows study area (enclosed by red box) on a large-scale tectonic map. Black arrows denotes plate motion. Plate boundaries are from [Bird, 2003].

Three key factors control the thermal structure of a subduction zone: the temperature of the incoming oceanic plate (slab), the plate convergence rate, and the flow pattern of the overlying mantle wedge. The temperature of the slab is primarily a function of its age, with heat being transferred by conduction. In the mantle wedge, however, heat is transferred mainly by the motion of the viscous mantle. In the context of fluid dynamics, the downward motion of the descending oceanic plate drags the overlying mantle by viscous coupling and sets up a forced-convection flow pattern, i.e., corner flow [Batchelor, 2000].

Several 2D thermal models have been developed for the Costa Rica-Nicaragua subduction zone. The objective of these models varies, and they can be roughly classified into two categories:

1. Models to study the relationship between hydrothermal circulation and shallow slab temperatures.

2. Models to study the role of viscous wedge flow in deep metamorphic and dehydration reactions within the slab.

The first category is reasonably well studied. These studies show that significant hydrothermal circulation must occur in the shallow (< 1 km) oceanic crust, to explain the observed surface heat flow along the MAT in Central America [Fisher et al., 2003b; Hutnak et al., 2008; Harris et al., 2010a]. Hydrothermal circulation cools the oceanic crust and provides a relatively good match between crustal temperatures and distribution of seismicity [Harris and Wang, 2002; Kummer and Spinelli, 2008; Cozzens and Spinelli, 2012; Rotman and Spinelli, 2013]. For the second category, Peacock et al. [2005] demonstrated that a non-Newtonian mantle rheology is needed to sustain the high temperatures required for mantle melting and arc volcanism. This also results in an oceanic crust that is fully dehydrated and transformed to eclogite at

depths of 70-100 km. However, they do not find significant variations in the thermal or flow structure along the strike of the subduction zone, which would be needed to fit the along-margin variations in arc geochemistry.

There are multiple factors that may explain the discrepancy between 2D models and the observed geochemistry. These include possible along-strike changes in the thermal state of the incoming oceanic plate or changes in the amount of water released into the mantle [Abers et al., 2003; Syracuse et al., 2008; Rychert et al., 2008; Van Avendonk et al., 2011; Dinc et al., 2011]. An important one, however, is the intrinsic two-dimensionality of the corner flow model. It is known that geometrical factors such as along-strike variations in slab dip or trench curvature can induce along-strike mantle flow [Kneller and van Keken, 2008; Bengtson and van Keken, 2012; Wada et al., 2015]. Such characteristics are present in Central America (Figure 5.1). In this region, the Cocos plate changes its dip from approximately 70° in Nicaragua to 45° in Central Costa Rica at depths greater than 70 km. The change occurs over an along-strike distance of 200 km.

In this study, we present the first three-dimensional (3D) model of the thermal structure of the Costa Rica-Nicaragua subduction zone. Our approach is similar to previous 2D models, as we incorporate a subducting slab that drives mantle wedge flow by viscous coupling. However, we consider a three-dimensional slab with a non-Newtonian rheology for the mantle wedge, using the most up-to-date geometry for the Cocos plate. This is expected to induce significant lateral flow in the mantle wedge, therefore changing the overall temperature distribution relative to 2D models. Our objectives are to quantify these differences and provide a more detailed description of the thermal structure of this subduction zone.

5.2 Model Set Up

The numerical models use a kinematic-dynamic approach to model the steady-state thermal structure of the subduction zone [van Keken et al., 2002, 2008; Currie et al., 2004]. The subducting oceanic plate and overriding continental plate have a fixed geometry and convergence rate. The mantle wedge has a viscous rheology and flows in response to the imposed subduction dynamics. The advantage of this approach over a completely dynamic subduction zone is that it allows for a much higher resolution of the thermal structure, especially in the mantle wedge corner region [Billen, 2008]. The disadvantage is that we neglect any dynamic factors, such as slab rollback or roll forward, which might induce 3D mantle flow as well.

To investigate 3D mantle wedge flow and the resulting temperature distribution of the Costa Rica-Nicaragua subduction zone, we use a three-dimensional finite-element mesh of the Costa Rica-Nicaragua subduction zone. The mantle wedge flow and thermal structure are computed using the equations of mass, momentum and energy. In that order, the equations are:

$$\nabla \cdot \mathbf{v} = 0 \ , \tag{5.1}$$

$$\nabla P - \nabla \cdot \boldsymbol{\sigma} = 0 \ , \tag{5.2}$$

$$\nabla \cdot (k \nabla T) - \rho c_p (\mathbf{v} \cdot \nabla T) + A = 0 \ , \tag{5.3}$$

where $\mathbf{v}$ is the velocity, P is the dynamic pressure, $\boldsymbol{\sigma}$ is the deviatoric stress tensor, T is the temperature, k is the thermal conductivity, A is the rate of radiogenic heat production, ρ is the density, and c_p is the specific heat. In the calculations, the mantle is assumed to be a Boussinesq fluid with infinite Prandtl number, and flow in the mantle wedge is driven only by the subducting plate. The models use the finite-element code PGCtherm3D. This code is the three-dimensional version of

PGCtherm2D, which has been previously benchmarked [van Keken et al., 2008] and used in other studies of different subduction zones (e.g., Currie et al. [2004]; Wada et al. [2008]; Wada and Wang [2009]; Wang et al. [2015]). PGCtherm3D was also used in a recent 3D modeling study of the northeast Japan subduction zone [Wada et al., 2015].

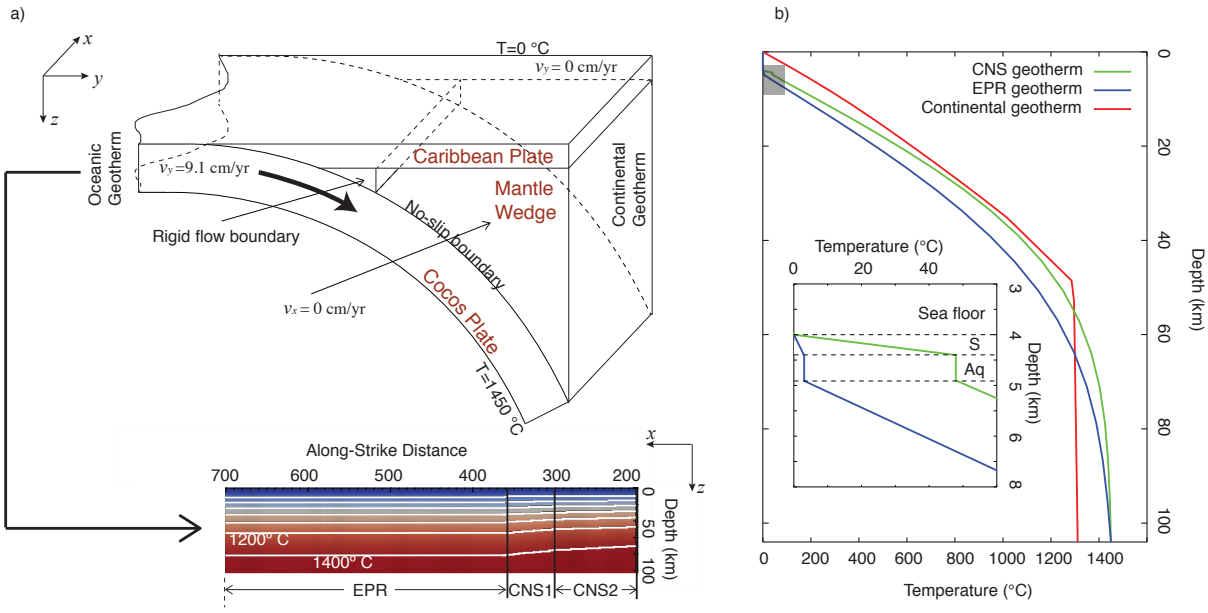

Figure 5.2 **a)** Schematic diagram of the 3D model and boundary conditions. The 2D temperature boundary condition for the oceanic boundary is shown, with isotherms shown every 200°C . Location of the boundary between CNS and EPR lithosphere is shown. **b)** Typical geotherms for CNS (green) and EPR (blue) oceanic lithosphere. Inset shows the oceanic geotherms at shallow depths, with sediments (S) and aquifer (Aq) having thicknesses of 400 m and 500 m, respectively.

The three main units in the model are the overriding Caribbean plate, the subducting Cocos plate and the viscous mantle wedge; smaller units such as the sediment layer of the oceanic plate or the upper and lower continental crust are considered as part of these main units. The rigid overriding plate consists of a 35 km-thick crust and

the top 5 km of upper mantle. This crustal thickness is consistent with the average Moho depth for Central America [MacKenzie et al., 2008; Manea et al., 2013]. The geometry of the subducting plate is from Kyriakopoulos et al. [2015]. The subducting plate has a total thickness of 100 km, and it is assumed that this includes the oceanic sediments, crust and mantle lithosphere, as well as sublithospheric mantle that is entrained with the subducting lithosphere. The model domain extends from south Costa Rica to Nicaragua. We selected this region due to the strong along-margin variations in slab dip at depths 70 km, which changes from approximately 70° in Nicaragua to 45° in central Costa Rica. Further south, the Cocos plate is difficult to observe because of the lack of Wadati-Benioff seismicity and arc volcanism [Protti et al., 1995]. The area may correspond to a slab window formed by subduction of the Cocos-Nazca spreading centre from late Miocene to late Pliocene [Johnston and Thorkelson, 1997; Abratis and Worner, 2001], as shown in Figure 5.1. The $x-$axis in our models is approximately aligned with the trench, the $y-$axis is in the landward direction, and the $z-$axis is the depth. The origin of the model grid is at -84°W, 7°N, and therefore, the model domain extends from x=200 to x=700 km. The trench corresponds to the seaward boundary of the model. The location of the backarc (landward) boundary is taken to be where the top of the oceanic plate is at a depth of 300 km; this keeps our modeling domain in the upper mantle. As the slab dip varies along the strike of the subduction zone, the distance between the trench and backarc boundary is variable, ranging between 200 and 300 km from the wedge corner. Tests show that the location of the backarc boundary has only a minor effect on temperatures in the mantle wedge, as long as the distance from the wedge corner to the boundary does not change by more than 200 km along the strike.

The thermal parameters for each model material follow those used by Harris et al. [2010b] and are given in Table 5.1. The overriding plate has a velocity of 0 cm/yr,

Table 5.1 Material properties and model parameters.

Subdomain	A (μW/m^3)	k (W/m K)	ρ (g/cm^3)	c_p (J/Kg K)
Continental Crust	0.2	2.9	3.3	1250
Mantle Wedge	0.02	3.1	3.3	1250
Oceanic Slab	0.2	2.9	3.3	1250

and the subducting plate has an assigned convergence velocity of 9.1 cm/yr, in agreement with the average velocity in our modeling area [DeMets, 2001]. For the mantle wedge, we present models with either an isoviscous rheology (viscosity of 10^{21} Pa s) or a power-law (non-Newtonian) rheology. The latter is based on the flow law for dislocation creep of wet olivine [Karato and Wu, 1993]:

$$\eta = A\dot{\epsilon}^{\frac{1-n}{n}} \exp\Big(\frac{E}{nRT}\Big) \ , \tag{5.4}$$

where A=28,968.6 Pa s$^{1/n}$ is the pre-exponential factor, $\dot{\epsilon}$ is the strain rate, E=430 kJ/mol is the activation energy, R is the universal gas constant, T is the temperature, and n=3 is the power-law exponent.

The boundary conditions for the model are shown in Figure 5.2. The top of the model is rigid with a tem- perature of 0°C , and the bottom of the model corresponds to the base of the oceanic plate, which has a velocity of 9.1 cm/yr and temperature of 1450°C . Free-slip and insulating boundary condi- tions are used on the side boundaries at x=200 km and x=700km, such that v_x=0 and there is no heat flow through these boundaries. The effect of the boundary conditions on the modeling results is discussed in the Appendix. At the oceanic boundary, a fixed velocity of 9.1 cm/yr is assigned. The temperatures along this boundary are based on the GDH1 oceanic plate cooling model [Stein and Stein, 1992], using the age of the plate at each point along

the trench. The complete oceanic boundary temperature can be seen in Figure 5.2a. Three age domains are included. Lithosphere generated at the Cocos-Nazca Spreading Centre (CNS) is divided into two sections: CNS1 and CNS2 [von Huene et al., 2000; Barckhausen et al., 2001]. These segments have ages of 17.5-20, and 20-24 Myr, respectively. An age of 24 Myr is used for lithosphere generated at the East Pacific Rise (EPR). The boundary between EPR and CNS2 lithosphere is found offshore the Nicoya peninsula (Figure 5.1); in our coordinate system is located at approximately x=360 km. At each point along the trench, the 1D oceanic geotherm incorporates the effects of sedimentation and sediment permeability, following Langseth and Silver [1996], Harris and Wang [2002] and Harris et al. [2010b]. In this area, temperatures at the uppermost oceanic crust (aquifer) may be affected by hydrothermal circulation. Harris et al. [2010b] showed that the offshore heat flow data are consistent with ventilated hydrothermal circulation for the EPR segment and insulated hydrothermal circulation for the CNS segment. In their models, hydrothermal circulation is allowed to continue to greater depths after subduction by introducing conductivity proxies in the crustal aquifer [Davis et al., 1997]. Our geotherms use the thermal structure proposed by Harris et al. [2010b] for the oceanic boundary but do not include conductivity proxies for the aquifer. Our approach is thus similar to that employed by Langseth and Silver [1996] and Harris and Wang [2002]. Figure 5.2b shows typical geotherms for EPR and CNS sections.

At the backarc boundary, stress-free conditions are used. No heat flow is assumed through this boundary, and the inflow-outflow transition is determined dynamically. The backarc geotherm is given by a steady-state equilibrium geotherm for a continental plate with a surface heat flux of 90mW/m^2, in agreement with observed backarc temperatures [Currie and Hyndman, 2006]. This geotherm intersects a mantle adiabatic gradient with a potential temperature of 1295°C at an approximate depth of

50 km (Figure 5.2b). The geotherm temperatures are assigned to the rigid overriding plate and the region of the mantle wedge with flow into the model domain.

Flow within the mantle wedge is driven by the subducting oceanic plate. Therefore, we employ a no-slip boundary condition between the downgoing plate and the lower boundary of the mantle wedge. The upper wedge boundary has a fixed velocity of 0 cm/yr. For computational efficiency, a rigid vertical flow boundary is placed in the wedge. This is also consistent with serpentinization of the forearc mantle, which is proposed to decouple the subducting slab from the mantle [Manea et al., 2005; Manea and Manea, 2008; Wada et al., 2008]. The boundary is located at the point at which the slab reaches a depth of 70 km, and it extends from the surface of the slab to the base of the upper plate. This location is consistent with observations that show that stagnation of the wedge corner is required to fit observations of a rapid landward increase in surface heat flow, from low values in the forearc to high values near the volcanic arc and into the backarc [Wada et al., 2008; Wada and Wang, 2009]. In the models, there are high gradients in pressure and temperature near the mantle wedge corner and along the surface of the slab, especially when a non-linear rheology is used (Equation 5.4). Thus, our models use a variable element size in the direction of subduction, where elements are as small as a few meters in the mantle wedge tip and as large as ∼10 km in the upper crust and deep slab. Along the strike of the subduction zone, the element width is 2 km. These sizes are based on benchmark tests [van Keken et al., 2008; Bengtson and van Keken, 2012]. In total, we employ 1,138,800 cubic elements that give a total of 9,262,617 grid nodes.

To assess the effect of 3D processes on the thermal structure, we also present 2D models at several locations along the subduction zone (Figure 5.1). These 2D models are later compared to cross-sections extracted from the 3D model at the location of each profile. From south to north, the profiles are: profile A and B, located in

south and central Costa Rica, respectively; profile C, located near the Costa Rica-Nicaragua border; and profile D, located in central Nicaragua. Profile A is located in a region in which there is a change of almost 25° in the dip of the slab over an along-strike distance of 200 km. For the other profiles, there are no significant along-margin changes in the geometry of the plate. These 2D models also use PGCtherm3D, but are only 100 m wide, with no variations in slab geometry (i.e., they have a 2D structure). The models have the same material prop- erties and boundary conditions as those in the full 3D model. Given that convergence of the Cocos plate in the MAT along Costa Rica-Nicaragua is mostly trench-perpendicular (∼10deg obliquity) [DeMets, 2001] and that the trench is almost straight in our study region, our 2D profiles are taken parallel to the convergence direction.

5.3 Results

Flow in the mantle wedge is a primary control factor on the thermal distribution of a subduction zone, especially beneath the volcanic arc. The nature of flow depends on the rheology of the mantle wedge [van Keken et al., 2002]. Shear-wave splitting studies demonstrate that the dislocation creep is the dominant deformation mechanism in the mantle wedge [Kneller and van Keken, 2008; Long and Silver, 2008; Hoernle et al., 2008; Soto et al., 2009]. However, we also present isoviscous models to gain a basic understanding of the factors that control the direction and magnitude of mantle wedge flow.

It is illustrative to start with a brief discussion of 2D models. Figure 5.3a shows the basic structure of a 2D corner flow for an isoviscous mantle wedge for profile A. In a subduction zone, the downward motion of the slab drags the overlying mantle through viscous coupling (yellow ellipse). This creates a region of low pressure near the wedge

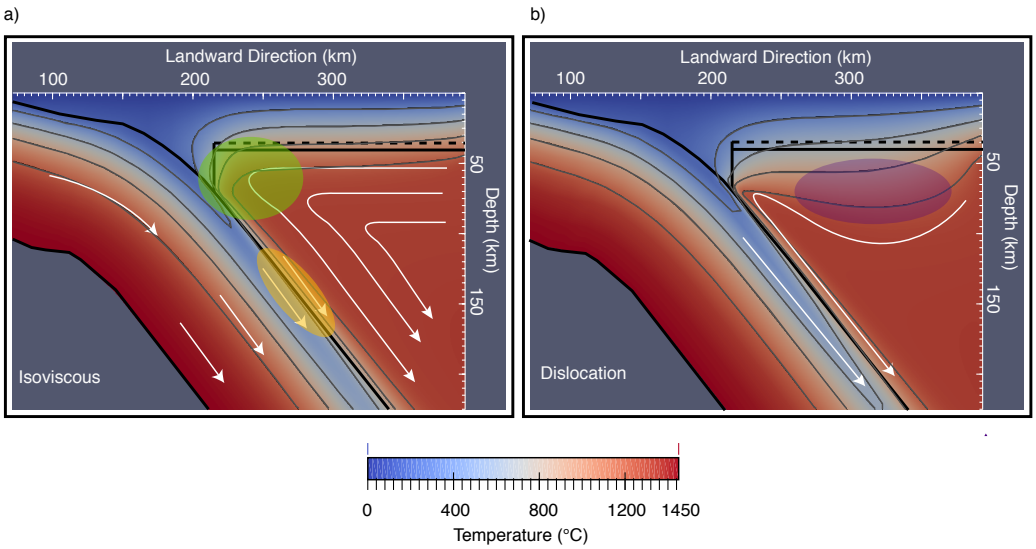

Figure 5.3 Two-dimensional (2D) corner flow models for **a** an isoviscous and **b** a dislocation creep wedge. Figures are for profile A. Black dashed line indicates the continental Moho. White arrows are streamlines. Green circle shows the low-pressure corner, which induces flow that brings hot mantle from the backarc. Yellow ellipse shows viscous coupling between slab and mantle wedge. Purple ellipse shows the stagnant lid for a dislocation creep rheology. Temperature contours are shown every 300°C .

corner (green circle) which induces flow that brings hot mantle from the backarc to replenish the lost material. The magnitude and size of this low-pressure area depends on the dip of the slab, with shallower dips tending to create lower pressures and a larger low-pressure region [Turcotte and Schubert, 2002; Manea and Gurnis, 2007]. As a result of this flow pattern, the thermal structure of the subduction zone has two distinct regimes. The forearc is relatively cool, owing to conductive cooling by the underlying oceanic plate; the arc and backarc regions are heated by the mantle wedge flow.

For an isoviscous rheology, the constant viscosity of the mantle allows flow through the backarc boundary at any depth. However, a dislocation creep rheology is temperature dependent (Equation 5.4) and thus flow is generally limited to temperatures

greater than 1200°C [van Keken et al., 2002; Currie et al., 2004]. Figure 5.3b shows a 2D model that uses a dislocation creep mantle wedge rheology. With this rheology, flow enters the model domain at a greater depth along the backarc boundary, and it is more strongly focused upward into the wedge corner, compared to the isoviscous model. As a result, the temperature in the mantle wedge corner is ∼100 to 200°C higher than for the isoviscous case. However, the upper part of the mantle wedge is essentially stagnant, leading to cool temperatures in this area (∼800°C). This region is known as the stagnant lid and is shown in Figure 5.3b by a purple ellipse.

5.3.1 Three-Dimensional Flow Field

In a three-dimensional subduction zone, the subducting plate also drags the overlying mantle downward, inducing corner flow. However, features such as along-strike changes in slab dip, obliquity, or trench curvature will induce lateral pressure gradients, which can lead to along-strike flow [Kneller and van Keken, 2008; Bengtson and van Keken, 2012]. For the case of Costa Rica-Nicaragua, along-strike variations in the dip of the Cocos plate (Figure 5.1) induce changes in the dynamic pressure within the mantle wedge (Figure 5.4). In response to this change, a component of along-strike flow is produced in the mantle wedge, with flow directed toward the south-east, from the region of high slab dip (70°) below Nicaragua to low slab dip (45°) below Costa Rica. This is consistent with the idea that a shallower dip induces lower pressures in the mantle wedge (e.g., Turcotte and Schubert [2002]; Manea and Gurnis [2007], and thus the corner flow is deflected towards the area of lower slab dip. The total flow field of the mantle wedge is therefore a combination of a 2D corner flow and lateral flow.

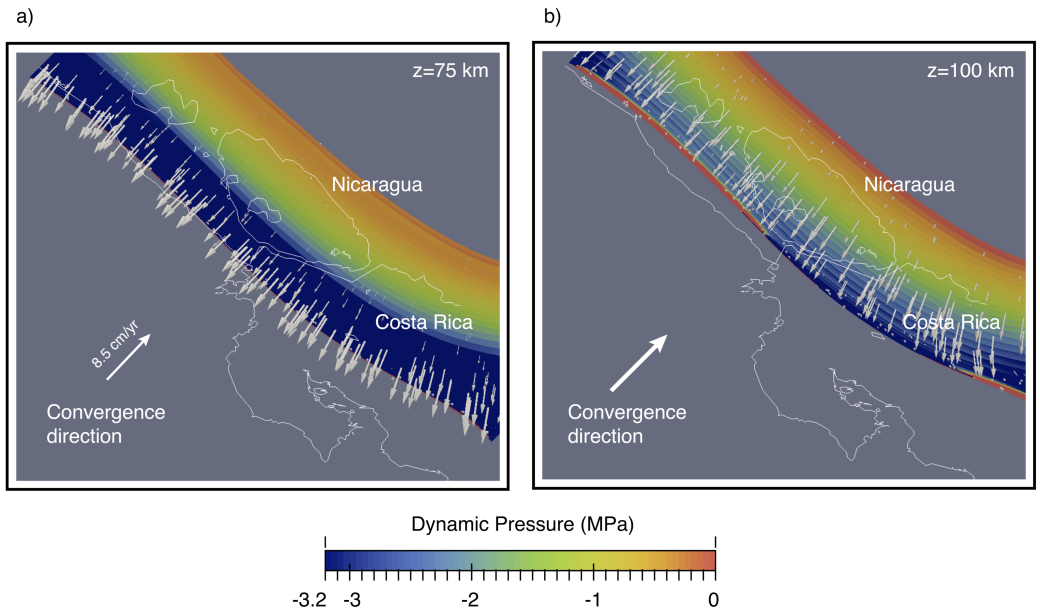

Figure 5.4 Dynamic pressure for the 3D model in horizontal planes located at depths of **a** 75 km and **b** 100 km. Color scale the magnitude in MPa. Gray arrows mantle wedge flow along each plane. Mantle wedge flow is mostly parallel (2D) to convergence direction below Nicaragua and northern Costa Rica. From mid-Nicoya to southern Costa Rica, mantle flow has an along-strike component (3D). Mantle flow departs from the 2D corner flow in response to changes in the low-pressure region (blue), which in turn are associated with changes in the dip of the slab.

Figure 5.5 shows the modeled wedge flow field for the isoviscous and dislocation creep cases. The flow field is visualized through streamlines that track the path of particles. The color scale denotes along-strike velocity (v_x), with positive values indicating northwestward flow. The dominant component of the flowfield is the slab-driven corner flow, where particles are pulled toward the wedge corner and then descend with the subducting plate. As seen in the 2D models, a dislocation creep rheology leads to a strong focusing of flow toward the wedge corner (Figure 5.3b), whereas an isoviscous wedge has subhorizontal flow in the upper part of the wedge (Figure 5.3a). In both cases, the flow also exhibits an along-strike component. This is largest below Costa Rica in the southern part of the model domain, where there

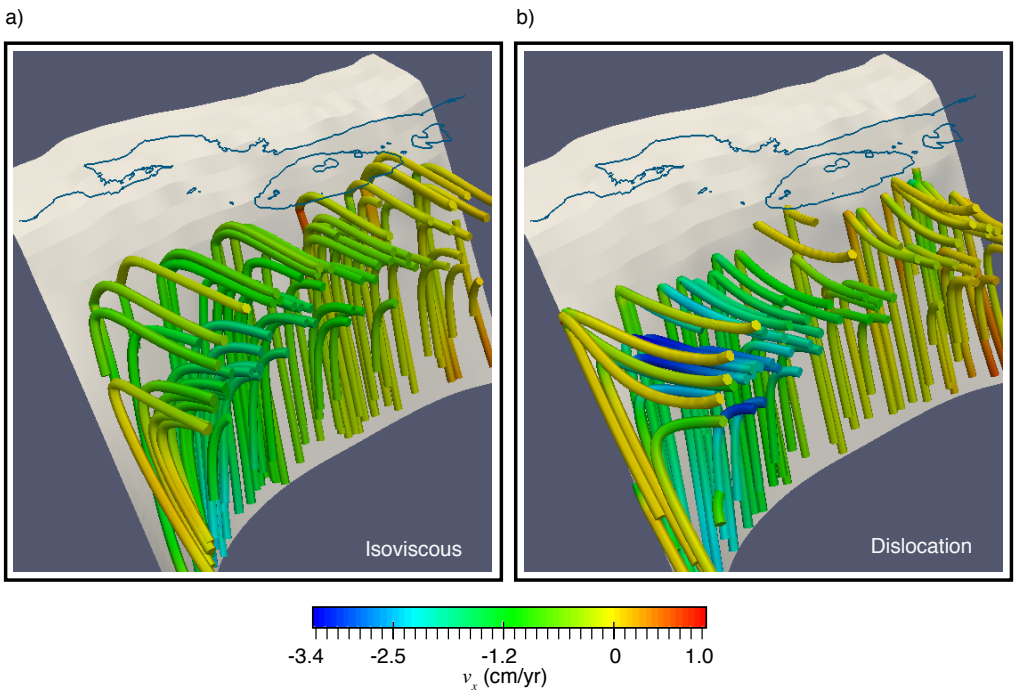

Figure 5.5 Three-dimensional flow field in the mantle wedge for a an isoviscous and b a dislocation creep rheology. Color scale denotes along-strike velocity, v_x, with blue denoting southeast flow and red denoting northwest flow. Maximum v_x for the isoviscous and dislocation creep models (not shown in figure) is -2.5 and -4.0 cm/yr, respectively.

are along- strike changes in slab dip. In the isoviscous case (Figure 5.5a), a maximum along-strike velocity of -2.5 cm/yr is observed, whereas the dislocation creep rheology results in a maximum along-strike velocity of over -4 cm/yr. This difference is caused by a lower mantle viscosity due to the higher temperatures in the dislocation creep model; flow is concentrated in the central wedge region where temperatures are highest. The along-strike flow is minimal in the northern part of the model area, as there are only minor dip variations here. It is important to mention that our current choice of boundary conditions could have an effect on the observed mantle flow. The v_x=0 restriction imposed on the side boundaries affects the flow pattern, and as a result, our 3D model may underestimate the along- strike flow component. A

detailed discussion of the effect of the boundary conditions in mantle flow is given in the Appendix.

5.3.2 Three-Dimensional Thermal Structure

Our three-dimensional thermal model for Costa Rica-Nicaragua is shown in Figure 5.6a for a dislocation creep rheology. The location of profiles A through D is shown. The detailed model results are also shown for profiles A and D for an isoviscous (Figure 5.6b) and dislocation creep rheology (Figure 5.6c). The large-scale temperature field for profile A is similar to that seen in the 2D models (Figure 5.3). If the wedge has an isoviscous rheology, isotherms are subhorizontal in the shallow backarc (Figure 5.6b). In contrast, a dislocation creep rheology leads to a strong focusing of flow from depth into the wedge corner and a cool stagnant lid is created in the backarc (Figure 5.6c).

To assess the effects of along-margin mantle flow, Figures 5.7 and 5.8 show the difference between 3D and 2D mantle wedge temperatures and the along-strike mantle flow for an isoviscous and non-Newtonian rheology, respectively. For both cases, the largest temperature difference is observed in profile A. For profiles B, C and D, the magnitude of the difference decreases in the northwestward direction. This result is consistent with the location of strong along-margin slab curvature, mostly located in the southeast side of our domain area (Figure 5.1), which creates pressure gradients that drive the flow in the southeastward direction (Figure 5.4.

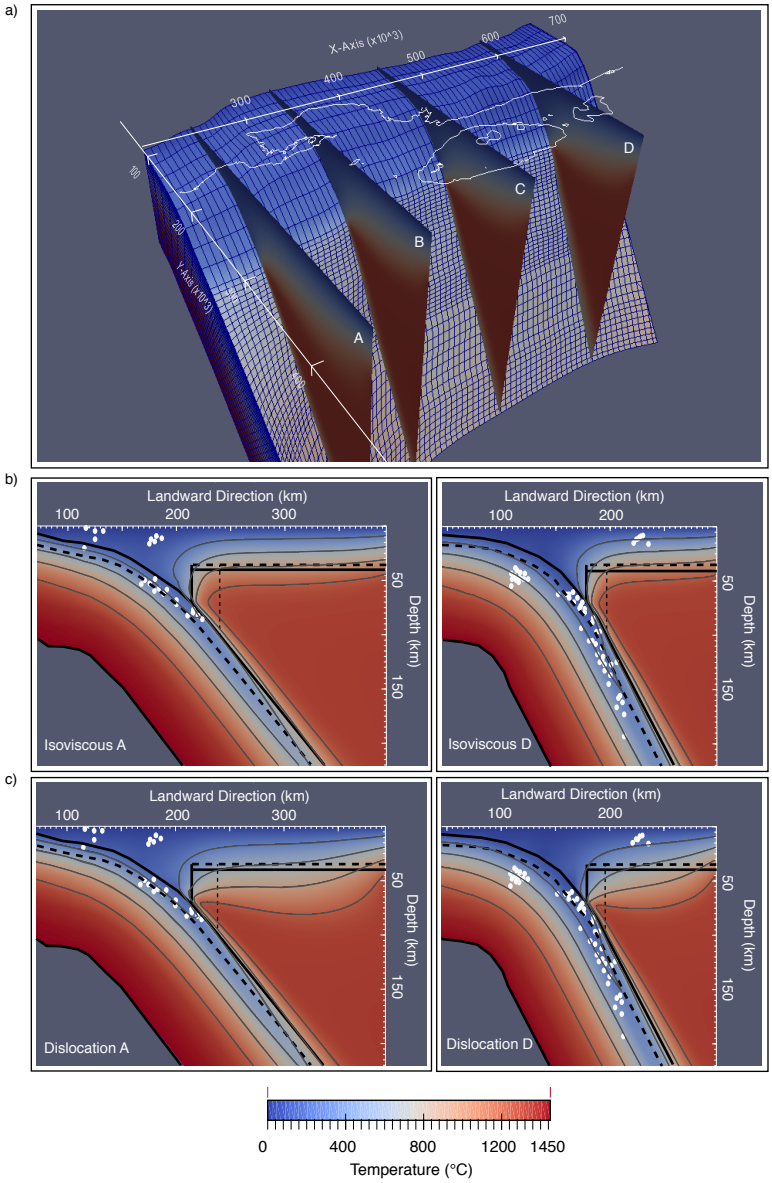

Figure 5.6 **a** Three-dimensional (3D) thermal model of the Costa Rica-Nicaragua subduction zone, with location of profiles A through D shown. The rheology for this model is dislocation creep. Cross-sections extracted from 3D model for profiles A and D are shown in two-dimensional view for **b** an isoviscous and **c** a dislocation creep rheology. Temperature contours are shown for every 300°C . White dots are seismicity from the TUCAN [Abers et al., 2004] and CRSEIZE (`http://es.ucsc.edu/~hdeshon/crseize_homepage.html`) deployments. Thick dashed lines represent the oceanic and continental Moho. Thin dashed line represents location of volcanic arc geotherm (Figure 5.10a).

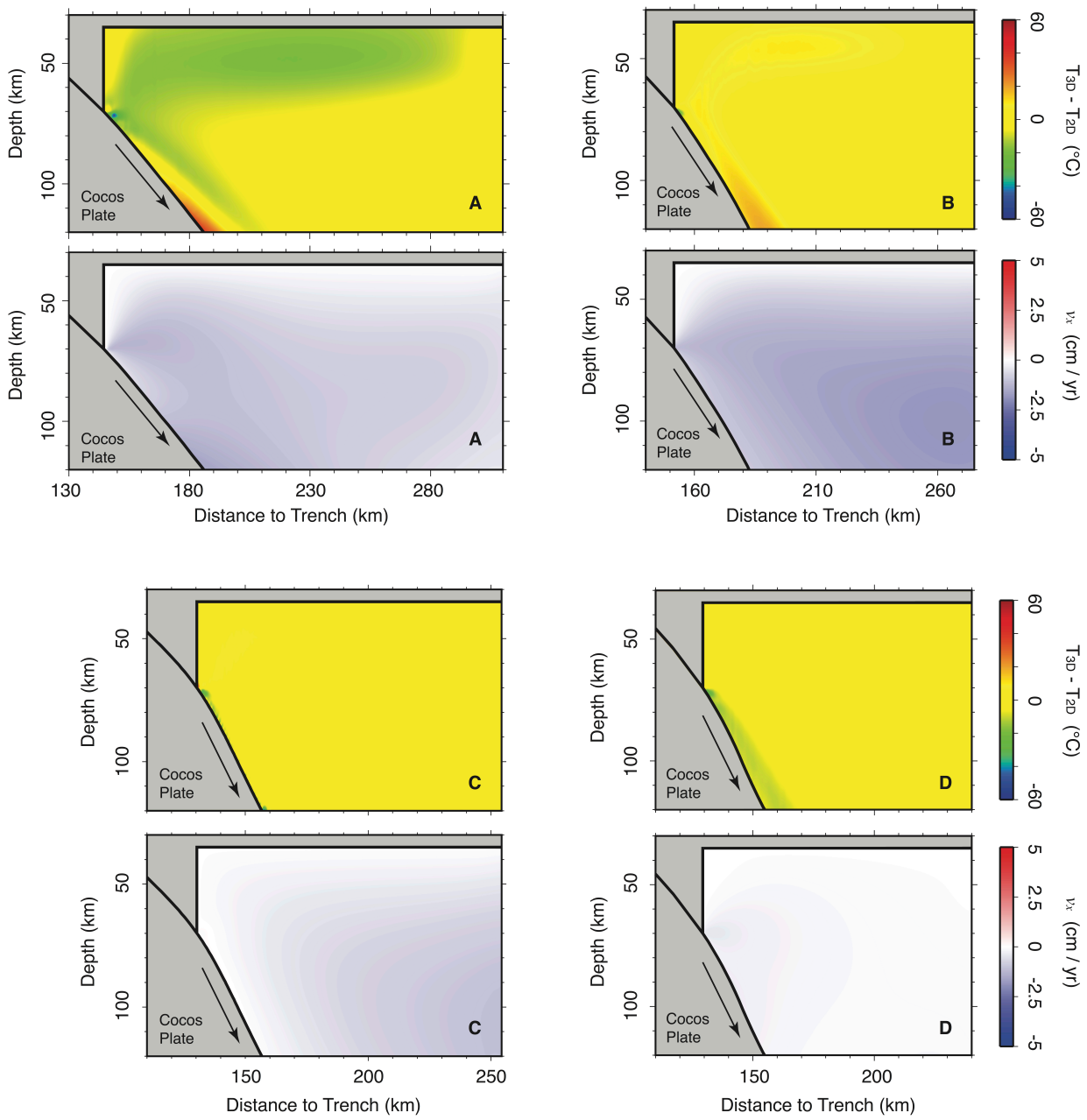

Figure 5.7 Temperature difference ($T_{3D}-T_{2D}$; upper plot) and along-strike velocity component (v_x; lower plot) for profiles A through D with an isoviscous (10^{21} Pa s) mantle wedge. Black arrow denotes subduction direction. Negative sign in the along-strike velocity indicates southeastward flow.

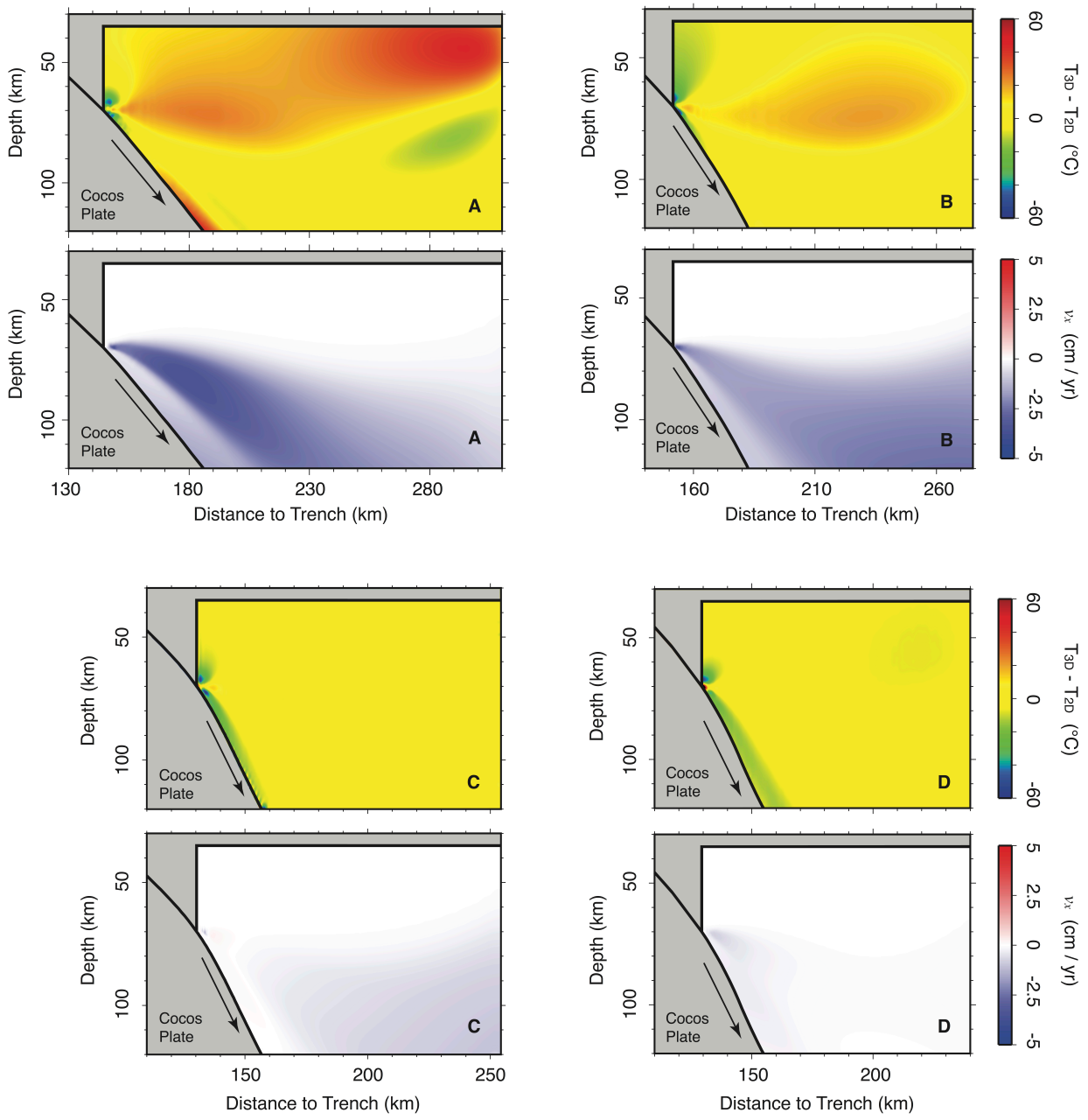

Figure 5.8 Same as in Figure 5.7, but for a non-Newtonian mantle wedge that flows through dislocation creep (Equation 5.4).

For an isoviscous rheology, the along-strike flow decreases temperatures in the 3D model by 10-30°C with respect to the 2D model along profile A (Figure 5.7). The along-strike component of the flow has a magnitude of ∼1.5 cm/yr. For profile B, temperatures do not change appreciably in the mantle wedge, despite the stronger along-strike flow (∼2 cm/yr). The difference between profiles A and B can be understood by considering the motion of a single fluid element in the mantle. Given the higher along-strike velocities along profile B, a fluid element in this area would have less time to cool than a fluid element in the vicinity of profile A at a given distance from the backarc boundary. The result is that 3D flow cools down the mantle more efficiently for profile A than for profile B. For profiles C and D, there are no variations in mantle wedge temperatures between 2D and 3D models and almost no along-strike flow (>1 cm/yr), indicating the mantle flow in this region is mostly 2D corner flow.

For a mantle with a dislocation creep rheology (Figure 5.8), the temperature differences between 2D and 3D models are largest for profile A, but the effect of 3D flow is opposite to that in the isoviscous case. For this profile, the mantle wedge in the 3D model is up to 50°C hotter than the 2D model, with the largest change in the uppermost mantle (stagnant lid). The along-strike flow has a maximum magnitude of ∼4 cm/yr for profile A. The thermal changes decrease in the northwest direction. Profile B still shows a difference of 20°C , with an along-strike flow of ∼2.5 cm/yr. For profiles C and D, only minor changes in the mantle wedge temperatures are observed. In these models, the viscosity of the mantle wedge depends on both the temperature and stress (Equation 5.4), which results in a more complex feedback between the flow field and thermal structure than for the isoviscous case. In general, however, the along-strike flow for the dislocation creep case has a relatively higher magnitude than in the isoviscous case. This rapid flow may limit the thickness of the stagnant lid, and as a result, the upper part of the mantle wedge will be somewhat warmer

compared to a purely 2D model.

On all profiles, moderate changes in thermal structure are observed in a local region (<5 km wide) in the wedge corner near the stagnant wedge bound- ary (Figures 5.8 and 5.9). This region is characterized by strong pressure and thermal gradients that require high resolution to properly resolve for the temperature [van Keken et al., 2002]. Thus, the temperatures in the wedge corner have some uncertainty that may arise from numerical artifacts.

5.4 Thermal Structure of the Costa Rica-Nicaragua Subduction Zone

The thermal structure of a subduction zone is a crucial control on key processes, including magmatism, slab metamorphism and dehydration, and earthquake distribution. Here, we examine the temperatures of the subducting slab and mantle wedge of our full 3D model with a dislocation creep rheology (Figure 5.6a). Seismic anisotropy studies for Central America suggest flow by dislocation creep is the most appropriate rheology [Hoernle et al., 2008].

5.4.1 Megathrust Earthquake Seismogenic Zone

We first address the implications of the 3D thermal model for megathrust earthquakes, which are earthquakes that occur on the subduction interface. The seismogenic zone corresponds to the part of the interface that exhibits velocity-weakening behavior, and this may depend on interface temperatures (e.g.,Hyndman et al. [1997]). The updip limit is usually placed at temperatures of 100-150°C , while the downdip limit is at either 350-450°C or the intersection between the interface and the upper plate

Moho.

Figure 5.9 shows pressure-temperature (PT) paths for the surface of the Cocos plate for profiles A through D, for both the 3D (solid line) and 2D (dashed line) models with a dislocation creep mantle; note that pressure has been converted to depth using the material density. A temperature of 100°C occurs at a depth of 15-20 km for the southern profiles (A and B), and at ∼10 km depth for the northern profiles (C and D). For all profiles, a temperature of 350°C occurs at depths greater than 60 km. The Moho depth for the Caribbean plate is 35 km [MacKenzie et al., 2008]. Thus, it is likely that the downdip limit of the seismogenic zone corresponds to the Moho intersection and not the 350°C isotherm. This is consistent with the conclusion of [Harris et al., 2010b].

Figure 5.10 shows a map view of the location of the 100°C isotherm on the subduction interface for our 3D model, as well as the location of the Moho intersection (corresponding to a slab depth of 35 km). There is an abrupt seaward shift in the position of the 100°C isotherm at the position of the Nicoya Peninsula. This point marks the change from oceanic lithosphere created at the East Pacific Rise (EPR) in the north and Cocos-Nazca Spreading Centre (CNS) in the south (Figure 5.1 1). At the trench, the incoming EPR lithosphere is cooler than the CNS lithosphere (Figure 5.2b), which translates to a cooler subduction interface and a more landward location of the 100°C isotherm for the EPR segment. For the CNS segment, the predicted seismogenic zone starts at 20-30 km from the trench and terminates at 70 km from the trench. In contrast, a seismogenic zone width of 20-30 km is predicted for the southeastern EPR segment, starting at 70-80 km from the trench. The width of the predicted seismogenic zone then decreases dramatically to a width of 10 km or less close to the border of Costa Rica with Nicaragua, and remains like that further northwest along the margin.

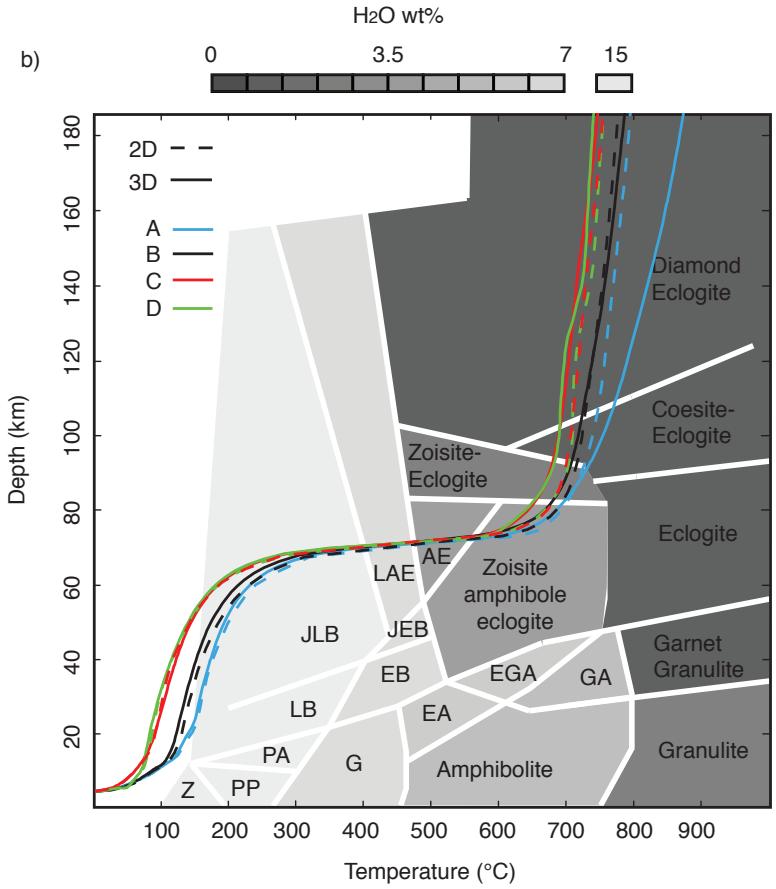

Figure 5.9 Phase diagram for mid-ocean ridge basalt (MORB), showing pressure-temperature (PT) paths for the surface of the slab for profiles A through D. Solid lines are for 3D models, and dashed lines are for 2D models. Shades of gray denote water content. Phase diagram from Hacker et al. [2003]. Metamorphic facies: A amphibolite, AE amphibole eclogite, EA epidote amphibolite, EB epidote blueschist, EGA epidote garnet amphibolite, G greenschist, GA garnet amphibolite, JLB jadeite lawsonite blueschist, JEB jadeite epidote blueschist, LAE lawsonite amphibole, JLB jadeite lawsonite blueschist, LB lawsonite blueschist, PP prehnite pumpellyite, Z zeolite.

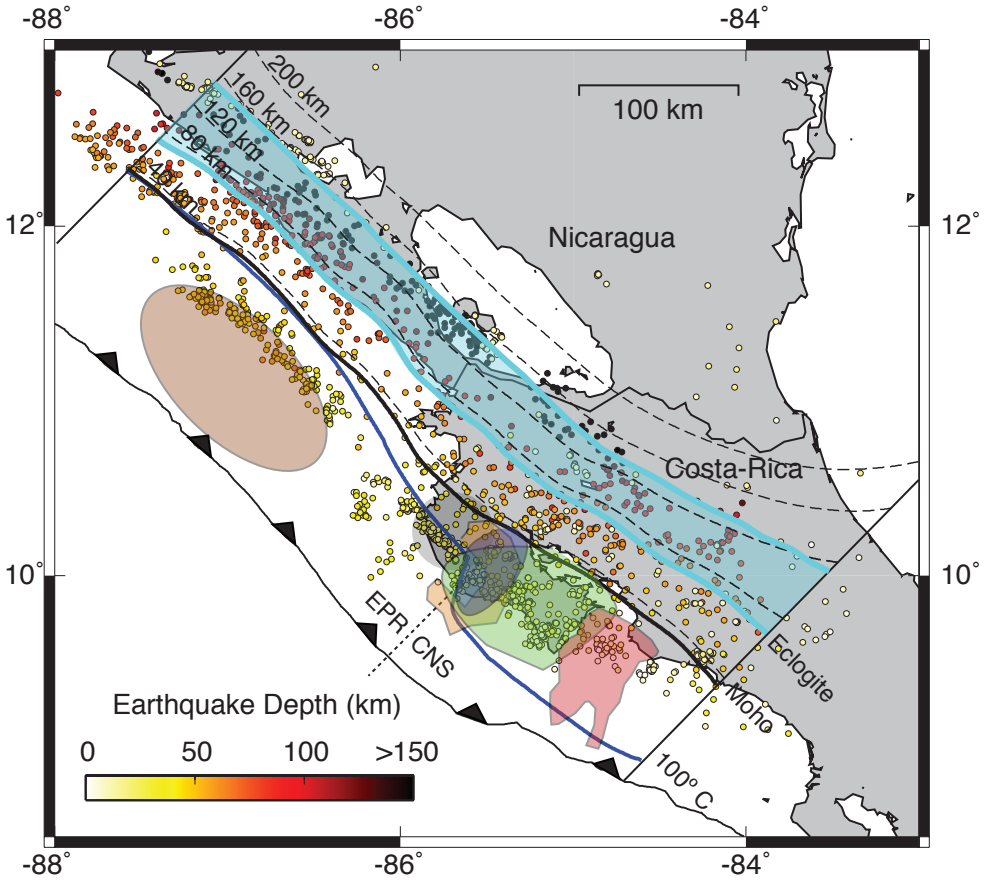

Figure 5.10 Map of the modeling area, with earthquake locations obtained by the TUCAN [Abers et al., 2004] and CRSEIZE (`http://es.ucsc.edu/~hdeshon/crseize_homepage.html`) deployments. The 100°C isotherm for the slab surface is shown in dark blue. The range over which the entire oceanic crust transforms to eclogite is shown in light blue. The intersection of the slab surface with the upper plate (Caribbean) Moho is shown in black. Slab depth contours are shown with dashed black lines. Approximate rupture areas for the 1900 (black *Mw* 7.2), 1950 (green *Mw* 7.7), 1978 (blue *Mw* 6.9), 1990 (red *Mw* 7.0), and 2012 (orange *Mw* 7.6) Nicoya megathrust earthquakes [Yue et al., 2013; Protti et al., 2014], as well as the 1992 (brown *Mw* 7.7) Nicaragua earthquake [Kanamori and Kikuchi, 1993] are shown. The dotted line divides East Pacific Rise (EPR) and Cocos-Nazca Spreading Centre (CNS) lithospheres.

Figure 5.10 also shows rupture areas for several historical megathrust earthquakes in the Nicoya region [Yue et al., 2013; Protti et al., 2014]. Each rupture area is roughly constrained by our model- predicted megathrust seismogenic zone. Of particular importance is the reduction in width of the predicted seismogenic zone in northern Nicoya, which correlates well with the reduction in rupture area for the 1900 (black), 1999 (blue) and 2012 (orange) Nicoya earthquakes. Further north, however, our results do not fit the inferred rupture area of the 1992 Nicaragua earthquake [Kanamori and Kikuchi, 1993]. Our model predicts a cool subduction interface, such that the critical temperature for the updip limit of the seismogenic zone is not reached until a depth of ∼35 km. This could indicate that our chosen geotherm for the north EPR section is too cold. We also note that the published depth of this earthquake is 45 km, which places it well below the subduction interface [Kikuchi and Kanamori, 1995], indicating that this earthquake may not have occurred on the plate interface.

In general, the predicted megathrust seismogenic zone in our 3D models is in good agreement with that of previous 2D thermal models for this region [Harris et al., 2010b], as well as other studies of the megathrust seismogenic zone that rely on more direct methods, such as earthquake locations and GPS observations [Newman et al., 2002; DeShon et al., 2006; Schwartz and Deshon, 2007]. It should be noted that the temperatures of the shallow plate interface are primarily determined by the thermal structure of the oceanic plate at the trench, as well as its geometry and convergence rate; mantle wedge flow does not significantly affect the shallow interface temperatures. The good agreement between our 3D models and previous 2D models suggests that along-margin heat transport is negligible for the shallow subduction interface. As shown in Figure 5.10, the transition in the location of the 100°C isotherm between the EPR and CNS segments occurs over an along-strike width of less than 30 km, suggesting that 2D models are suitable for modeling interface temperatures

for much of this subduction zone.

5.4.2 Slab Temperatures and Eclogitization of the Cocos Plate

The width of the megathrust seismogenic zone is controlled by the temperature along the interface between the oceanic plate and the overriding plate. For deeper sections within the plate, temperature also regulates the depth of release of water stored in the plate and the distribution of intraslab earthquakes [Kirby et al., 1996]. As the Cocos plate subducts, it is progressively being exposed to greater pressures and temperatures, causing it to undergo several metamorphic and dehydration reactions. The main components of the oceanic crust and mantle lithosphere are mid-ocean ridge basalt (MORB) and harzburgite, respectively [Irifune, 1993]. For the case of the oceanic crust, the MORB eventually transforms to eclogite. This process dehydrates the slab and significantly increases its density. For the oceanic mantle lithosphere, hydration of harzburgite leads to serpentinization of the mantle. Serpentinite is usually stable until depths of 60-70 km for most subduction zones [Schmidt and Poli, 2003]. At larger depths, serpentinite starts to dehydrate. In general, water trapped in serpentinized harzburgite may be the most efficient transport mechanism of water to the deep mantle [Rupke et al., 2004]. For this study, however, we only investigated the 3D temperature distribution within the oceanic crust. A full discussion of lithosphere mantle temperatures and dehydration is given in Rosas et al. [2015, submitted].

Figure 5.9 shows the PT paths of the top of the Cocos plate superimposed on a phase diagram for MORB [Hacker et al., 2003]. The PT paths show minimal variations between 3D and 2D models at shallow depths. For all 4 profiles, the surface of the slab goes through the jadeite lawsonite blueschist (JLB) and lawsonite amphibole eclogite (LAE) facies, before entering the amphibole eclogite (AE) facies

at 70-75 km depth. At this point, the oceanic crust is almost dry, with less than 2 wt% H2O. At greater depths, differences between 3D and 2D models are larger due to along-strike flow. For profile A, the difference between 3D and 2D models steadily increases with depth. At a depth of 180 km, the difference is 80-90°C . For profiles B, C and D, the difference is much less (10-20°C).

Figure 5.10 shows a map view of the predicted location of the transition to eclogite (light blue) in the oceanic crust for our 3D model, assuming no kinetic delay. The seaward boundary of the region represents the point at which the top of the slab transforms to eclogite (Figure 5.9), whereas the landward boundary represents the point at which the entire oceanic crust (assumed to have a thickness of 7 km) is predicted to undergo complete eclogitization. The depth for complete eclogitization of the oceanic crust ranges between 120 and 160 km along our modeling area. The predicted phase change can be compared to the location of intraslab earthquakes. Earthquake locations were obtained from the TUCAN seismic experiment [Abers et al., 2004] and UCSC-CRSEIZEA data archive (`http://es.ucsc.edu/~hdeshon/crseize_homepage.html`). Figure 5.6c shows the location of intraslab earthquakes along Profiles A and D. For these profiles, earthquakes in the oceanic crust are absent at depths of >90-100 and >170 km, respectively, consistent with the predicted range for eclogitization of our 3D model.

5.4.3 Mantle Wedge Temperatures and Flow Field

Mantle wedge temperatures are important for the generation of melt and arc volcanism. Depending in the amount of water in the mantle wedge, tempera- tures of 1100-1300°C are needed for melting [Schmidt and Poli, 1998]. Figure 5.11 shows the geotherms along a vertical line located at a point where the slab reaches a depth of

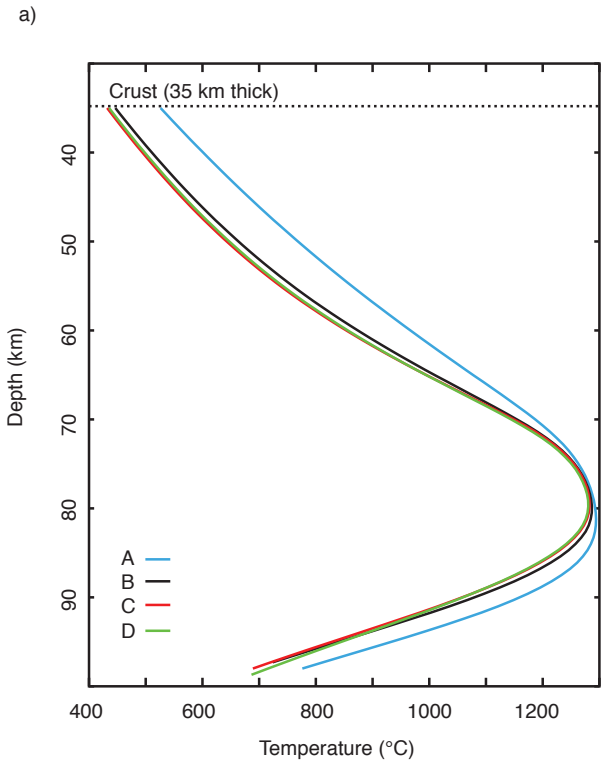

Figure 5.11 Volcanic arc geotherms for profiles A through D for our 3D thermal model. Geotherms were taken along a vertical line located at a point where the slab reaches a depth of 100 km (see Figure 5.6c for profiles A and C). Thin dashed line shows the Moho of the continental crust.

100 km, consistent with the global average location of the volcanic arc [Syracuse and Abers, 2006]. For profile A, temperatures are up to 100°C higher than for the other profiles. As shown in Figure 5.8, 3D modeling predicts larger temperatures than 2D modeling (up to 40°C) below the volcanic arc for this profile. It is unclear how this will affect melt production and arc volcanism, as melting also depends on the water content [Schmidt and Poli, 1998]. Assuming a similar water content for the mantle wedge along the strike, the higher temperatures observed below Costa Rica would suggest more melting in this region than for Nicaragua. However, seismic studies near the trench show that the incoming Cocos plate might carry large amounts of water along its Nicaraguan section, where significant fracturing occurs in the outer

rise prior to subduction [Abers et al., 2003; Syracuse et al., 2008; Rychert et al., 2008; Van Avendonk et al., 2011; Dinc et al., 2011]. Thus, the Cocos plate may release more water into the wedge below Nicaragua than for Costa Rica, which can significantly affect the generation of melt.

As discussed in Section 5.3.1, an important result from our 3D models is that the observed along-strike changes in the slab geometry can induce along-strike mantle flow of up to 4 cm/yr (Figure 5.4b). In our models, significant along-strike flow toward the southeast is predicted below Costa Rica. This flow is driven by the southward decrease in dip angle of the subducting plate. In contrast, geochemical and seismic studies indicate a northward lateral flow, with a magnitude of 6-19 cm/yr [Hoernle et al., 2008]. Our models show that such flow is not driven by along-strike changes in slab dip and trench curvature. If these observations are correct, an additional driving mechanism for along-strike flow must be considered. One possibility is mantle flow through the slab window just to the southeast of the study area (Figure 5.1). Such flow may be enhanced by rollback of the Cocos plate as it subducts. Given that our moderate along-strike flow can increase temperatures by up to 40°C in the mantle wedge (Figures 5.8 and 5.11) and by 80-90°C along the slab at depths >180 km (Figure 5.9) along profile A, we expect the 6-19 cm/yr flow predicted by geochemical studies to have an even larger effect on mantle and slab temperatures. We are currently working on numerical models that incorporate this flow to assess its effect in the thermal structure of the subduction zone.

5.5 Conclusions

Previous 3D thermal modeling studies of sub- duction zones investigated the relation between flow and anisotropy [Kneller and van Keken, 2008] or the effects of obliq-

uity and trench curvature on slab surface temperatures [Bengtson and van Keken, 2012]. However, these studies do not discuss the thermal structure of the wedge in detail. Wada et al. [2015] presented a 3D thermal model for the sub- duction zone of northeast Japan and found that the obliquity of the trench generates an along-strike flow component that results in a different thermal structure than for a 2D corner flow model. In our study, we present the first 3D model of the Costa Rica-Nicaragua subduction zone.

The key conclusions of this work are:

1. *Velocity field for the mantle:* Variations in the slab dip in the Costa Rica-Nicaragua subduction zone lead to along-strike mantle flow, with a maximum magnitude of 2.5 cm/yr for an isoviscous wedge and 4 cm/yr for a wedge that deforms through dislocation creep (approximately 40% of the slab convergence rate). The predicted flow direction is toward the southeast, in the direction of decreasing slab dip. This is opposite to the flow direction inferred from geochemical and seismic observations [Hoernle et al., 2008], which suggests that an additional mechanism to create along-margin flow is needed for this subduction zone. Just south of our modeling area, there appears to be a slab window that is created by the subduction of the Cocos-Nazca spreading centre [Johnston and Thorkelson, 1997; Abratis and Worner, 2001]. Future 3D models should investigate how this may affect the mantle wedge flow field, especially below Costa Rica.

2. *Thermal effects of 3D mantle flow:* The thermal structure of the subduction zone depends on the rheology of the mantle wedge. In addition, along-strike flow can change the temperature of the mantle wedge. In our 3D models, we find that along-strike flow of an isoviscous wedge results in cooler temperatures below the

volcanic arc with respect to the corresponding 2D model. A dislocation creep rheology has the opposite effect: higher along-strike flow velocities lead to a hotter 3D model. The temperature differences between 2D and 3D are up to 50°C and are largest below central Costa Rica (profile A), where along-strike flow has the highest magnitude. Given that dislocation creep is considered the primary mechanism for mantle wedge deformation and that dislocation creep has the opposite effect on temperatures than the isoviscous case, we conclude that 3D isoviscous are probably not well suited for studies of 3D subduction zone thermal structure.

3. *Slab temperatures in Costa Rica-Nicaragua:* The temperatures of the shallow subducting plate (<35 km depth) are not significantly altered by 3D effects. Our predicted megathrust seismogenic zone correlates well with that obtained in other 2D modeling studies [Harris et al., 2010b] in the vicinity of the Nicoya peninsula. It also matches rupture areas of historical earthquakes in this area. For the Nicaragua section, our model suggests a very narrow seismogenic zone (<10 km wide). This does not fit the observed rupture area of the 1992 earthquake (Figure 5.9), and this discrepancy needs to be explored in more detail. For the deeper parts of the slab, temperatures are affected by mantle wedge flow, resulting in difference of up to 80-90°C between 2D and 3D modeling. This can affect factors such as eclogitization and dehydration of the subducting oceanic plate, as well as the stability of serpentinized mantle within the subducting mantle.

4. *Applicability of two-dimensional models to the Costa Rica-Nicaragua Subduction Zone:* Our 3D models show that changes in slab dip lead to along-strike flow up to 4 cm/yr, which results in temperature variations up to 50°C for the

subducting oceanic plate and mantle wedge compared to 2D models. This variation may have implications for metamorphism and dehydration of the deep slab and mantle wedge melting. In addition, if the significant along-strike flow (6-19 cm/yr) from geochemical and seismic studies [Hoernle et al., 2008] is correct, it is reasonable to expect thermal changes that are much larger than those observed in our study. This indicates that 2D models are not suitable for modeling the thermal structure of the Costa Rica-Nicaragua subduction zone at mantle depths, as they are unable to capture all the complexity of mantle wedge dynamics.

5.6 Appendix

In Section 5.2, the side boundaries of the model domain are described as free-slip, insulated boundaries. This no-flow condition (v_x=0) forces the mantle to follow a 2D corner flow pattern near the side boundaries. In 3D models, along-strike flow can result from along-strike changes in the dip, trench curvature, or obliquity in convergence direction relative to the trench. Thus, it is clear that the side boundary conditions become important, and may adversely affect the model results if there are any of these geometrical factors near the boundaries, as the v_x=0 restriction would act to inhibit any along-strike flow.

For our Costa Rica-Nicaragua model, profiles A and D are the closest ones to the southeast and northwest boundaries, respectively. For profile A, the dip at depths of ∼40 km changes from ∼70° below northern Costa Rica to ∼45° in central and southern Costa Rica. The thermal changes between 3D and 2D models observed in Figures 5.8 and 5.9 result from this change in slab dip. However, the distance of this profile to the side boundary is 50 km, which means that the effect of the no-

flow boundary condition described above could affect the along-strike component of mantle flow and the resulting temperature distribution.

To assess the effects of the side boundary, we have tested an additional model in which the along-strike model width is increased by 250 km. Figure 5.12 shows the top view of the extended 3D model, with the original boundaries indicated. In the extended model, the southern boundary is 150 km south of the original model boundary. To assign the slab geometry in the new region, there are two possibilities. First, the slab geometry from Kyriakopoulos et al. [2015] could be used (Figure 5.1). However, the data show a significant decrease in dip south of the original model area, with a slab that is imaged to a maximum depth of $\sim$75 km at the southern limit of the Kyriakopoulos et al. [2015] study. This is a problem because of the maximum slab depth of 300 km imposed in our models. To solve this, we could extrapolate the slab geometry to a depth of 300 km, but this would result in a considerable shift of the backarc boundary in the landward direction, resulting in a highly distorted model geometry, which may lead to further numerical artifacts. We also note a complete absence of volcanoes (Figure 5.1) and slab seismicity at depths >100 km [Protti et al., 1995] in this region, which suggest that the slab geometry should not be simply extrapolated to 300 km depth.

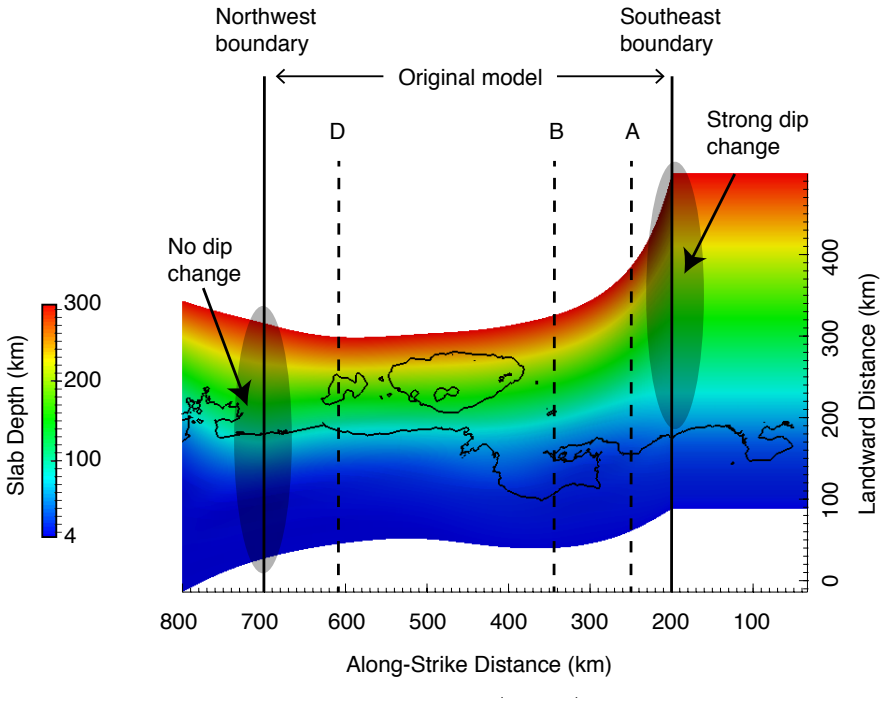

Figure 5.12 Slab geometry of the 3D extended model. Color scale denotes the depth of the slab. Solid black lines are the original model boundaries; dashed lines the location of the profiles A, B and D. Profile C is omitted, as it is located far away from the boundaries. In the extended model, the southeast boundary is located 150 km further south of that in the original model, assuming a constant slab geometry. For the northwest boundary, the extended model is 100 km further south of the original model boundary and the slab geometry is taken from Kyriakopoulos et al. [2015]. Black circle in the vicinity of the southern boundary shows the location of a strong along-strike dip gradient. For the northwest boundary, no significant dip gradient is observed.

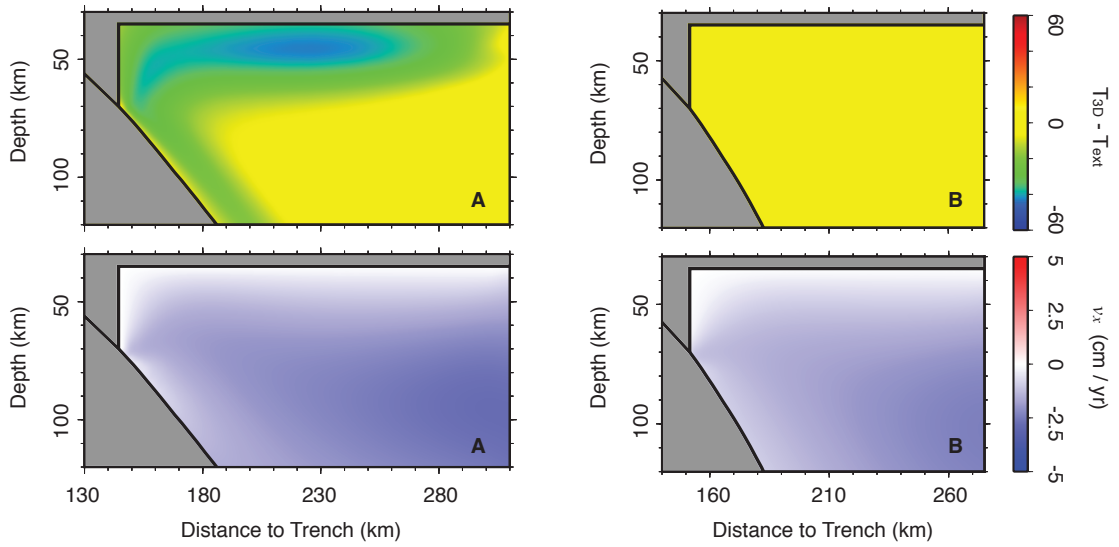

Figure 5.13 Thermal difference between the original 3D model (T_{3D}) and the extended 3D model (T_{ext}), and the along-strike velocity component for the extended model, for profiles A and B.

A second possibility is to take the geometry of the south boundary and apply it to the new section of the model. This would allow along-margin flow to pass through the original model boundary and therefore reduce the effect of the no-flow boundary condition on temperatures near the boundary. However, because the extended region has a constant dip, a strong along-strike gradient in dip is generated near the location of the original boundary (black circle in Figure 5.12).

Figure 5.13 shows the temperature difference between the original 3D model and the extended 3D model, for a mantle wedge with an isoviscous rheology. The slab geometry of the extended region is the geometry of the south boundary, as discussed in the previous paragraph. The figure also shows the along-strike flow component for profiles A and B in the extended model; the along-strike flow for these profiles in the original model is shown in Figure 5.7. For profile A, the extended model has that temperatures in the upper mantle wedge are ∼30 to 50°C cooler than in the original

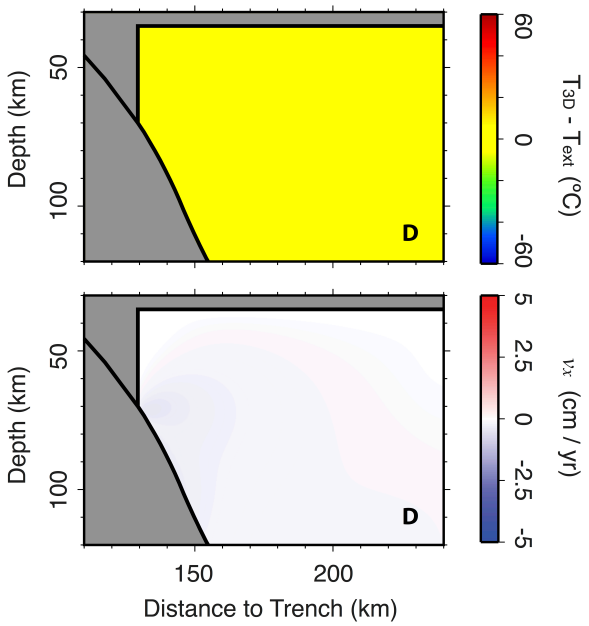

Figure 5.14 Same as Figure 5.13, but for profile D.

models. This appears to be related to the higher magnitude of along-strike flow that is generated in the extended model (compare Figures 5.7 and 5.13). For profile B, there is very little difference between our original model and the extended model, which indicates that the boundary condition does not influence the thermal structure at this location.

From this, we conclude that the model results for Profile A in the original models may be affected by the side boundary. However, as the geometry from the extended model is not a real feature of the Cocos plate (is merely an extension of the geometry from the south boundary of the original model), the large temperature change observed in Figure 5.13 is also not a feature that would be observed in reality. We thus prefer the original model over the extended model because the former is limited to real features of the slab geometry as provided by Kyriakopoulos et al. [2015], although we acknowledge the effect of the side boundary is important.

At the north end of the modeling area, the original side boundary is moved 100 km to the north in the extended model, and the slab geometry in this section uses the geometry from Kyriakopoulos et al. [2015] (Figure 5.12). In the extended geometry, profile D is located 190 km away from the boundary. The along-strike variations in dip near this profile are not as large as for profile A. Figure 5.14 shows there are negligible differences in the thermal structure and a comparison of the along-strike velocity for this profile in Figures 5.8 (original model) and 5.14 (extended model) shows no obvious difference. Therefore, we do not believe that there are any adverse effects from the side boundary at the north end of our original models.

Acknowledgments

We thank Christodoulos Kyriakopoulos for providing the updated geometry of the Cocos plate prior to publication, Felipe da Cruz Pimentel Moreira Santos for his technical support in creating the 2D meshes, Geoffrey Abers and Ellen Syracuse for providing earthquake locations shown in Figures 5.4 and 5.11, and Robert Harris for discussions about hydrothermal circulation. We also thank Ikuko Wada and Vlad Manea for helpful and thoughtful reviews and William Bandy for his editorial handling of the manuscript. Research was funded by the Natural Sciences and Engineering Research Council of Canada (NSERC) and the National Council for Science and Technology of Mexico (CONACYT).

Chapter 6

Three-Dimensional Mantle Wedge Flow and Thermal Structure in the Mexican Subduction Zone

This chapter will be submitted to Earth and Planetary Science Letters (EPSL).

Rosas, J., Pimentel, F., Currie, C., He, J., and Harris, R.

Abstract

Mantle wedge flow is an important control on the thermal structure of subduction zones. This flow is usually modeled as two-dimensional corner flow driven by the drag exerted by the downgoing plate. If variations in the along-strike geometry of the plate are present (e.g. changes in the angle in subduction), along-strike pressure gradients arise and the flow field becomes three-dimensional. In this study, we present steady-state models with a kinematically preescribed slab to analyze the flow pattern of the mantle wedge in the Mexican subduction zone. We employ a three-dimensional slab geometry that extends from the western state of Jalisco to the state of Oaxaca, in central Mexico. Our model use a continous slab that con-

nects the ∼40° -dipping Cocos plate in west-central Mexico with the the flat-slab section observed in central Mexico. This change in the subduction geometry induces significant along-strike flow, with a maximum magnitude of 3.6 cm/yr in the eastward direction. Along-strike flow also perturbs the thermal structure of the mantle wedge when compared to typical two-dimensional corner flow models. A maximum temperature change of 75°C is observed in the transition between the normal-dipping and the flat-slab sections. Finally, our wedge flow is compared to the available seismic anisotropy pattern observed in Mexico. The flow direction is found to be consistent with the fast directions in the mantle wedge throughout our model. This suggests wedge flow above the Cocos plate in Mexico is driven by along-strike changes in the angle of subduction, and not by the presence of a slab gap along the Orozco fracture zone that allows asthenospheric mantle to penetrate into the wedge, as previously suggested. Given this, for the origin of the Tzitzio gap and the termination of the ultra-slow velocity layer observed along the Orozco fracture zone, we propose they are related to a thermal disturbance in the region originated from the combined effect of along-strike changes in the age of the Cocos plate at the trench, changes in the efficiency of hydrothermal circulation prior to subduction, and variable amounts of water stored and released by the subducted Cocos plate.

6.1 Introduction

Mantle wedge flow is an important control on the thermal structure of subduction zones. Advection of hot backarc material into the wedge corner facilitates mantle melting by increasing its temperature, as well as affecting dehydration and metamorphic processes within the subducting oceanic plate [Schmidt and Poli, 1998; Schmidt and Poli, 2003]. The flow is generally assumed to be driven by viscous coupling with the downgoing plate (slab). As mantle is carried downward above the slab, mantle from the backarc is pulled into the wedge corner, creating an area of low pressure. This results in a two-dimensional (2D) corner-flow pattern for the mantle wedge

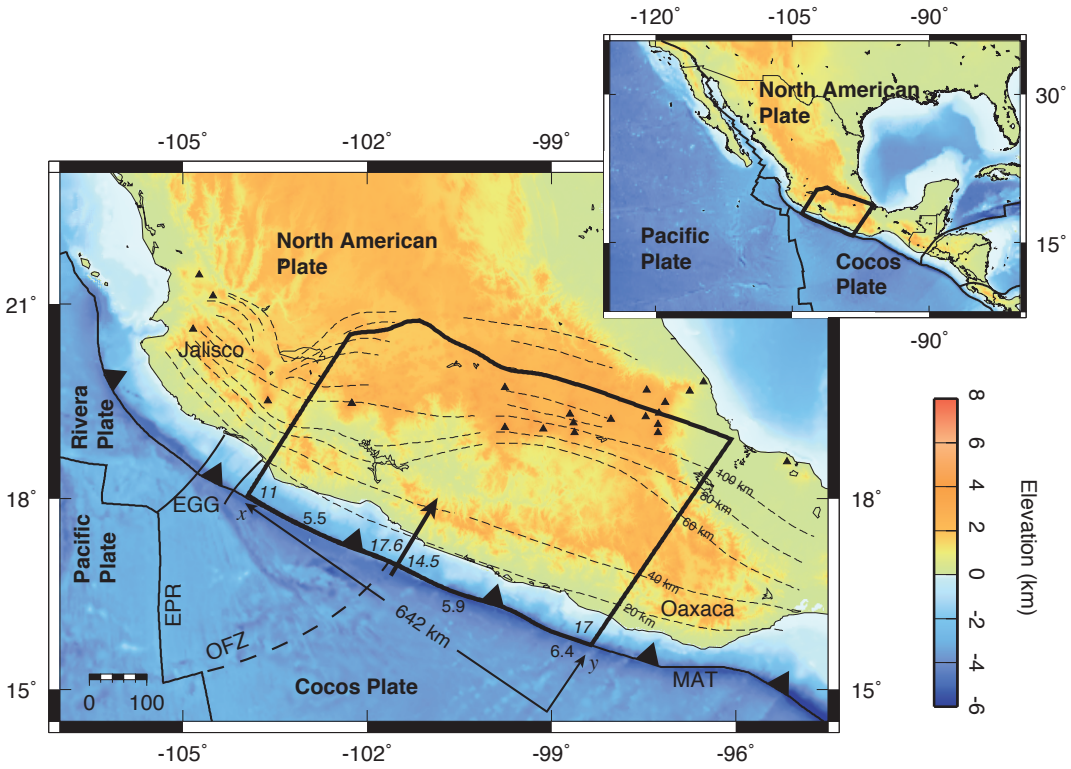

Figure 6.1 Map of the Mexican subduction zone. Locations of the Cocos, Rivera, Pacific and North American plates are shown, as well as the East-Pacific Rise (EPR), the El Gordo Grabben (EGG) and the Orozco fracture zone (OFZ). Age of the Cocos plate in Myr prior to subduction is shown near the trench in italics; convergence rate is shown in regular letters. Dashed lines are depth contours for the subducted Cocos plate; solid line are the 3D model boundaries. Slab contours are obtained from the MARS, MASE and VEOX arrays. Regions in which the slab contour is missing are due to poor space coverage of the arrays. For 3D slab, these areas were connected through a smooth surface. Black triangles represent active volcanoes. Arrow denotes subduction direction of our 3D model (fixed at 6 cm/yr). Coordinate axis for the model is also shown, with model size in the x-direction indicated. Location of the states of Jalisco (west) and Oaxaca (east) is also shown. Inset shows study area on a larger scale. Plate boundaries are from Bird [2003].

[Peacock, 1996; Batchelor, 2000; van Keken et al., 2002]. In addition to this, along-strike pressure gradients might arise due to the presence of three-dimensional (3D) changes in the subduction geometry (e.g. along-strike variations in the angle of subduction, trench curvature, or the presence of slab edges) or oblique convergence, which might lead to along-strike mantle flow [Kneller and van Keken, 2008; Bengtson and van Keken, 2012; Wada et al., 2015; Rosas et al., 2016].

High-resolution, 2D corner flow models with a kinematically-preescribed slab and a dynamic mantle wedge have been in use for a number of years [Peacock, 1996; Peacock and Wang, 1999; van Keken et al., 2002; Currie et al., 2002, 2004; Peacock et al., 2005; van Keken et al., 2008; Wada et al., 2008; Harris et al., 2010b]. One important conclusion from these models is that the thermal effects of the flow depend on the rheology of the mantle. A stress- and temperature-dependent rheology results in higher temperatures (200-400°C below the volcanic arc) and faster flow velocities than an isoviscous mantle [van Keken et al., 2002; Currie et al., 2004; Peacock et al., 2005; Rosas et al., 2016]. In recent years, 3D kinematic-dynamic models of subduction zones have become more common. Some studies used generic models to examine the relationship between the geometry of the subducting plate, along-strike mantle flow and the thermal structure [Kneller and van Keken, 2008; Bengtson and van Keken, 2012]. 3D models tailored to the subduction zones of the Marianas and the Andes [Kneller and van Keken, 2007], Japan [Morishige, 2015; Wada et al., 2015] and Central America [Rosas et al., 2016] have also been developed. Along-strike flow in subduction zones is inferred by the splitting or birefringence of shear waves, which indicates olivine minerals in the mantle are seismically anisotropic [Long and Silver, 2008; Long and Wirth, 2013]. The direction of fastest propagation (or a-axis) indicates the direction of maximum deformation of mantle minerals, as well as showing a good correlation with the flow direction [McKenzie, 1979; Fischer et al.,

2000; Park and Levin, 2002; Becker et al., 2003; Conrad et al., 2007]. Near subduction zones, anisotropy studies consistently reveal an a-axis that departs from the expected trench-perpendicular orientation inferred from plate motions, indicating the flow field from the mantle wedge has a complex 3D pattern [Nakajima et al., 2006; Long and Silver, 2008; Hoernle et al., 2008; Abt et al., 2009]. Additionally, the magnitude and direction of the flow can also be constrained by geochemical studies of arc magmas [Herrstrom et al., 1995; Johnston and Thorkelson, 1997; Abratis and Worner, 2001; Ferrari et al., 2001; Hoernle et al., 2008].

The Mexican subduction zone is a region for which shear-wave splitting studies suggest along-strike mantle flow [Soto et al., 2009; Stubailo et al., 2012; Bernal-López et al., 2015]. At the Mexican subduction zone, the Cocos plate and Rivera microplate subduct beneath the North American plate along the Middle America Trench (MAT) (Figure 6.1). The Rivera and Cocos plate are two of the remaining fragments of the Farallon plate that resulted from the interaction of the Farallon spreading center with the North American plate, approximately 23 Myr ago [Atwater, 1970; Mammerickx and Klitgord, 1982; DeMets and Traylen, 2000; Barckhausen et al., 2008]. The Rivera plate subducts beneath the westernmost side of the MAT. Further west, the boundary between the Rivera and Cocos plate lies along the El Gordo graben, a 40-50 km-wide region currently undergoing extension [Bandy et al., 1995, 2000; Serrato-Díaz et al., 2004; Gaviria et al., 2013].

In the last decade, seismic data provided by the MARS (MApping the Rivera Subduction zone), the MASE (Meso-American Subduction Experiment), and the VEOX (Veracruz-Oaxaca subduction experiment) arrays have provided contraints on the structure of the Cocos plate [Pérez-Campos et al., 2008; Yang et al., 2009; Kim et al., 2010]. The data collected from these networks has also helped to create an anisotropy map throughout southern Mexico [Soto et al., 2009; Stubailo et al., 2012; Bernal-López

et al., 2015].

On the westernmost side of the MAT, the Rivera plate dips at an angle of 60° -70° [Pardo and Suárez, 1995; Yang et al., 2009]. *P*-wave tomography studies by Yang et al. [2009] show a continuous, east-to-west, high-velocity seismic structure across the Rivera-Cocos boundary that extends to a depth of ∼150 km. At larger depths, a discontinuity in this structure is interpreted as a gap separating both plates. Shear-wave splitting studies in the area show *a*-axis in the mantle wedge that are mostly aligned with the trench along much of the Rivera plate, but significantly rotate towards a more trench-perpendicular orientation near the Rivera-Cocos boundary [Soto et al., 2009; Stubailo et al., 2012]. This suggests the gap observed by Yang et al. [2009] serves as a pathway for asthenospheric mantle to flow from behind the slab in a toroidal pattern. A similar interpretation was given to the rotation of fast directions in the western U.S. along the edge of the subducted Gorda-Juan de Fuca plate [Zandt and Humphreys, 2008]. Toroidal flow around the Rivera plate edge was first proposed by Ferrari et al. [2001] in order to explain the presence of intraplate lavas, mostly in the form of oceanic-island basalt (IOB). Laboratory models have also reproduced this toroidal flow around the Rivera plate [Neumann et al., 2015].

East of the Rivera-Cocos boundary, the slab dip gradually reduces at a depth of 40 km, with the slab eventually becoming flat [Pardo and Suárez, 1995; Pérez-Campos et al., 2008; Kim et al., 2010]. Such complex geometry for the Cocos plate results in an oblique volcanic arc, the Trans-Mexican Volcanic Belt (TMVB), which contrasts with the trench-parallel arc observed along the MAT in Central America [Carr et al., 2003; Ferrari et al., 2012]. The detailed structure of the Cocos plate in this region has been particularly difficult to investigate due to the lack of seismicity at depths larger than 100 km, with most of the earthquakes located near the coast [Pardo and Suárez, 1995]. Using data from the MASE array, receiver function imaging estimated a dip

of 15° for the Cocos plate near the coast, a flat slab that underplates the overriding North American plate at a depth of 40-60 km for a distance of ∼250 km landward of the trench, and then a slab with an approximate dip of 75° [Kim et al., 2010, 2012] (Figure 6.1). Flat-slabs occur in approximately 10% of modern subduction zones [van Hunen et al., 2004], and they are commonly associated with subduction of young (buoyant) slabs and oceanic ridges, as well as increased seismic activity in the upper plate resulting from the coupling between slab and upper plate [Gutscher et al., 2000; Gutscher, 2002]. For the case of central Mexico, slab-flattening is associated with neither ridge subduction nor with a buoyant slab [Skinner and Clayton, 2011]. The current understanding of flat-slab subduction in Mexico invokes trench rollback, which favours a shallower dip for the slab due to an increase in the suction force within the wedge [Manea and Gurnis, 2007; Manea et al., 2012], combined with sudden increases in subducting plate velocities in mid-to-late Miocene [Manea et al., 2013].

Anisotropy based on Rayleigh-wave phase velocity dispersion show a predominantly trench-perpendicular orientation for the *a*-axis in the mantle wedge adjacent to the flat-slab [Stubailo et al., 2012]. A similar result was obtained by Bernal-López et al. [2015] using *SKS* and *SKKS* waves recorded by MASE. In the transition between the flat-slab and the normal-dipping section of the plate, Stubailo et al. [2012] observed a rotation of *a*-axis from a trench-perpendicular to an east-trending orientation. The location of the rotation coincides with the landward projection of the Orozco fracture zone (OFZ) (Figure 6.2). Dougherty et al. [2012] argues the OFZ serves as an structural boundary dividing two sections of the Cocos plate, as indicated by a significant change in intraslab seismicity and slab dehydration across the fracture.

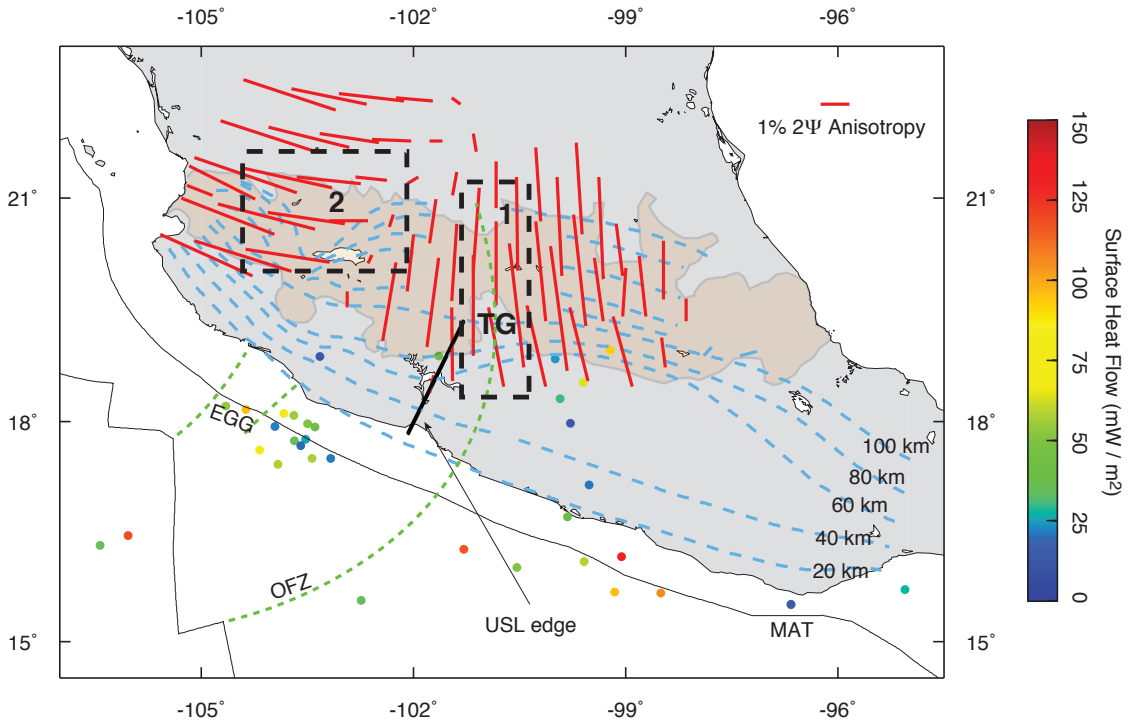

Figure 6.2 Some geophysical observations in the Mexican subduction zone. Black lines are tectonic boundaries between plates. Light orange shows approximate location of the TMBV (Middle Miocene to Holocene volcanism), as shown by Ferrari et al. [2012]. Green dashed line near the Rivera-Cocos boundary encloses the El Gordo grabben (EGG); to the east, the Orozco fracture zone (OFZ) and its landward projection to the Tzitzio gap (TG) are also shown. Coloured dots are heat flux measurements [Ziagos et al., 1985; Prol-Ledesma et al., 1989]. Thick black line represents the western end of the ultra-slow velocity layer (USL) [Dougherty et al., 2012]. Red lines are the fast directions for the mantle at a depth of 100 km [Stubailo et al., 2012]. Light blue dashed lines are depth contours. Thick dashed lines are the proposed tear that divides the normal-dipping and flat-slab sections of the Cocos plate (1), and the location of the Rivera-Cocos gap (2).

Detailed imaging of the Cocos plate in the transition between the flat-slab and normal dipping sections is difficult due to a very shallow seismicity in the area, with a Wadati-Benioff zone that does not exceed 100 km depth, and poor spatial coverage of the MARS and MASE arrays in the region. However, two main models for the geometry of the slab are possible:

1. Given the structural boundary the OFZ represents and the rotation of the a-axis in the mantle wedge above it, Stubailo et al. [2012] suggested the landward projection of the OFZ corresponds to a tear that cuts the Cocos plate, separating the flat-slab section from the normal-dipping section. The tear would be an analogous to the Rivera-Cocos boundary, allowing asthenospheric mantle to flow into the wedge in a toroidal pattern.

2. A second hypothesis to explain the rotation of the a-axis would be to have a continuous slab across the fracture, under which along-strike flow would be generated by the extreme changes in the angle of subduction observed in central Mexico.

In this study, we present the first three-dimensional, steady-state thermal model of the Mexican subduction zone. Our objective is to study three-dimensional mantle wedge motions and its effects on the thermal structure. Previous 2D thermal studies of the Mexican subduction zone have concentrated on the shallow thermal structure of the slab, either to investigate slab metamorphism, the megathrust seismogenic zone or the role of hydrothermal circulation on slab temperatures [Currie et al., 2002; Manea et al., 2004, 2005; Manea and Manea, 2011] but these studies do not address mantle wedge flow in detail.

For the model presented here, we assume the slab is a continous feature. In particular, we are interested in the transition between the flat-slab section and the

normal-dipping section, where the along-strike variations in the geometry of the Cocos plate may induce a significant along-strike flow. Previous 3D thermal studies have shown a mantle wedge that flows from steep dip to shallow dip [Kneller and van Keken, 2008; Bengtson and van Keken, 2012; Wada et al., 2015; Rosas et al., 2016]. The anisotropy pattern given by Stubailo et al. [2012] shows an east-trending orientation for the a-axis, suggesting the mantle flows from steep to shallow dip as well. By comparing our wedge flow with the seismic anisotropy pattern, our model will allow us to infer whether the Cocos plate is fragmented in central Mexico or not.

6.2 Model Description

Our modeling area in the Mexican subduction zone extends from the southern state of Oaxaca to the westernmost section of the Cocos plate, near the state of Jalisco (black box in Figure 6.1). We do not include the gap between the Cocos and the Rivera plate. The geometry of the slab was obtained from the information gathered by the MARS, MASE and VEOX deployments [Ferrari et al., 2012]. A cartesian coordinate frame is defined so that the x-axis runs approximately parallel to the strike of the trench, the y-axis runs in the landward direction, and the z-axis is the depth. The approximate along-strike distance for our model is 642 km, and it includes most of the flat slab section, as well as the transition to a normal dipping plate. The side boundaries are aligned with the y-axis. The oceanic (seaward) boundary of our model corresponds to the trench. The maximum depth of the top of the slab is 300 km, which places the entire mantle wedge in the upper mantle. Due to changes in the angle of subduction of the Cocos plate, the backarc (landward) boundary of our model is thus located at a variable distance from the trench.

Our model uses a steady-state, kinematic-dynamic approach, with fixed geome-

tries for the upper and lower plates, and a mantle wedge that flows dynamically due to viscous coupling with the downgoing slab. The advantage of this type of model is that it allows for a greater resolution of the thermal structure compared to a completely dynamic model [Billen, 2008]. The disadvantage is that we neglect for any dynamic factors affecting the slab, such as slab rollback or retreat/advance. We use the finite-element code PGCtherm3D. This code is the three-dimensional version of PGCtherm2D, a subduction modeling code that has been used in many studies [Currie et al., 2002, 2004; Wada et al., 2008; Wada and Wang, 2009; Wada et al., 2011; Wang et al., 2015; Völker and Stipp, 2015] and has been benchmarked [van Keken et al., 2008]. The code solves the equations of conservation of mass, momentum and energy. In that order, the equations are:

$$\nabla \cdot \mathbf{u} = 0 \ , \tag{6.1}$$

$$\nabla P - \nabla \cdot (2\eta \dot{\boldsymbol{\epsilon}}) = 0 \ , \tag{6.2}$$

$$\mathbf{u} \cdot \nabla T = -\frac{k}{\rho c_p} \nabla^2 T + \frac{A}{\rho c_p} \ , \tag{6.3}$$

where $\mathbf{u}$ is the velocity, P is the dynamic pressure, η is the dynamic viscosity, $\dot{\boldsymbol{\epsilon}}$ is the strain-rate tensor, T is the temperature, k is the thermal conductivity, ρ is the density, A is the radiogenic heat production, and c_p is the specific heat. In equations 6.1-6.3, the mantle is assumed to be an incompressible, infinite Prandtl number fluid driven by viscous coupling with the downgoing slab and along-strike pressure gradients.

The model is divided into 3 main units, namely the upper plate, the subducting slab and the mantle wedge (Figure 6.3a). For the upper plate, the continental Moho is fixed at a depth of 40 km, and underlain by a 5 km-thick lithospheric mantle. This Moho depth is in agreement with results from the MASE, MARS and VEOX deploy-

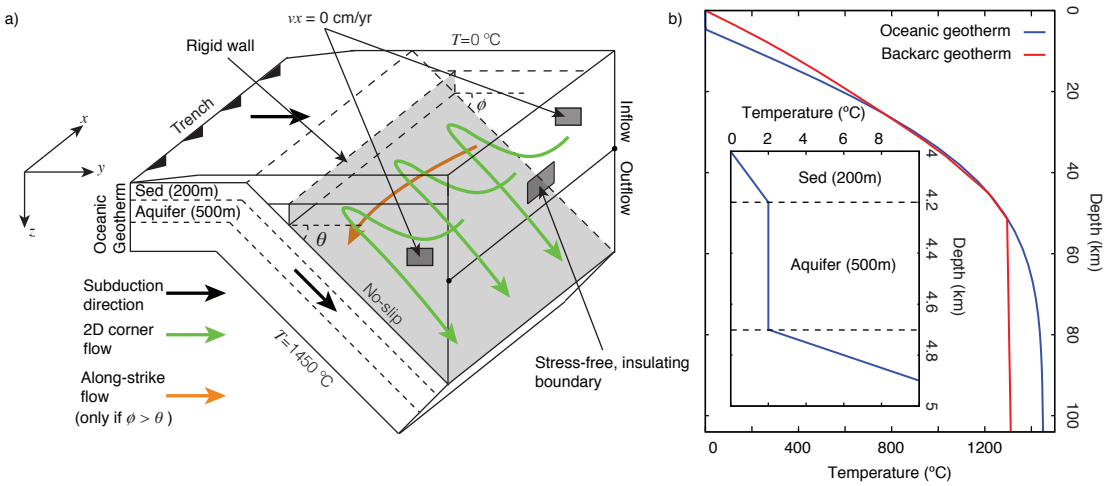

Figure 6.3 **a**: General 3D model setup with main units and boundary conditions. Thicknesses of sediment layer (sed) and basement aquifer are shown. 2D corner flow and along-strike flow in the mantle wedge are denoted by green and yellow arrows, respectively. Inflow and outflow transition point on the backarc boundary is also shown. **b**: Modified oceanic geotherm for a 15 Myr-old slab (blue) and backarc (red) geotherms. The inset shows the oceanic geotherm at shallow depths, with sediments and aquifer shown. A cold thermal gradient is imposed near the surface to reproduce the low surface heat flow observed near the trench. Complete oceanic geotherm is composed of multiple 2D geotherms at each location in the trench for different ages, with the same shallow thermal structure (sediments and aquifer).

ments [Ferrari et al., 2012], as well with as previous modeling studies [Currie et al., 2002; Manea et al., 2004; Manea and Manea, 2011]. The subducting slab includes a sediment layer and the oceanic crust, followed by the oceanic mantle lithosphere and an entrained layer of mantle below the plate. The sediment layer is 200 m-thick. The uppermost section of the oceanic crust is the subducting aquifer, a high permeability ($10^{-12} - 10^{-15}$ m^2 layer 500 m thick [Fisher, 1998] overlain by the impermeable sediments. To create the finite-element mesh, each domain is subdivided into isoparametric finite elements whose size range between a few kilometers in the upper crust and lower part of the slab, to a few hundred meters near the mantle wedge corner. The along-strike width of each element is fixed at 2.8 km for the entire model.

The thermal properties for each element according to their unit are shown in Table 6.2. A temperature of 0°C and 1450°C is imposed on the surface and bottom of the model, respectively. As we are only interested in the effect of along-strike mantle flow, we neglect the effects of frictional heating along the subduction interface. On the backarc boundary, we use an conductive equilibrium geotherm for the upper part of the model that gives a surface heat flow of 90 mW/m^2, consistent with what has been observed for most backarcs [Currie and Hyndman, 2006]. The conductive geotherm intersects a mantle adiabat with a potential temperature of 1295 °C at a depth of ∼50 km. For the oceanic boundary condition, we employ a GDH1 geotherm that uses the age of the plate at each point along the trench [Stein and Stein, 1992]. The age of the Cocos plate is shown in Figure 6.1 [Ferrari et al., 2012]. We identify three age domains: (1) a steadily-decreasing age from 17 Myr at the east boundary of our model to 14.5 Myr near the OFZ, (2) a discontinuous increase in age across the OFZ from 14.5 Myr to 17.6 Myr, and (3) a decrease from 17.6 Myr to 11 Myr on the west boundary, near the Rivera-Cocos gap. Surface heat flow near the MAT can be as low as ∼15mW/m^2 [Ziagos et al., 1985; Prol-Ledesma et al., 1989], indicating the possible presence of hydrothermal circulation in the subducting aquifer. Hydrothermal circulation refers to vigorous convection of aqueous fluids, which can significantly affect slab temperatures [Spinelli and Wang, 2009; Harris et al., 2010b; Cozzens and Spinelli, 2012]. In order to match the observed low surface heat flow, we impose a cold thermal gradient of 10 km/°C along the sediment layer, and a constant temperature throughout the aquifer to include the effects of hydrothermal circulation that simulates the thermal effect of rapid fluid flow (Figure 6.3b). This approach has been used by several studies intended to model the effect of hydrothermal circulation on slab temperatures[Langseth and Silver, 1996; Harris and Wang, 2002; Rosas et al., 2016]. No velocity is assigned for the top of the model (surface), whereas a velocity

Table 6.1 Thermal properties for 3D model of the Mexican subduction zone.

Subdomain	A (μW/m^3)	k (W/m K)	$C = \rho c_p$ (MJ/K m^3)
Upper Crust (15 km)	1.3	2.5	2.5
Lower Crust (25 km)	0.25	2.5	2.5
Oceanic Slab (100 km)	0.02	2.5	3.3
Sediment Layer (200 m)	1.0	1.0	2.5
Mantle Wedge	0.02	3.1	3.3

equal to the convergence rate is assigned to the bottom. No-flow ($v_x = 0$ cm/yr) and insulating boundary conditions are employed along the side boundaries. Previous studies show the side-boundary conditions are expected to affect modeling results only within the 100-150 km closest to the boundaries, and only if there are significant changes in the along-strike geometry of the plate near them [Wada et al., 2015; Rosas et al., 2016]. A no-slip condition is imposed along the interface between the slab and the mantle wedge, whereas a zero-velocity is imposed to the mantle along the continental Moho. The slab convergence rate throughout our model is fixed at 6 cm/yr, consistent with the average convergence rate for the region [DeMets and Traylen, 2000]. The direction of convergence is parallel to the side boundaries. For the backarc boundary, we employ stress-free boundary conditions, with the transition between inflow and outflow determined dynamically (Figure 6.3).

A rigid boundary is placed near the wedge corner to prevent the mantle from flowing into it. The boundary is located at a point in which the slab reaches a depth of 70 km, and it extends vertically to the continental Moho. This depth is consistent with the transition from low surface heat flow in the forearc to high values in the arc region [Wada and Wang, 2009]. The low heat flow observed in the forearc is consistent with serpentinization of the forearc mantle, which results in a decoupling between the wedge and the slab and prevents the mantle from flowing into the wedge

corner [Wada et al., 2008].

Mantle flow by dislocation creep results in LPO anisotropy of olivine minerals, which has been observed through shear-wave splitting studies in the mantle wedge of subduction zones [Long and Silver, 2008; Long and Wirth, 2013]. We thus employe a dislocation creep rheology for the mantle, with an effective viscosity given by

$$\eta = (BC_{\mathrm{OH}}^{r})^{-\frac{1}{n}} \dot{\epsilon}^{\frac{1-n}{n}} \exp\Big(\frac{E}{nRT}\Big) \ , \tag{6.4}$$

where $B = 3.0 \times 10^{-20}$ Pa^{-n} s^{-1} is the pre-exponential factor, C_{OH} is the water content in the mantle wedge, $r = 1.2$ is the water exponent, $\dot{\epsilon}$ is the second invariant of the strain-rate tensor, $n = 3.5$ is the power-law exponent, $E = 480$ kJ/mol is the activation energy, and $R = 8.314$ J/mol K is the universal gas constant [Hirth and Kohlstedt, 2003]. Seismic studies for Central Mexico show a attenuation quality factor of $Q_s = 150 - 500$ for the mantle wedge [Chen and Clayton, 2009]. In contrast, a $Q_s = 38 - 84$ is observed in the southern section of the MAT below Nicaragua and Costa Rica [Rychert et al., 2008]. The large attenuation observed in Central America is due to the larger amounts of water transported down by the Cocos plate [Abers et al., 2003; Ivandic et al., 2010; Van Avendonk et al., 2011], which are later released into the mantle wedge [Dinc et al., 2011]. Assuming mantle attenuation is controlled by its temperature and water content, a higher Q_s (lower attenuation) suggest the mantle wedge of Mexico is not as hydrated as in Central America. We thus use a water content of $C_{\mathrm{OH}} = 1000$ H/10^6 Si, a value that has been used for a moderately hydrated mantle in other studies [Behn et al., 2009; Goes et al., 2012].

6.3 Results

Figure 6.4 shows the streamlines for the mantle wedge below Mexico. Coupling between the downgoing plate and the mantle carries mantle material downward, and new material from the backarc is being pulled into the corner to replenish the lost mantle. The flow also moves laterally in response to along-strike pressure gradients resulting from changes in the angle of subduction.

6.3.1 Three-dimensional flow field

Figure 6.4a shows the streamlines from a lateral point of view with a slight elevation. Overall, the mantle maintains a predominately 2D corner flow pattern throughout the entire modeling region. The flow, however, is not entirely two-dimensional. Regional variations in the angle of subduction leads to some of the flow being driven laterally. The along-strike flow goes from the normal-dipping section of the plate to the flat-slab section (east to west). This is in agreement with previous 3D studies of wedge flow, in which the mantle is observed to flow from steep-dip regions to shallow-dip regions due to changes in the size of the low-pressure area of the wedge corner [Kneller and van Keken, 2008; Rosas et al., 2016].

The magnitude of the along-strike flow is not uniform throughout the model. Figure 6.4b shows a top-view of the mantle streamlines down to a depth of 120 km. Mantle above this point is predominately incoming flow from the backarc. This inflow is important because its driven by pressure gradients, as opposed to the return flow or outflow, which is driven by the no-slip condition in the slab-mantle interface and thus follows the direction of convergence. The magnitude of the along-strike flow is in the range 0-3.6 cm/yr along the entire width of our model (range shown in Figure 6.4 is up to 3.15 cm/yr). Most of the along-strike flow occurs on the western side of

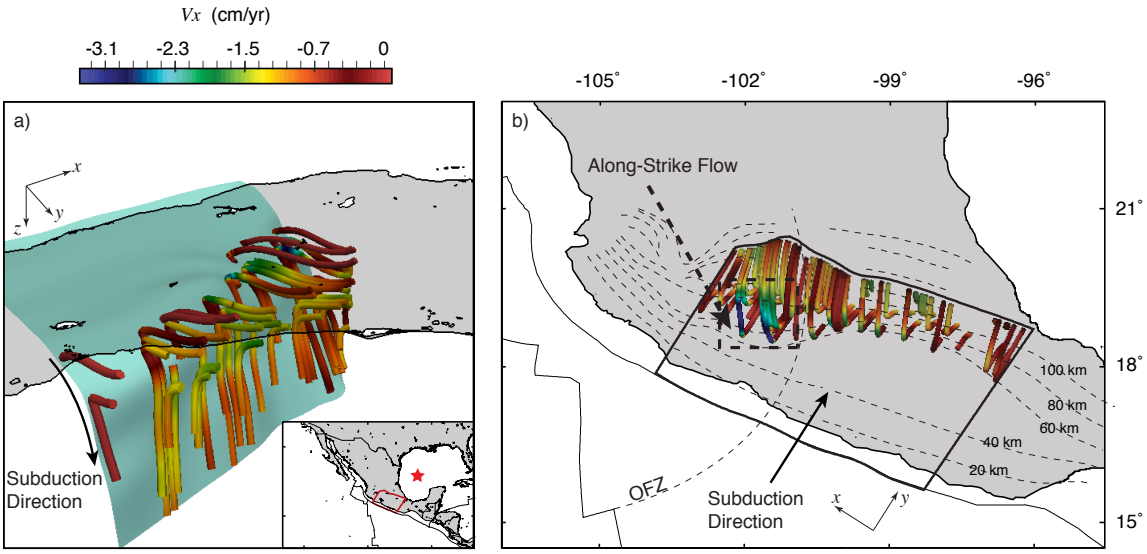

Figure 6.4 Mantle streamlines for the mantle wedge of the Mexican subduction zone. Color scale denotes along-strike (v_x) flow component. Solid black arrow shows subduction direction. **a**: Three-dimensional view of the mantle. The surface of the subducting Cocos plate is shown in cyan. Insets show the approximate point of view (red star). Red box is the modeling area. **b**: Top view of the mantle. Thin dashed lines are depth contours of the slab surface. Orozco fracture zone (OFZ) is also shown. Dashed black arrow and box shows region of strong along-strike flow.

the OFZ, corresponding to the largest along-strike change in slab dip. The 3.6 cm/yr observed in this region accounts for 60% of the magnitude of the convergence rate (6 cm/yr). Relative to the convergence rate, this magnitude is higher than the 40% observed for the southern section of the MAT, in Costa Rica-Nicaragua, where the dip of the Cocos plate changes from 70° to 45° over a distance of 200-250 km [Rosas et al., 2016]. We attribute this higher magnitude to the larger dip change experienced in Mexico form (∼45°C to flat-slab) over a distance of 200-250 km.

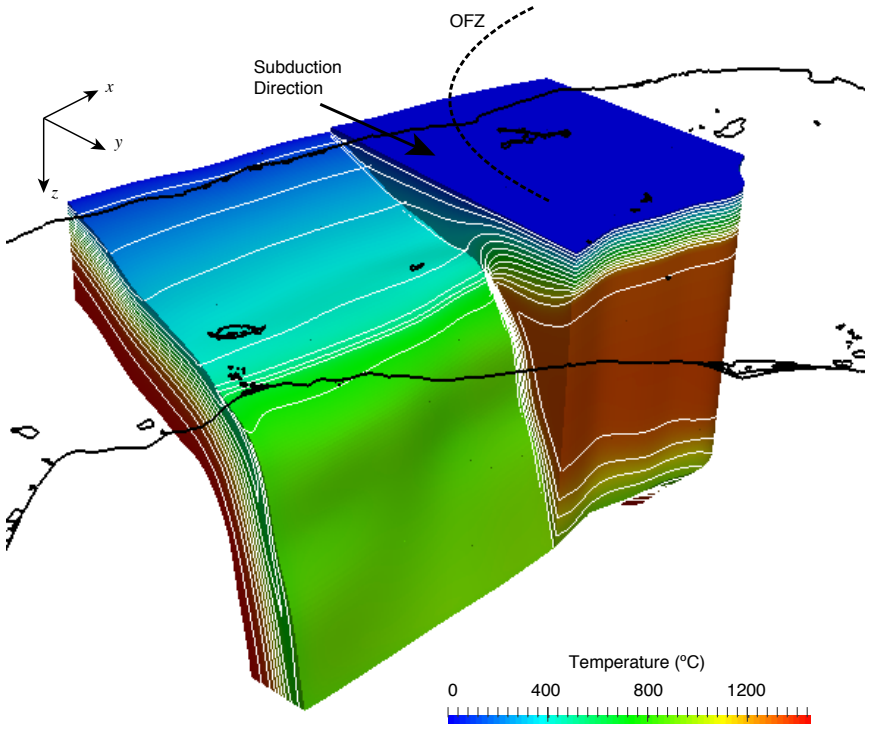

Figure 6.5 3D thermal structure of the Mexican subduction zone. Point of view is similar as in Figure 6.4. Model is cut in the middle to show thermal structure of the slab, mantle wedge and upper plate. White lines are Isotherms with a 100°C spacing. Subduction direction is shown with a black arrow. Dashed black line is the approximate location of the Orozco fracture zone (OFZ) and its landward projection.

6.3.2 Thermal structure and comparison to two-dimensional models

The 3D thermal structure of the Mexican subduction zone is shown in Figure 6.5. The thermal structure shows similar features to those observed in 2D models [Peacock, 1996; van Keken et al., 2002], such as a depression of the isotherms as the slab subducts, and an increase in mantle wedge temperatures to 1000-1250°C below the volcanic arc.

Figure 6.6a shows the thermal structure of the surface of the Cocos plate. The thermal structure shows a complex 3D structure due changes in the age of the slab at the trench and along-strike mantle flow. In particular, we note the age offset near the OFZ displaces the isotherms in the landward direction. The disturbance propagates downdip as the slab subducts, and continues even after the slab enters the mantle wedge. Below the Tiztzio gap, the 800°C and 900°C isotherms are displaced by 30-40 km and 70-80 km, respectively, at a depth of 100-150 km.

To better visualize the thermal structure in the wedge and how it is affected by the along-strike flow, Figures 6.6b-6.6d show the along-strike flow component, the thermal structure extracted from two profiles through the 3D model, and the temperature difference with respect to 2D models. The temperature difference is used to assess the effect of along-strike flow on the thermal structure. The 2D models are created using the plate geometry extrated from our 3D model at specific cross-sections. PGCtherm3D is used to generate the 2D models, and they employ similar boundary conditions and thermal properties as the 3D model. 2D models have a constant along-strike geometry and a width of only 200 m (i.e., they have a 2D structure). The location of the cross-sections is shown in Figure 6.6a. Cross-section AA' is located in the flat-slab section, 200 km away from the eastern boundary of the 3D model, whereas cross-section BB' is located in the curved section of the slab, 150 km away from the western boundary.

For cross-section AA', the along-strike flow occurs throughout the mantle wedge, with its maximum magnitude never exceeding ∼1.5 cm/yr (Figure 6.6b). The thermal structure of the wedge (Figure 6.6c) is not significantly affected by this flow, with a maximum thermal change of less than 20°C between the 3D and 2D models (Figure 6.6d). This indicates that 2D corner flow models adequately capture the dynamics of the wedge in this region.

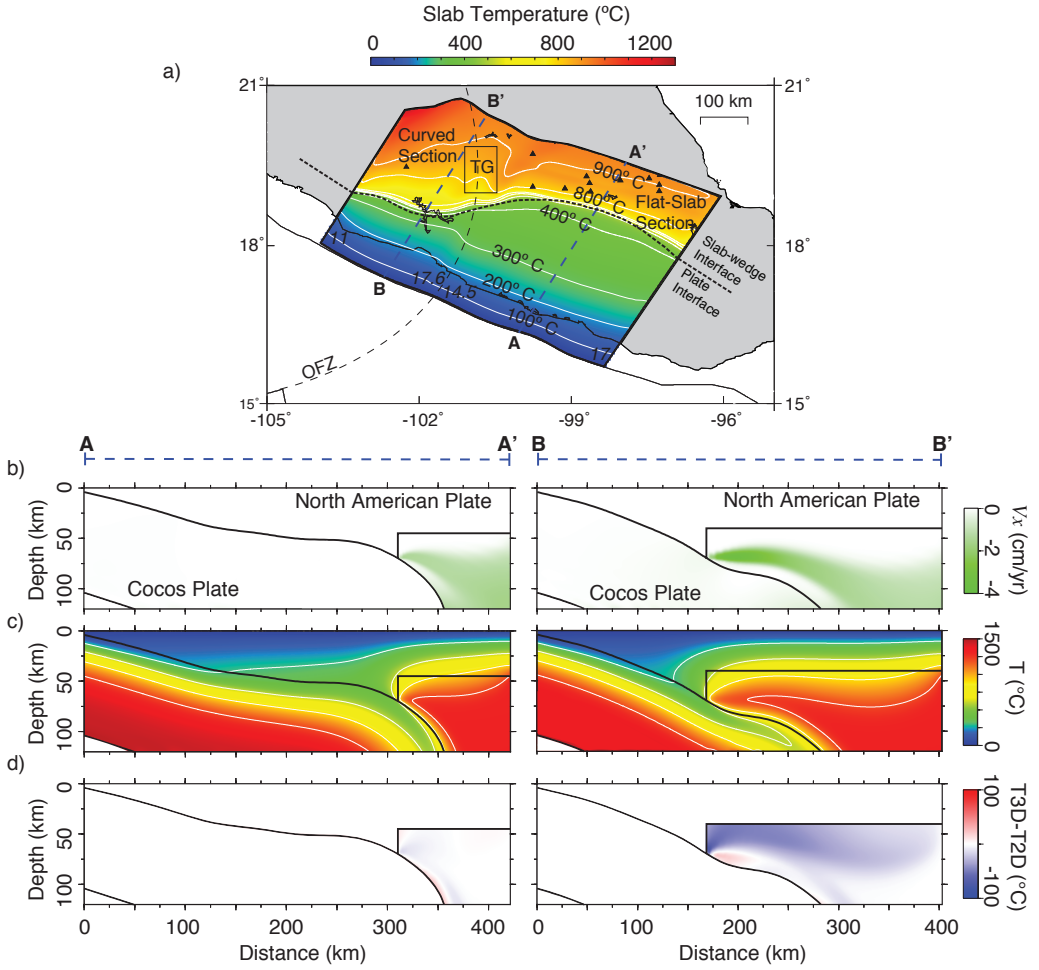

Figure 6.6 **a**: Slab temperatures obtained from 3D model, with isotherms with a 100°C spacing shown. Location of cross-sections AA' and BB' (dashed blue lines) and approximate location of the Tzitzio gap (TG) (black rectangle) is shown. Cross-section AA' is located in the flat-slab section, whereas cross-section BB' is in the curved section of the slab. Dotted black line represents the point of transition between upper-lower plate interface and slab-mantle interface, located a depth of ∼70 km. **b**: Along-strike flow component. **c**: 3D thermal structure extracted at cross-section locations. Isotherms with a 300°C spacing are shown. **d**: Thermal difference between 3D and 2D model for cross-sections AA' and BB'.

For cross-section BB', the along-strike flow has a maximum magnitude of ∼3.5 cm/yr, and is not as dispersed near the wedge corner as for cross-section AA'. The along-strike flow is focalized through a narrow channel (approx. 100 km in length) that extends from the tip of the wedge corner to a distance of 300-325 km from the trench. Contrary to cross-section AA', the along-strike flow has a significant impact on the thermal structure, with temperatures changing as much as 75°C in the mantle wedge. The 3D model is colder than the 2D model, similar to what was obtained for Japan [Wada et al., 2015], but different to the results for Central America [Rosas et al., 2016], where the 3D model was shown to be hotter. A change of 75°C can affect the melting point of the mantle wedge which, depending on the amount of water released by the slab, requires temperatures of 1000-1300°C [Schmidt and Poli, 1998]. Models investigating the thermal structure of the mantle wedge near the transition to a flat-slab are thus required to incorporate 3D effects, as 2D models do not incorporate along-strike flow.

6.4 Mantle Flow and Anisotropy

Olivine minerals in the mantle flowing through a dislocation creep rheology exhibit lattice-preferred orientation (LPO) anisotropy. LPO anisotropy in geodynamic models is usually investigated by calculating the deformation of fluid elements in the mantle, with the direction of maximum stretching taken to be the a-axis. Laboratory experiments have shown that this is the case at shear-stresses of ∼100-300 MPa and a water content of less than 200 ppm H/Si [Zhang and Karato, 1995; Karato et al., 2008]. Numerical modeling of mantle flow in subduction zones have shown a clear relationshop between stretching directions and the a-axis as well [Kneller and van Keken, 2008; Faccenda and Capitanio, 2013; Li et al., 2014].

For this study, we assume the mantle flows in the direction of the a-axis, an assumption that has been made in other studies of mantle wedge flow [Kneller and van Keken, 2007; Wada et al., 2015]. To compare the 3D flow field and the anisotropy pattern, Figure 6.7 shows the mantle inflow from our 3D model and the a-axis in the mantle wedge at a depth of 100 km [Stubailo et al., 2012]. The a-axis show a predominantly trench-perpendicular orientation inside our modeling region, with a slight eastward rotation in central Mexico that coincides with the change from normal-dipping to flat-slab subduction. To the west of our modeling area, the a-axis abruptly rotate, likely due to toroidal mantle motions flowing through the gap between the Rivera-Cocos gap. The flow field from our 3D model is consistent with the anisotropy pattern throughout the modeling area, with the a-axis rotating slightly near the curved section of the slab. This suggests the corner flow of the wedge controls mantle motions in this area, as opposed to the region near the Rivera-Cocos gap, where asthenospheric mantle from behind the slab infiltrates the wedge.

6.5 Discussion

The flow field shown in Figures 6.4 and 6.6b can be used to infer the structure of the subducted Cocos plate. As discussed previously, Stubailo et al. [2012] proposed a slab tear along the OFZ to explain the rotation of the a-axis in central Mexico. Our 3D model does not incorporate the tear proposed by Stubailo et al. [2012], but rather employs a continous slab that connects the flat-slab section with the western section of the Cocos plate. The along-strike flow is induced by this change in the angle of subduction (Subsection 6.3.1).

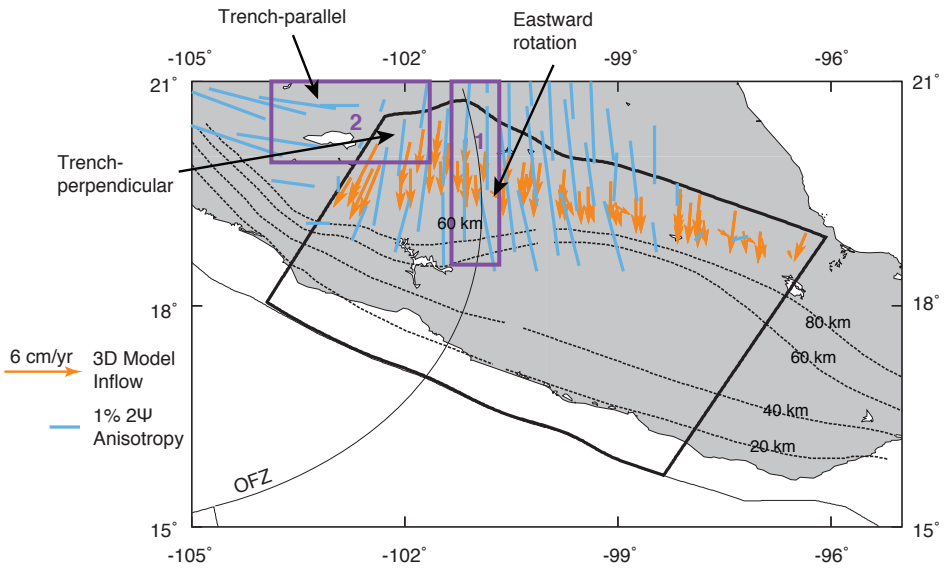

Figure 6.7 Horizontal velocity field as obtained from 3D model (orange) and a-axis as obtained from Stubailo et al. [2012] at a depth of 100 km. Thin dashed lines are depth contours of the slab. Projection of Orozco fracture zone is observed. Purple lines are locations the proposed tear in the Cocos plate (Region 1) and the Rivera-Cocos gap (Region 2).

6.5.1 Is the Cocos plate fragmented along the OFZ?

The comparison between 3D wedge flow and anisotropy shown in Figure 6.7 can help us to infer the structure of the Cocos plate. Two regions of interest are shown in Figure 6.7. Region 1 is located in the vicinity of the landward projection of the OFZ, whereas Region 2 is located near the Rivera-Cocos boundary. Although our 3D model does not extend to Region 2, the differences in their respective anisotropy patterns can be useful when inferring the structure of the subducted Cocos plate.

In Region 1, there is a small rotation of the a-axis with respect to the trench. We note the rotation is directed in the eastward orientation and slightly increases as we approach the slab, similar to the flow direction from our model. The Outside Region 1, in the mantle adjacent to the flat-slab section, a slightly-rotated orientation of the a-axis is observed, but the flow appears to be consistent by typical 2D corner flow, in

agreement with other anisotropy studies in the region [Bernal-López et al., 2015].

Compared to Region 1, the a-axis in Region 2 show a very abrupt change in their orientation, from trench-perpendicular on its eastern side to trench-parallel on the west above the Rivera plate. Given that there are no significant changes in the dip between the Cocos and Rivera plate in this area, and in light of the gap observed by Yang et al. [2009], the abruptness of the transition in the a-axis orientation suggests the flow of the mantle in Region 2 is driven by a different mechanism than for Region 1. Whereas for Region 1 the a-axis follow a slight eastward rotation that is consistent with along-strike mantle flow induced by changes in the angle of subduction, the change in the a-axis in Region 2 is consistent with the description of Ferrari et al. [2001] and Soto et al. [2009], in which the mantle flows toroidally around the Rivera plate in response to the rollback of the slab.

In general, the a-axis obtained by Stubailo et al. [2012] are consistent with our predicted mantle flow in the curved section of the slab. As our model employs a continous slab rather than a fragmented one, this suggests that a tear along the OFZ is not needed to explain the anisotropy pattern, and in fact the slab could be continous in this region.

6.5.2 Tzitzio Gap and termination of the Ultra-Slow Velocity Layer

A tear in the Cocos plate along the path of the OFZ could explain the presence of a prominent indentation in the TMVB, known as the Tzitzio gap (Figure 6.2), in which quaternary volcanism is displaced ∼100 km landward from the volcanic front [Blatter and Hammersley, 2010]. The Tzitzio gap would result from the absence of subducted material in this region and hence the absence of volcanism [Stubailo et al., 2012].

The termination of an ultra-slow velocity layer (USL) observed along the surface of the Cocos plate on its eastern side would support this hypothesis [Song et al., 2009; Dougherty et al., 2012]. The USL has been proposed to be a fluid-saturated section of the oceanic crust [Song et al., 2009], or a mantle wedge remnant that experienced significant serpentinization as the slab flattened [Manea et al., 2013]. Figure 6.2 shows the proposed termination point for the USL [Dougherty et al., 2012].

Given our results regarding the mantle flow and thermal structure, we note two important points with respect to the origin of the Tzitzio gap and the termination ot the USL:

1. As discussed in Section 6.3, the age offset in the Cocos plate across the OFZ results in a thermal disturbance that is carried down as the plate subducts. In the mantle wedge, the disturbance results in a shift of the isotherms in the slab, with a seaward displacement of 60-70 km in the 900°C isotherm in Figure 6.6a near the downward projection of the Tzitzio gap. To the east of the Tzitzio gap, we note the landward distance between the 800-900°C isotherms is 40-50 km. The 800-900°C isotherm transition is located at a depth of 80-110 km in this area (not shown in Figure 6.6a). This is contrary to what is observed near or at the Tzitzio gap, where the landward distance of the 800-900°C isotherm transition increases to ∼100 km, with the 900°C isotherm located at a depth of ∼150 km. The downdip push of the isotherms suggests that any water stored in the slab can be transported to larger depths, pushing the volcanic arc landward and thus creating the Tzitzio gap.

   The geochemistry around the Tzitzio gap supports our interpretation of its origin. The geochemical evidence of mantle infiltration from around the slab and into the mantle wedge along the MAT comes from the presence of magmas

with an oceanic-island basalt (OIB) composition [Herrstrom et al., 1995; Ferrari et al., 2001; Hoernle et al., 2008]. OIB magmas are found throughout the TMVB, probably due to mantle flowing through a west-east propagating tear in the slab at depths ∼500 km [Ferrari, 2004; Pérez-Campos et al., 2008]. A higher concentration of OIB magmas (∼5% of total volcanic output) is found near the western TMVB [Ferrari et al., 2001], consistent with the toroidal mantle that flows through the Rivera-Cocos gap Soto et al. [2009]. Near the proposed tear along the OFZ, however, no significant signal of OIB magmas is observed [Gómez-Tuena et al., 2007]. Furthermore,, we note the presence of arc magmas that show an anomalously high signal of hydrous fluids from the slab in the north end of the Tzitzio gap [Blatter and Hammersley, 2010], indicating that the slab could be continuous across the OFZ.

2. Although there is in fact a termination of the USL on the eastern side of the OFZ [Dougherty et al., 2012], in our view, this does not imply the Cocos plate is fragmented along the fracture. The USL represents the fluid-saturated portion of the upper oceanic crust [Song et al., 2009], and as such is controlled by the thermal state of the plate [Manea and Manea, 2011]. Although the slab temperatures presented in Figure 6.6a do not show significant changes on the eastern side of the OFZ and thus do not permit us to infer the origin of the USL, we recognize that our models do not fully include the effect of hydrothermal circulation, as we only incorporate it through a modified oceanic geotherm (Section 6.2) and not through conductivity proxies in the aquifer that mimic convective heat transport [Davis et al., 1997; Wang, 2004]. For the case of Mexico, the effect of hydrothermal circulation is expected to cool the Cocos plate by 125-180°C [Rotman and Spinelli, 2013; Perry et al., 2016]. It is likely that such

cooling would change the depth of dehydration and probably explain the termination of the USL. We also note the efficiency of hydrothermal circulation could change along the trench, as indicated by significant changes in the intensity of surface heat flow in the trench (15-110 mW/m^2, as shown in Figure 6.2). It is thus clear that a model that includes changes in the efficiency of hydrothermal circulation along the strike is needed in order to investigate the termination of the USL.

6.6 Summary and Conclusions

For this study, we created the first three-dimensional model of the Mexican subduction zone, extending from the western edge of the Cocos plate to its flat-slab section in the state of Oaxaca.

Our results show that mantle flow in this region is three-dimensional. The magnitude of the along-strike flow is in the range 0-3.6 cm/yr. Such magnitude represent as much as 60% of the slab convergence rate. The maximum magnitude is located in the transition from normal-dipping slab to a flat-slab and has an eastward direction, consistent with previous studies that show a mantle flowing from steep-dipping to shallow-dipping slab sections [Kneller and van Keken, 2008; Bengtson and van Keken, 2012; Rosas et al., 2016]. The effect of along-strike flow on the thermal structure can be significant along the curved section of the slab, with a thermal change as large as 70°C for the mantle wedge with respect to 2D corner flow models. Such change in temperatures can be important for melt generation and arc volcanism. For the flat slab-section, the thermal change is negligible, indicating 2D models are adequate for the modeling of this region.

In terms of the seismic anisotropy pattern, our flow directions are mostly aligned

with the a-axis of the mantle obtained in other studies [Stubailo et al., 2012; Bernal-López et al., 2015]. Mantle wedge near a tear proposed to exist along the subducted Orozco fracture zone [Stubailo et al., 2012] flows in the eastward direction, consistent with the orientation of the a-axis in the region. This suggests the mantle flows in response to pressure gradients induced by the downgoing plate and by changes in the angle of subduction, and not by the presence of the slab tear along the Orozco fracture zone [Stubailo et al., 2012].

Our results also suggest a thermal origin for the Tzitzio gap, as indicated by a disturbance in the thermal structure of the subducted plate near below the downward projection of the gap. For the termination of the ultra-slow velocity layer observed in the interface of the Cocos and North American plates, we believe this might be related to the effect of hydrothermal circulation, which might reduce temperatues along the subduction interface and thus affect slab dehydration. Future models of the Mexican subduction zone need to incorporate hydrothermal circulation and along-strike changes in the age of the plate at the trench in order to explore this possibility.

Acknowledgments

We thank Jorge Castillo Castellanos for providing the geometry of the subducted Cocos plate, and Igor Stubailo and Caroline Beghein for providing the anisotropy data for Mexico. The figures shown in this study were created using GMT (Generic Mapping Tools; `https://www.soest.hawaii.edu/gmt/`) and Paraview (`http://www.paraview.org/`). Research was funded by the Natural Sciences and Engineering Research Council of Canada (NSERC) and the National Council for Science and Technology of Mexico (CONACYT).

Chapter 7

Conclusions

The main objective of this thesis was to analyze the three-dimensional (3D) thermal structure of subduction zones. Within the subducting oceanic plate, along-strike changes in the thermal structure are due to variations in the age of the slab or changes in the efficiency of hydrothermal circulation in the uppermost oceanic crust. For the mantle wedge, along-strike changes in the subduction geometry (e.g. changes in the angle of subduction or curvature of the trench) or oblique subduction induce an along-strike flow. The resultant flow field is thus a combination of this trench-parallel flow and the 2D corner flow. As the temperatures within the wedge are controlled by advection of hot mantle, this 3D flow field results in a thermal structure that differs from that obtained with traditional 2D corner flow models.

The modeling code used throughout this thesis was PGCtherm3D, a steady- state, finite-element code that uses a kinematic-dynamic approach by having fixed geometries for the upper plate and downgoing slab, a mantle wedge tat evolves dynamically. As the code had not been used before for subduction modeling, extensive testing of it was required prior to its use in specific scientific problems. Once the testing phase of PGCtherm3D was completed, I chose to model the 3D thermal structure of two

sections along the Middle America Trench (MAT): the Costa-Rica Nicaragua subduction zone and the Mexican subduction zone. These regions are ideal for subduction thermal modeling due to (1) significant changes in the angle of subduction along the trench (from flat-subduction in Mexico to a steep dip of $\sim 70^{\circ}$ in Nicaragua [Pardo and Suárez, 1995; Kim et al., 2010; Kyriakopoulos et al., 2015], and (2) a large number of geophysical observations in the form of shear-wave splitting studies [Hoernle et al., 2008; Soto et al., 2009; Stubailo et al., 2012; Bernal-López et al., 2015] and surface heat flow measurements [Ziagos et al., 1985; Prol-Ledesma et al., 1989; Harris et al., 2010a]. Along with geochemical studies of arc magmas in the region [Carr et al., 2003; Gómez-Tuena et al., 2007; Hoernle et al., 2008; Ferrari et al., 2012], this observations help to constrain the thermal state of the subducting slab, and the direction and magnitude of the wedge flow.

7.1 Main Conclusions

The main conclusions of this thesis are:

1. **Effect of the hydrothermal circulation on the thermal state of the Costa Rica-Nicaragua subduction zone (Chapters 4 and 5):**

   Previous studies showed hydrothermal circulation (HC) has an important effect on the shallow thermal structure of the Costa Rica-Nicaragua subduction zone, controlling the magnitude of the surface heat flow near the trench and possibly the length of the megathrust seismogenic zone [Langseth and Silver, 1996; Harris and Wang, 2002; Harris et al., 2010b]. The effect at larger depths, however, had not been investigated previously. The 2D thermal models presented in Chapter 4 include HC through a modified oceanic geotherm and conductivity proxies that simulate heat advection in the oceanic crust aquifer. The results indicate

HC cools the oceanic crust in the East-Pacific Rise (EPR) section (north Costa Rica and Nicaragua) by more than 60°C down to a depth of ∼70 km. For the Cocos-Nazca Spreading Center (CNS) section (central Costa Rica down to Panama), the cooling is ∼30°C at a depth <30 km. The increased EPR cooling is due to water being able to penetrate into the oceanic lithosphere through vertical faults in the outer trench prior to subduction [Ivandic et al., 2010; Van Avendonk et al., 2011]. The vertical faults are only present in the EPR section, probably due to the larger dip of the slab in this region. The extra water that penetrates these faults ventilates the oceanic aquifer, which further reduces the temperatures. In spite of the significant cooling induced by HC in the EPR section, the change in temperatures is not large enough so as alter the Pressure-Temperature (PT) paths of oceanic crust and oceanic lithosphere rocks considerably. This indicates the high amount of wedge hydration observed in Nicaragua [Rychert et al., 2008; Dinc et al., 2011] is likely due to an increased amount of water stored in the Cocos plate in its EPR section, and not due to along-strike changes in dehydration reactions due to variations in the efficiency of HC.

Given the small change in the PT paths in 2D models, it is very unlikely that the addition of along-strike heat diffusion in a 3D model would give a different result. This is confirmed in Figure 5.10, which shows that the depth of eclogitization of the slab remains approximately unaffected throughout the 3D modeling region. The 3D model also gives a seismogenic zone that is in good agreement with the seismogenic zone presented in other studies and with the rupture areas of recent megathrust earthquakes, at least near the Nicoya peninsula. Therefore, HC appears to only affect the shallow thermal structure of the Cocos plate

in Costa Rica-Nicaragua. The results here show 2D models are adequate for studying this part of the subduction zone.

2. **Along-strike mantle flow (Chapters 5 and 6):**

   Changes in the angle of subduction induce along-strike flow due to along-strike pressure gradients created as the plate subducts. Models that use a dislocation creep rheology for the mantle wedge show higher along-strike flow velocities, with a flow pattern that is stronly focused into the wedge corner. In contrast, isoviscous models show smaller flow magnitudes and an along-strike flow that is more dispersed throughout the mantle wedge. Using a dislocation creep rheology, the maximum along-strike flow for the Costa Rica-Nicaragua and Mexican subduction zones is 4 cm/yr and 3.6 cm/yr, respectively. For the case of Mexico, the extreme change in the dip (from $\sim$45° to flat-slab subduction over a distance of $\sim$200 km-250 km) induces a flow that has almost the same magnitude than for Costa Rica-Nicaragua, despite having a slower convergence rate. For both cases, along-strike wedge flow goes from steep dip to shallow dip, and appears to be consistent with shear-wave splitting studies.

3. **Thermal effects of along-strike mantle flow (Chapters 5 and 6):**

   The effect of the along-strike flow on the thermal structure of the mantle wedge depends on the rheology. For an isoviscous wedge, the model for Costa Rica-Nicaragua gives a thermal difference, with respect to 2D corner flow models, of $<$30°C . For a wedge that flows under a dislocation creep rheology, the largest thermal differences are $\sim$60°C an $\sim$75°C in Central America and in Mexico, respectively. Also, thermal models of the Japan subduction developed with PGCtherm3D [Wada et al., 2015] show a thermal difference $>$150°C with respect to 2D models. The effects of these thermal changes can be important for

melt genetartion in the wedge, as the temperatures required for mantle melting are in the range 1000-1300°C depending of the amount of water that is present [Schmidt and Poli, 1998]. For both an isoviscous and a dislocation creep rheology, the largest thermal change is located near the region where the dip of the slab changes. For sections of the slab in which there are no significant along-strike changes in the dip, 2D corner flow dominates and the thermal structure can be adequately modeled with 2D models.

7.2 Future Work

3D kinematic-dynamic models have only been developed for subduction zones in the Marianas and sections of the Andes [Kneller and van Keken, 2007], Japan [Morishige, 2015; Wada et al., 2015], Central America [Rosas et al., 2016] and Mexico (6). More models of subduction zones for which shear-wave splitting studies indicate along-strike flow should be developed in order to better understand the 3D thermal structure of subduction zones. The models developed with PGCtherm3D follow a kinematic-dynamic approach. As such, their accuracy depends on reliable estimates of the geometry of the slab and its convergence rate and direction. To better constrain future models, extensive data in the form of arc geochemistry, shear-wave splitting studies, surface heat flow, earthquake locations, etc, is also needed.

In terms of the models and results presented in this thesis, I now outline several possible future research directions.

a) *Mantle wedge flow due to slab window in Central America:*

For the Costa Rica-nicaragua subduction zone, the mantle wedge in the 3D model presented in Chapter 5 flows in the southeast direction. However, arc

magmas with an ocean-island basalt (OIB) composition indicate that the mantle wedge in Central America flows in the northwest direction [Hoernle et al., 2008]. The models in this thesis show that this flow is not a consequence of along-strike changes in the dip. Instead, the flow may be induced by slab rollback in the area that brings mantle from a slab window located below Panama [Herrstrom et al., 1995; Johnston and Thorkelson, 1997; Abratis and Worner, 2001]. A complete model of the thermal structure in the Central America subduction zone needs to include the slab window. In PGCtherm3D, this could be achieved by modifying the side boundary conditions, currently set at vx = 0 cm/yr (Section 2.3.3). The geochemical studies of arc magmas suggest an along-strike flow with a magnitude of 6.3-19 cm/yr [Hoernle et al., 2008]. The models presented in Chapter 5 show an along-strike flow of ∼4 cm/yr that results in a thermal change with respect to 2D models of ∼60°C . It is therefore reasonable to expect a significantly larger change on the thermal structure if an along-strike flow of 6.3-19 cm/yr could be added to the model, affecting melting temperatures in the mantle wedge and probably PT paths in the slab.

b) *Seismic attenuation and velocities in the mantle wedge:*

S-wave attenuation studies in Central America give values of $Q_s = 76 - 78$ and $Q_s = 84 - 88$ below Nicaragua and Costa Rica, respectively [Rychert et al., 2008]. This may indicate that the mantle wedge is more hydrated below Nicaragua than for Costa Rica [Dinc et al., 2011]. The exact relationship between attenuation, mantle temperature and hydration is still unclear, but several experimentally-derived models have been developed. One of such models is given by:

$$Q_s^{-1} = \Big[B' \exp\Big(-\frac{E + PV}{RT}\Big)\Big]^{\alpha}, \tag{7.1}$$

where B' is a function of the water content C_{OH} (see Section 2.3.2), and α is a constant [Behn et al., 2009; Goes et al., 2012]. Likewise, seismic velocities in the mantle wedge can be related to attenuation values through:

$$v_s = v_\infty[1 - F \cdot Q_s^{-1}] \ , \tag{7.2}$$

where v_∞ is the velocity at infinite frequency, and F is a function of α [Behn et al., 2009]. Equations (7.1)-(7.2) can be applied to the wedge temperatures of the 3D models in Chapters 5 and 6 for varying amounts of water. The resulting model-predicted Q_s and v_s can be compared with the attenuation and seismic velocities observed in the area, allowing us to constrain the amount of water that is released by the Cocos plate [Rychert et al., 2008; Chen and Clayton, 2009].

c) *Slab temperatures in Mexico:*

The models presented in Chapter 6 were developed to investigate the flow field of the mantle wedge and its effects on the thermal structure of the Mexican subduction zone. The thermal state of the subducting slab, however, has not examined in detail in this thesis. The Cocos plate in Mexico has a continous change in its age along the trench, as well as an abrupt change across the Orozco fracture zone (OFZ). Additionally, the effect of HC in Mexico is expected to be significantly larger than for Central America [Rotman and Spinelli, 2013]. In Chapter 6, I propose a thermal explanation for the Tzitzio Gap (the indentation in the Trans- Mexican Volcanic Belt) and the termination of the Ultra-Slow Velocity layer (USL; a highly hydrated layer between the Cocos plate and the North American plate). Thermal models of the Cocos plate in Mexico that

include along-strike changes in the age at the trench as well as the effect of HC are needed in order to explore this hypothesis. Likewise, better estimates of the intensity and distribution of surface heat flow near the trench in Mexico are required to better constrain the effect of HC, as the current available data is sparsely distributed along the MAT.

d) *Time-dependent models:*

The models presented in this thesis are steady-state, i.e, the thermal state evolves until no changes are observed between time steps. For the model to reach a steady-state, some amount of time is required. The thermal evolution is important for subduction zones in which the slab structure is rapidly changing, or in which there have been rapid changes in the convergence rate. A good example is the Mexican subduction zone, in which the slab started to flatten ∼16 Myr ago, but since then it has undergone rollback as indicated by a seaward migration of the volcanic front [Manea et al., 2013]. During this time, it is possible the thermal structure of the mantle wedge has changed. Time-dependent models would allow to investigate the thermal evolution of the mantle wedge.

Bibliography

Abers, G. A., Auger, L., Syracuse, E., Plank, T., Fischer, K. M., Rychert, C., Walker, A., Protti, J., Gonzalez Salas, V., Strauch, W., and Perez, P. (2004). Imaging the Subduction Factory Beneath Central America: The TUCAN Broadband Seismic Experiment. *AGU Fall Meeting Abstracts*.

Abers, G. A., Plank, T., and Hacker, B. R. (2003). The wet Nicaraguan slab. *Geophysical Research Letters*, 30.

Abratis, M. and Worner, G. (2001). Ridge collision, slab-window formation, and the flux of Pacific asthenosphere into the Caribbean realm. *Geology*, 29:127–130.

Abt, D. L., Fischer, K. M., Abers, G. A., Strauch, W., Protti, J. M., and González, V. (2009). Shear wave anisotropy beneath Nicaragua and Costa Rica: Implications for flow in the mantle wedge. *Geochemistry, Geophysics, Geosystems*, 10.

Anderson, R., DeLong, S., and Schwarz, W. M. (1978). Thermal model for subduction with dehydration in the downgoing slab. *The Journal of Geology*, 86:731–739.

Anderson, R., Zoback, M., Hickman, S., and Newmark, R. (1985). Permeability versus depth in the upper oceanic crust: In situ measurements in DSDP hole 504B, eastern equatorial Pacific. *Journal of Geophysical Research*, 90:3659–3669.

Andrews, D. J. and Sleep, N. H. (1974). Numerical modelling of tectonic flow behind island arcs. *Geophysical Journal of the Royal Astronomical Society*, 38:237–251.

Atwater, T. (1970). Implications of plate tectonics for the Cenozoic tectonic evolution of Western North America. *Geological Society of America Bulletin*, 81:3513–3536.

Audet, P. and Schwartz, S. Y. (2013). Hydrologic control of forearc strength and seismicity in the Costa Rican subduction zone. *Nature Geosciences*, 6:852–855.

Bandy, W., Hilde, T., and Yan, C. (2000). The Rivera-Cocos plate boundary: Implications for Rivera-Cocos relative motion and plate fragmentation. *Geological Society of America Special Papers*, 334:1–28.

Bandy, W., Mortera-Gutierrez, C., Urrutia-Fucugauchi, J., and Hilde, T. W. C. (1995). The subducted Rivera-Cocos Plate boundary: Where is it, what is it, and what is its relationship to the Colima rift? *Geophysical Research Letters*, 22:3075–3078.

Barckhausen, U., Ranero, C. R., Cande, S. C., Engels, M., and Weinrebe, W. (2008). Birth of an intraoceanic spreading center. *Geology*, 36:767–770.

Barckhausen, U., Ranero, C. R., Huene, R., Cande, S. C., and Roeser, H. A. (2001). Revised tectonic boundaries in the Cocos plate off Costa Rica: Implications for the segmentation of the convergent margin and for plate tectonic models. *Journal of Geophysical Research*, 106:19207–19220.

Batchelor, G. K. (2000). *An Introduction to Fluid Dynamics*. Cambridge University Press.

Becker, T. W., Kellogg, J. B., Ekström, G., and O'Connell, R. J. (2003). Comparison

of azimuthal seismic anisotropy from surface waves and finite strain from global mantle-circulation models. *Geophysical Journal International*, 155:696–714.

Behn, M. D., Hirth, G., and Elsenbeck, J. R. (2009). Implications of grain size evolution on the seismic structure of the oceanic upper mantle. *Earth and Planetary Science Letters*, 282:178–189.

Behn, M. D., Hirth, G., and Kelemen, P. B. (2007). Trench-parallel anisotropy produced by foundering of arc lower crust. *Science*, 317:108–111.

Bengtson, A. K. and van Keken, P. E. (2012). Three-dimensional thermal structure of subduction zones: effects of obliquity and curvature. *Solid Earth*, 3:365–373.

Bernal-López, L. A., Garibaldi, B. R., León Soto, G., Valenzuela, R. W., and Escudero, C. R. (2015). Seismic anisotropy and mantle flow driven by the Cocos slab under Southern Mexico. *Pure and Applied Geophysics*, pages 1–21.

Billen, M. I. (2008). Modeling the dynamics of subducting slabs. *Annual Review of Earth and Planetary Sciences*, 36:325–356.

Bird, P. (2003). An updated digital model of plate boundaries. *Geochemistry, Geophysics, Geosystems*, 4.

Blatter, D. L. and Hammersley, L. (2010). Impact of the Orozco Fracture Zone on the central Mexican Volcanic Belt. *Journal of Volcanology and Geothermal Research*, 197:67–84.

Cagnioncle, A.-M., Parmentier, E. M., and Elkins-Tanton, L. T. (2007). Effect of solid flow above a subducting slab on water distribution and melting at convergent plate boundaries. *Journal of Geophysical Research*, 112.

Cannat, M., Bideau, D., and Bougault, H. (1992). Serpentinized peridotites and gabbros in the Mid-Atlantic Ridge axial valley at 15°37'N and 16°52'N. *Earth and Planetary Science Letters*, 109:87–106.

Carr, M. J., Feigenson, M. D., Bolge, L. L., Walker, J. A., and Gazel, E. (2014). RU-CAGeochem, a database and sample repository for Central American volcanic rocks at Rutgers University. *Geoscience Data Journal*, 1:43–48.

Carr, M. J., Feigenson, M. D., Patino, L. C., and Walker, J. A. (2003). Volcanism and geochemistry in Central America: Progress and problems. In Eiler, J., editor, *Inside the Subduction Factory*, pages 153–174. American Geophysical Union.

Carr, M. J., Saginor, I., Alvarado, G. E., Bolge, L. L., Lindsay, F. N., Milidakis, K., Turrin, B. D., Feigenson, M. D., and Swisher, C. C. (2007). Element fluxes from the volcanic front of Nicaragua and Costa Rica. *Geochemistry, Geophysics, Geosystems*, 8.

Chandrasekhar, S. (1961). *Hydrodynamic and hydromagnetic stability*. Dover.

Chen, T. and Clayton, R. W. (2009). Seismic attenuation structure in central Mexico: Image of a focused high-attenuation zone in the mantle wedge. *Journal of Geophysical Research*, 114.

Cloos, M. (1993). Lithospheric buoyancy and collisional orogenesis: Subduction of oceanic plateaus, continental margins, island arcs, spreading ridges, and seamounts. *Geological Society of America Bulletin*, 105:715–737.

Conrad, C. P., Behn, M. D., and Silver, P. G. (2007). Global mantle flow and the development of seismic anisotropy: Differences between the oceanic and continental upper mantle. *Journal of Geophysical Research*, 112.

Cozzens, B. D. and Spinelli, G. A. (2012). A wider seismogenic zone at Cascadia due to fluid circulation in subducting oceanic crust. *Geology*, 40:899–902.

Currie, C., Wang, K., Hyndman, R. D., and He, J. (2004). The thermal effects of steady-state slab-driven mantle flow above a subducting plate: The Cascadia subduction zone and backarc. *Earth and Planetary Science Letters*, 223:35–48.

Currie, C. A., Beaumont, C., and Huismans, R. S. (2007). The fate of subducted sediments: A case for backarc intrusion and underplating. *Geology*, 35:1111–1114.

Currie, C. A. and Hyndman, R. D. (2006). The thermal structure of subduction zone back arcs. *Journal of Geophysical Research*, 111.

Currie, C. A., Hyndman, R. D., Wang, K., and Kostoglodov, V. (2002). Thermal models of the Mexico subduction zone: Implications for the megathrust seismogenic zone. *Journal of Geophysical Research*, 107.

Davis, E. E., Wang, K., He, J., Chapman, D. S., Villinger, H., and Rosenberger, A. (1997). An unequivocal case for high Nusselt number hydrothermal convection in sediment-buried igneous oceanic crust. *Earth and Planetary Science Letters*, 146:137–150.

DeMets, C. (2001). A new estimate for present-day Cocos-Caribbean plate motion: Implications for slip along the Central American Volcanic Arc. *Geophysical Research Letters*, 28:4043–4046.

DeMets, C. and Traylen, S. (2000). Motion of the Rivera plate since 10 Ma relative to the Pacific and North American plates and the mantle. *Tectonophysics*, 318:119–159.

DeShon, H. R. and Schwartz, S. Y. (2004). Evidence for serpentinization of the forearc mantle wedge along the Nicoya Peninsula, Costa Rica. *Geophysical Research Letters*, 31.

DeShon, H. R., Schwartz, S. Y., Newman, A. V., González, V., Protti, M., Dorman, L. M., Dixon, T. H., Sampson, D. E., and Flueh, E. R. (2006). Seismogenic zone structure beneath the Nicoya Peninsula, Costa Rica, from three-dimensional local earthquake p- and s-wave tomography. *Geophysical Journal International*, 164:109–124.

Dinc, A. N., Rabbel, W., Flueh, E. R., and Taylor, W. (2011). Mantle wedge hydration in Nicaragua from local earthquake tomography. *Geophysical Journal International*, 186:99–112.

Dougherty, S. L., Clayton, R. W., and Helmberger, D. V. (2012). Seismic structure in Central Mexico: Implications for fragmentation of the subducted Cocos plate. *Journal of Geophysical Research*, 117.

Faccenda, M. and Capitanio, F. A. (2013). Seismic anisotropy around subduction zones: Insights from three-dimensional modeling of upper mantle deformation and SKS splitting calculations. *Geochemistry, Geophysics, Geosystems*, 14:243–262.

Ferrari, L. (2004). Slab detachment control on mafic volcanic pulse and mantle heterogeneity in central Mexico. *Geology*, 32:77–80.

Ferrari, L., Orozco-Esquivel, T., Manea, V., and Manea, M. (2012). The dynamic history of the Trans-Mexican Volcanic Belt and the Mexico subduction zone. *Tectonophysics*, 522:122–149.

Ferrari, L., Petrone, C. M., and Francalanci, L. (2001). Generation of oceanic-island

basalt-type volcanism in the western Trans-Mexican volcanic belt by slab rollback, asthenosphere infiltration, and variable flux melting. *Geology*, 29:507–510.

Fischer, K. M., Parmentier, E. M., Stine, A. R., and Wolf, E. R. (2000). Modeling anisotropy and plate-driven flow in the Tonga subduction zone back arc. *Journal of Geophysical Research*, 105:16181–16191.

Fisher, A. T. (1998). Permeability within basaltic oceanic crust. *Reviews of Geophysics*, 36:143–182.

Fisher, A. T., Davis, E. E., Hutnak, M., Spiess, V., Zuhlsdorff, L., Cherkaoui, A., Christiansen, L., Edwards, K., Macdonald, R., Villinger, H., Mottl, M. J., Wheat, C. G., and Becker, K. (2003a). Hydrothermal recharge and discharge across 50 km guided by seamounts on a young ridge flank. *Nature*, 421:618–621.

Fisher, A. T., Stein, C. A., Harris, R. N., Wang, K., Silver, E. A., Pfender, M., Hutnak, M., Cherkaoui, A., Bodzin, R., and Villinger, H. (2003b). Abrupt thermal transition reveals hydrothermal boundary and role of seamounts within the Cocos plate. *Geophysical Research Letters*, 30.

Forsyth, D. and Uyeda, S. (1975). On the relative importance of the driving forces of plate motion. *Geophysical Journal of the Royal Astronomical Society*, 43:163–200.

Fowler, C. (2005). *The Solid Earth: an Introduction to Global Geophysics*. Cambridge University Press, Second edition.

Furukawa, Y. (1993). Magmatic processes under arcs and formation of the volcanic front. *Journal of Geophysical Research*, 98:8309–8319.

Gaviria, J. R. P., Gutiérrez, C. A. M., Bandy, W. L., and Michaud, F. (2013). Mor-

phology and magnetic survey of the Rivera-Cocos plate boundary of Colima, Mexico. *Geofísica Internacional*, 52:73–85.

Gerya, T. (2011). Future directions in subduction modeling. *Journal of Geodynamics*, 52:344–378.

Gerya, T. and Yuen, D. (2003). Rayleigh-Taylor instabilities from hydration and melting propel cold plumes at subduction zones. *Earth and Planetary Science Letters*, 212.

Goes, S., Armitage, J., Harmon, N., Smith, H., and Huismans, R. (2012). Low seismic velocities below mid-ocean ridges: Attenuation versus melt retention. *Journal of Geophysical Research*, 117.

Gómez-Tuena, A., Orozco-Esquivel, M. T., and Ferrari, L. (2007). Igneous petrogenesis of the Trans-Mexican Volcanic Belt. *Geological Society of America Special Papers*, 422:129–181.

Gordon, R. B. (1967). Thermally activated processes in the Earth: Creep and seismic attenuation. *Geophysical Journal of the Royal Astronomical Society*, 14:33–43.

Grevemeyer, I., Kaul, N., Diaz-Naveas, J., Villinger, H., and Ranero, C. andReichert, C. (2005). Heat flow and bending-related faulting at subduction trenches: Case studies offshore of Nicaragua and Central Chile. *Earth and Planetary Science Letters*, 236:238–248.

Gutscher, M.-A. (2002). Andean subduction styles and their effect on thermal structure and interplate coupling. *Journal of South American Earth Sciences*, 15:3–10.

Gutscher, M.-A., Spakman, W., Bijwaard, H., and Engdahl, E. R. (2000). Geody-

namics of flat subduction: Seismicity and tomographic constraints from the Andean margin. *Tectonics*, 19:814–833.

Hacker, B. R. (1996). Eclogite formation and the rheology, buoyancy, seismicity, and H_2O content of oceanic crust. In Bebout, G., Scholl, D., Kirby, S., and Platt, J., editors, *Subduction Top to Bottom*, pages 337–346. American Geophysical Union.

Hacker, B. R. (2008). H_2O subduction beyond arcs. *Geochemistry, Geophysics, Geosystems*, 9.

Hacker, B. R., Abers, G. A., and Peacock, S. M. (2003). Subduction factory 1. Theoretical mineralogy, densities, seismic wave speeds, and H_2O contents. *Journal of Geophysical Research*, 108.

Hall, P. S. and Kincaid, C. (2001). Diapiric flow at subduction zones: A recipe for rapid transport. *Science*, 292:2472–2475.

Harris, R. N., Grevemeyer, I., Ranero, C. R., Villinger, H., Barckhausen, U., Henke, T., Mueller, C., and Neben, S. (2010a). Thermal regime of the Costa Rican convergent margin: 1. Along-strike variations in heat flow from probe measurements and estimated from bottom-simulating reflectors. *Geochemistry, Geophysics, Geosystems*, 11.

Harris, R. N., Spinelli, G., Ranero, C., Grevemeyer, I., Villinger, H., and Barckhausen, U. (2010b). Thermal regime of the Costa Rican convergent margin: 2. Thermal models of the shallow Middle America subduction zone offshore Costa Rica. *Geochemistry, Geophysics, Geosystems*, 11.

Harris, R. N. and Wang, K. (2002). Thermal models of the Middle America Trench at the Nicoya peninsula, Costa Rica. *Geophysical Research Letters*, 29.

Haskell, N. A. (1935). The motion of a viscous fluid under a surface load. *Journal of Applied Physics*, 7:56–61.

Helffrich, G. and Wood, B. (2001). The Earth's mantle. *Nature*, 412.

Herrstrom, E. A., Reagan, M. K., and Morris, J. D. (1995). Variations in lava composition associated with flow of asthenosphere beneath southern Central America. *Geology*, 23:617–620.

Hirth, G. and Kohlstedt, D. (2003). Rheology of the upper mantle and the mantle wedge: A view from the experimentalists. In Eiler, J., editor, *Inside the Subduction Factory*, pages 83–105. American Geophysical Union.

Hoernle, K., Abt, D. L., Fischer, K. M., Nichols, H., Hauff, F., Abers, G. A., van den Bogaard, P., Heydolph, K., Alvarado, G., Protti, M., and Strauch, W. (2008). Arc-parallel flow in the mantle wedge beneath Costa Rica and Nicaragua. *Nature*, 451:1094–1097.

Hutchison, I. (1985). The effects of sedimentation and compaction on oceanic heat flow. *Geophysical Journal of the Royal Astronomical Society*, 82:439–459.

Hutnak, M., Fisher, A., Harris, R., Stein, C., Wang, K., Spinelli, G., Schindler, M., Villinger, H., and Silver, E. (2008). Large heat and fluid fluxes driven through mid-plate outcrops on ocean crust. *Nature Geoscience*, 1:611–614.

Hutnak, M., Fisher, A., Stein, C., Harris, R., Wang, K., Silver, E., Spinelli, G., Pfender, M., Villinger, H., MacKnight, R., Costa Pisani, P., DeShon, H., and Diamente, C. (2007). The thermal state of 18-24 Ma upper lithosphere subducting below the Nicoya Peninsula, northern Costa Rica margin. In Dixon, T. and

Moore, J., editors, *The Seismogenic Zone of Subduction Thrust Faults*, pages 86–122. Columbia University Press.

Hyndman, R. and Peacock, S. (2003). Serpentinization of the forearc mantle. *Earth and Planetary Science Letters*, 212:417–432.

Hyndman, R. D., Yamano, M., and Oleskevich, D. A. (1997). The seismogenic zone of subduction thrust faults. *Island Arc*, 6:244–260.

Irifune, T. (1993). Phase transformations in the Earth's mantle and subducting slabs: Implications for their compositions, seismic velocity and density structures and dynamics. *Island Arc*, 2:55–71.

Ito, E. and Katsura, T. (1989). A temperature profile of the mantle transition zone. *Geophysical Research Letters*, 16:425–428.

Ivandic, M., Grevemeyer, I., Bialas, J., and Petersen, C. J. (2010). Serpentinization in the trench-outer rise region offshore of Nicaragua: Constraints from seismic refraction and wide-angle data. *Geophysical Journal International*, 180:1253–1264.

Jadamec, M. A. and Billen, M. I. (2010). Reconciling surface plate motions with rapid three-dimensional mantle flow around a slab edge. *Nature*, 465:338–341.

Jadamec, M. A. and Billen, M. I. (2012). The role of rheology and slab shape on rapid mantle flow: Three-dimensional numerical models of the Alaska slab edge. *Journal of Geophysical Research*, 117.

Johnston, S. T. and Thorkelson, D. J. (1997). Cocos-Nazca slab window beneath Central America. *Earth and Planetary Science Letters*, 146:465–474.

Kanamori, H. and Kikuchi, M. (1993). The 1992 Nicaragua earthquake: a slow tsunami earthquake associated with subducted sediments. *Nature*, 361:714–716.

Karato, S. (2010). Rheology of the Earth's mantle: A historical review. *Gondwana Research*, 18:17–45.

Karato, S., Jung, H., Katayama, I., and Skemer, P. (2008). Geodynamic significance of seismic anisotropy of the upper mantle: New insights from laboratory studies. *Annual Review of Earth and Planetary Sciences*, 36:59–95.

Karato, S. and Wu, P. (1993). Rheology of the upper mantle: A synthesis. *Science*, 260:771–778.

Kelley, D. S., Karson, J. A., Blackman, D. K., Fruh-Green, G. L., Butterfield, D. A., Lilley, M. D., Olson, E. J., Schrenk, M. O., Roe, K. K., Lebon, G. T., Rivizzigno, P., and the AT3-60 Shipboard Party (2001). An off-axis hydrothermal vent field near the Mid-Atlantic Ridge at 30° N. *Nature*, 412:145–149.

Kikuchi, M. and Kanamori, H. (1995). Source characteristics of the 1992 Nicaragua tsunami earthquake inferred from teleseismic body waves. *Pure and Applied Geophysics*, 144:441–453.

Kim, Y., Clayton, R. W., and Jackson, J. M. (2010). Geometry and seismic properties of the subducting Cocos plate in central Mexico. *Journal of Geophysical Research*, 115.

Kim, Y., Miller, M. S., Pearce, F., and Clayton, R. W. (2012). Seismic imaging of the Cocos plate subduction zone system in central Mexico. *Geochemistry, Geophysics, Geosystems*, 13.

King, S. (2007). Mantle Downwellings and the Fate of Subducting Slabs: Constraints from Seismology, Geoid Topography, Geochemistry, and Petrology. In Schubert, G., editor, *Treatise on Geophysics*, pages 325–370. Elsevier.

Kirby, S., Engdahl, R. E., and Denlinger, R. (1996). Intermediate-depth intraslab earthquakes and arc volcanism as physical expressions of crustal and uppermost mantle metamorphism in subducting slabs. In Bebout, G., Scholl, D., Kirby, S., and Platt, J., editors, *Subduction Top to Bottom*, pages 195–214. American Geophysical Union.

Kneller, E. and van Keken, P. (2007). Trench-parallel flow and seismic anisotropy in the Mariana and Andean subduction systems. *Nature*, 450:1222–125.

Kneller, E. A. and van Keken, P. E. (2008). Effect of three-dimensional slab geometry on deformation in the mantle wedge: Implications for shear wave anisotropy. *Geochemistry, Geophysics, Geosystems*, 9.

Kummer, T. and Spinelli, G. A. (2008). Hydrothermal circulation in subducting crust reduces subduction zone temperatures. *Geology*, 36:91–94.

Kummer, T. and Spinelli, G. A. (2009). Thermal effects of fluid circulation in the basement aquifer of subducting ocean crust. *Journal of Geophysical Research*, 114.

Kyriakopoulos, C., Newman, A., Thomas, A. M., Moore-Driskell, M., and Farmer, G. T. (2015). A new seismically constrained subduction interface model for Central America. *Journal of Geophysical Research*, 120:5535–5548.

Landau, L. D., Lifshitz, E. M., Sykes, J. B., and Reid, W. H. (1959). *Fluid Mechanics*. Pergamon Press Oxford, England.

Langseth, M. G. and Silver, E. A. (1996). The Nicoya Convergent Margin - A region of exceptionally low heat flow. *Geophysical Research Letters*, 23:891–894.

Li, Z.-H., Di Leo, J. F., and Ribe, N. M. (2014). Subduction-induced mantle flow,

finite strain, and seismic anisotropy: Numerical modeling. *Journal of Geophysical Research*, 119:5052–5076.

Long, M. D. and Silver, P. G. (2008). The subduction zone flow field from seismic anisotropy: A global view. *Science*, 319:315–318.

Long, M. D. and Wirth, E. A. (2013). Mantle flow in subduction systems: The mantle wedge flow field and implications for wedge processes. *Journal of Geophysical Research*, 118:583–606.

MacKenzie, L., Abers, G. A., Fischer, K. M., Syracuse, E. M., Protti-Quesada, J. M., González-Salas, V., and Strauch, W. (2008). Crustal structure along the southern Central American volcanic front. *Geochemistry, Geophysics, Geosystems*, 9.

MacKenzie, L., Abers, G. A., Rondenay, S., and Fisher, K. M. (2010). Imaging a steeply dipping subducting slab in southern Central America. *Earth and Planetary Science Letters*, 296.

Mammerickx, J. and Klitgord, K. D. (1982). Northern East Pacific Rise: Evolution from 25 m.y. B.P. to the present. *Journal of Geophysical Research*, 87:6751–6759.

Manea, M. and Manea, V. C. (2008). On the origin of El Chichón volcano and subduction of Tehuantepec Ridge: A geodynamical perspective. *Journal of Volcanology and Geothermal Research*, 175:459–471.

Manea, V. and Gurnis, M. (2007). Subduction zone evolution and low viscosity wedges and channels. *Earth and Planetary Science Letters*, 264:22–45.

Manea, V. and Manea, M. (2011). Flat-slab thermal structure and evolution beneath Central Mexico. *Pure and Applied Geophysics*, 168:1475–1487.

Manea, V., Manea, M., and Ferrari, L. (2013). A geodynamical perspective on the subduction of Cocos and Rivera plates beneath Mexico and Central America. *Tectonophysics*, 609:56–81.

Manea, V. C., Manea, M., Kostoglodov, V., Currie, C. A., and Sewell, G. (2004). Thermal structure, coupling and metamorphism in the Mexican subduction zone beneath Guerrero. *Geophysical Journal International*, 158:775–784.

Manea, V. C., Manea, M., Kostoglodov, V., and Sewell, G. (2005). Thermomechanical model of the mantle wedge in Central Mexican subduction zone and a blob tracing approach for the magma transport. *Physics of the Earth and Planetary Interiors*, 149:165–186.

Manea, V. C., Pérez-Gussinyé, M., and Manea, M. (2012). Chilean flat slab subduction controlled by overriding plate thickness and trench rollback. *Geology*, 40:35–38.

McKenzie, D. (1979). Finite deformation during fluid flow. *Geophysical Journal of the Royal Astronomical Society*, 58:689–715.

McKenzie, D. P. (1969). Speculations on the consequences and causes of plate motions. *Geophysical Journal of the Royal Astronomical Society*, 18:1–32.

Minear, J. W. and Toksoz, M. N. (1970). Thermal regime of a downgoing slab and new global tectonics. *Journal of Geophysical Research*, 75:1397–1419.

Morishige, M. (2015). A new regime of slab-mantle coupling at the plate interface and its possible implications for the distribution of volcanoes. *Earth and Planetary Science Letters*, 427:262–271.

Naif, S., Key, K., Constable, S., and Evans, R. L. (2015). Water-rich bending faults at the Middle America Trench. *Geochemistry, Geophysics, Geosystems*.

Nakajima, J., Shimizu, J., Hori, S., and Hasegawa, A. (2006). Shear-wave splitting beneath the southwestern Kurile arc and northeastern Japan arc: A new insight into mantle return flow. *Geophysical Research Letters*, 33.

Neumann, F., Vásquez-Serrano, A., Tolson, G., Negrete-Aranda, R., and Contreras, J. (2015). Toroidal, counter-toroidal, and upwelling flow in the mantle wedge of the Rivera and Cocos plates: Implications for IOB geochemistry in the Trans-Mexican Volcanic Belt. *Pure and Applied Geophysics*, pages 1–23.

Newman, A. V., Schwartz, S. Y., Gonzalez, V., DeShon, H. R., Protti, J. M., and Dorman, L. M. (2002). Along-strike variability in the seismogenic zone below Nicoya Peninsula, Costa Rica. *Geophysical Research Letters*, 29.

Oxburgh, E. R. (1968). Problem of high heat flow and volcanism associated with zones of descending mantle convective flow. *Nature*, 218:1041–1043.

Pardo, M. and Suárez, G. (1995). Shape of the subducted Rivera and Cocos plates in southern Mexico: Seismic and tectonic implications. *Journal of Geophysical Research*, 100:12357–12373.

Park, J. and Levin, V. (2002). Seismic anisotropy: Tracing plate dynamics in the mantle. *Science*, 296:485–489.

Patino, L. C., Michael, A., Carr, J., Mark, A., and Feigenson, D. (2000). Local and regional variations in Central American arc lavas controlled by variations in subducted sediment input. *Contributions to Mineralogy and Petrology*, pages 265–283.

Peacock, S., van Keken, P., Holloway, S., Hacker, B., Abers, G. A., and Fergason, R.

(2005). Thermal structure of the Costa Rica-Nicaragua subduction zone. *Physics of the Earth and Planetary Interiors*, 149:187–200.

Peacock, S. M. (1996). Thermal and petrologic structure of subduction zones. In Bebout, G., Scholl, D., Kirby, S., and Platt, J., editors, *Subduction Top to Bottom*, volume 96, pages 119–133. American Geophysical Union.

Peacock, S. M. and Wang, K. (1999). Seismic consequences of warm versus cool subduction metamorphism: Examples from southwest and northeast Japan. *Science*, 286:937–939.

Peltier, W. R. (1974). The impulse response of a Maxwell Earth. *Reviews of Geophysics and Space Physics*, 12:649–669.

Pérez-Campos, X., Kim, Y., Husker, A., Davis, P. M., Clayton, R. W., Iglesias, A., Pacheco, J. F., Singh, S. K., Manea, V. C., and Gurnis, M. (2008). Horizontal subduction and truncation of the Cocos plate beneath central Mexico. *Geophysical Research Letters*, 35.

Perry, M., Spinelli, G. A., Wada, I., and He, J. (2016). Modeled temperatures and fluid source distributions for the Mexican subduction zone: Effects of hydrothermal circulation and implications for plate boundary seismic processes. *Geochemistry, Geophysics, Geosystems*, 17.

Prol-Ledesma, R., Sugrobov, V., Flores, E., Juárez M., G., Smirnov, Y., Gorshkov, A., Bondarenko, V., Rashidoṽ, V., Nedopekin, L., and Gavrilov, V. (1989). Heat flow variations along the Middle America Trench. *Marine Geophysical Researches*, 11:69–76.

Protti, M., Glendel, F., and McNally, K. (1995). Correlation between the age of

the subducting Cocos plate and the geometry of the Wadati-Benioff zone under Nicaragua and Costa Rica. *Geological Society of America Special Papers*, 295:309–326.

Protti, M., Gonzalez, V., Newman, A. V., Dixon, T. H., Schwartz, S. Y., Marshall, J. S., Feng, L., Walter, J. I., Malservisi, R., and Owen, S. E. (2014). Nicoya earthquake rupture anticipated by geodetic measurement of the locked plate interface. *Nature Geoscience*, 7:117–121.

Ranero, C. R., Phipps Morgan, J., McIntosh, K., and Reichert, C. (2003). Bending-related faulting and mantle serpentinization at the Middle America trench. *Nature*, 425:367–373.

Ricard, Y. (2007). Physics of mantle convection. In Schubert, G., editor, *Treatise on Geophysics*, pages 31–87. Elsevier.

Rosas, J. C., Currie, C. A., and He, J. (2016). Three-dimensional thermal model of the Costa Rica-Nicaragua subduction zone. *Pure and Applied Geophysics*.

Rotman, H. M. M. and Spinelli, G. A. (2013). Global analysis of the effect of fluid flow on subduction zone temperatures. *Geochemistry, Geophysics, Geosystems*, 14:3268–3281.

Rouméjon, S. and Cannat, M. (2014). Serpentinization of mantle-derived peridotites at mid-ocean ridges: Mesh texture development in the context of tectonic exhumation. *Geochemistry, Geophysics, Geosystems*, 15.

Rupke, L. H., Morgan, J. P., Hort, M., and Connolly, J. A. (2004). Serpentine and the subduction zone water cycle. *Earth and Planetary Science Letters*, 223:17–34.

Rychert, C. A., Fischer, K. M., Abers, G. A., Plank, T., Syracuse, E., Protti, J. M., Gonzalez, V., and Strauch, W. (2008). Strong along-arc variations in attenuation in the mantle wedge beneath Costa Rica and Nicaragua. *Geochemistry, Geophysics, Geosystems*, 9.

Saffer, D. M., Lockner, D. A., and McKiernan, A. (2012). Effects of smectite to illite transformation on the frictional strength and sliding stability of intact marine mudstones. *Geophysical Research Letters*, 39.

Saffer, D. M. and Marone, C. (2003). Comparison of smectite- and illite-rich gouge frictional properties: application to the updip limit of the seismogenic zone along subduction megathrusts. *Earth and Planetary Science Letters*, 215:219–235.

Schmidt, M. W. and Poli, S. (1998). Experimentally based water budgets for dehydrating slabs and consequences for arc magma generation. *Earth and Planetary Science Letters*, 163:361–379.

Schmidt, M. W. and Poli, S. (2003). Generation of mobile components during subduction of oceanic crust. *Treatise on Geochemistry*, 3:567–591.

Schroeder, T., John, B., and Frost, B. R. (2002). Geologic implications of seawater circulation through peridotite exposed at slow-spreading mid-ocean ridges. *Geology*, 30:367–370.

Schubert, G., Turcotte, D., and Olson, P. (2001). *Mantle Convection in the Earth and Planets*. Cambridge University Press.

Schwartz, S. Y. and Deshon, H. R. (2007). Distinct geodetic and seismic up-dip limits to the northern Costa Rica seismogenic zone: Evidence for two mechanical tran-

sitions. In Dixon, T. and Moore, J., editors, *The Seismogenic Zone of Subduction Thrust Faults*, pages 576–599. Columbia University Press.

Serrato-Díaz, G., Bandy, W., and Mortera-Gutierrez, C. (2004). Active rifting and crustal thinning along the Rivera-Cocos plate boundary as inferred from mantle Bouguer gravity anomalies. *Geofísica Internacional*, 43:361–381.

Skinner, S. and Clayton, R. (2011). An evaluation of proposed mechanisms of slab flattening in central Mexico. *Pure and Applied Geophysics*, 168:1461–1474.

Song, T.-R. A., Helmberger, D. V., Brudzinski, M. R., Clayton, R. W., Davis, P., Pérez-Campos, X., and Singh, S. K. (2009). Subducting slab ultra-slow velocity layer coincident with silent earthquakes in southern Mexico. *Science*, 324:502–506.

Soto, G. L., Ni, J. F., Grand, S. P., Sandvol, E., Valenzuela, R. W., Speziale, M. G., González, J. M. G., and Reyes, T. D. (2009). Mantle flow in the Rivera-Cocos subduction zone. *Geophysical Journal International*, 179:1004–1012.

Spinelli, G., Giambalvo, E., and Fisher, A. (2004). Sediment permeability, distribution, and influence on fluxes in oceanic basement. In Davis, E. and Elderfield, H., editors, *Hydrogeology of the Oceanic Lithosphere*, pages 151–188. Cambridge University Press.

Spinelli, G. A. and Harris, R. N. (2011). Thermal effects of hydrothermal circulation and seamount subduction: Temperatures in the Nankai trough seismogenic zone experiment transect, Japan. *Geochemistry, Geophysics, Geosystems*, 12.

Spinelli, G. A. and Wang, K. (2008). Effects of fluid circulation in subducting crust on nankai margin seismogenic zone temperatures. *Geology*, 36:887–890.

Spinelli, G. A. and Wang, K. (2009). Links between fluid circulation, temperature, and metamorphism in subducting slabs. *Geophysical Research Letters*, 36.

Stein, C. and Stein, S. (1992). A model for the global variation in oceanic depth and heat flow with lithospheric age. *Nature*, 359:123–129.

Stern, R. J. (2002). Subduction zones. *Reviews of Geophysics*, 40:1–38.

Stubailo, I., Beghein, C., and Davis, P. M. (2012). Structure and anisotropy of the Mexico subduction zone based on Rayleigh-wave analysis and implications for the geometry of the Trans-Mexican Volcanic Belt. *Journal of Geophysical Research*, 117.

Syracuse, E. M. and Abers, G. A. (2006). Global compilation of variations in slab depth beneath arc volcanoes and implications. *Geochemistry, Geophysics, Geosystems*, 7.

Syracuse, E. M., Abers, G. A., Fischer, K., MacKenzie, L., Rychert, C., Protti, M., Gonzlez, V., and Strauch, W. (2008). Seismic tomography and earthquake locations in the Nicaraguan and Costa Rican upper mantle. *Geochemistry, Geophysics, Geosystems*, 9.

Toksoz, M. N., Minear, J. W., and Julian, B. R. (1971). Temperature field and geophysical effects of a downgoing slab. *Journal of Geophysical Research*, 76:1113–1138.

Tovish, A., Schubert, G., and Luyendyk, B. P. (1978). Mantle flow pressure and the angle of subduction - non-newtonian corner flows. *Journal of Geophysical Research*, 83:5892–5898.

Turcotte, D. L. and Schubert, G. (2002). *Geodynamics*. Cambridge University Press.

Van Avendonk, H. J. A., Holbrook, W. S., Lizarralde, D., and Denyer, P. (2011). Structure and serpentinization of the subducting Cocos plate offshore Nicaragua and Costa Rica. *Geochemistry, Geophysics, Geosystems*, 12.

van der Pluijm, B. A. and Marshak, S. (2003). *Earth Structure: An Introduction to Structural Geology and Tectonics*. W. W. Norton & Company.

van Hunen, J., van den Berg, A. P., and Vlaar, N. J. (2004). Various mechanisms to induce present-day shallow flat subduction and implications for the younger Earth: a numerical parameter study. *Physics of the Earth and Planetary Interiors*, 146:179–194.

van Keken, P., Currie, C., King, S., Behn, M., Cagnioncle, A., He, J., Katz, R., Lin, S., Parmentier, E., Spiegelman, M., and Wang, K. (2008). A community benchmark for subduction zone modeling. *Physics of the Earth and Planetary Interiors*, 171:187–197.

van Keken, P. E., Kiefer, B., and Peacock, S. M. (2002). High-resolution models of subduction zones: Implications for mineral dehydration reactions and the transport of water into the deep mantle. *Geochemistry, Geophysics, Geosystems*, 3.

Völker, D. and Stipp, M. (2015). Water input and water release from the subducting Nazca plate along southern Central Chile (33 °S-46 °S). *Geochemistry, Geophysics, Geosystems*, 16:1825–1847.

von Huene, R., Ranero, C. R., Weinrebe, W., and Hinz, K. (2000). Quaternary convergent margin tectonics of Costa Rica, segmentation of the Cocos plate, and Central American volcanism. *Tectonics*, 19:314–334.

Wada, I., He, J., Hasegawa, A., and Nakajima, J. (2015). Mantle wedge flow pattern

and thermal structure in Northeast Japan: Effects of oblique subduction and 3-D slab geometry. *Earth and Planetary Science Letters*, 426:76–88.

Wada, I., Rychert, C. A., and Wang, K. (2011). Sharp thermal transition in the forearc mantle wedge as a consequence of nonlinear mantle wedge flow. *Geophysical Research Letters*, 38.

Wada, I. and Wang, K. (2009). Common depth of slab-mantle decoupling: Reconciling diversity and uniformity of subduction zones. *Geochemistry, Geophysics, Geosystems*, 10.

Wada, I., Wang, K., He, J., and Hyndman, R. D. (2008). Weakening of the subduction interface and its effects on surface heat flow, slab dehydration, and mantle wedge serpentinization. *Journal of Geophysical Research*, 113.

Wang, K. (2004). Applying fundamental principles and mathematical models to understand processes and estimate parameter. In Davis, E. and Elderfield, H., editors, *Hydrogeology of the Oceanic Lithosphere*, pages 376–413. Cambridge University Press.

Wang, K. and Davis, E. E. (1992). Thermal effects of marine sedimentation in hydrothermally active areas. *Geophysical Journal International*, 110:70–78.

Wang, K., He, J., Schulzeck, F., Hyndman, R. D., and Riedel, M. (2015). Thermal condition of the 27 October 2012 Mw 7.8 Haida Gwaii subduction earthquake at the obliquely convergent Queen Charlotte Margin. *Bulletin of the Seismological Society of America*.

Wirth, E. A. and Korenaga, J. (2012). Small-scale convection in the subduction zone mantle wedge. *Earth and Planetary Science Letters*, 357:111–118.

Yang, T., Grand, S. P., Wilson, D., Guzman-Speziale, M., Gomez-Gonzalez, J. M., Dominguez-Reyes, T., and Ni, J. (2009). Seismic structure beneath the Rivera subduction zone from finite-frequency seismic tomography. *Journal of Geophysical Research*, 114.

Yue, H., Lay, T., Schwartz, S. Y., Rivera, L., Protti, M., Dixon, T. H., Owen, S., and Newman, A. V. (2013). The 5 september 2012 Nicoya, Costa Rica Mw 7.6 earthquake rupture process from joint inversion of high-rate GPS, strong-motion, and teleseismic p wave data and its relationship to adjacent plate boundary interface properties. *Journal of Geophysical Research*, 118:5453–5466.

Zandt, G. and Humphreys, E. (2008). Toroidal mantle flow through the western U.S. slab window. *Geology*, 36:295–298.

Zhang, S. and Karato, S.-i. (1995). Lattice preferred orientation of olivine aggregates deformed in simple shear. *Nature*, 375:774–777.

Ziagos, J. P., Blackwell, D. D., and Mooser, F. (1985). Heat flow in southern Mexico and the thermal effects of subduction. *Journal of Geophysical Research*, 90:5410–5420.